



저작자표시-비영리-변경금지 2.0 대한민국

이용자는 아래의 조건을 따르는 경우에 한하여 자유롭게

- 이 저작물을 복제, 배포, 전송, 전시, 공연 및 방송할 수 있습니다.

다음과 같은 조건을 따라야 합니다:



저작자표시. 귀하는 원저작자를 표시하여야 합니다.



비영리. 귀하는 이 저작물을 영리 목적으로 이용할 수 없습니다.



변경금지. 귀하는 이 저작물을 개작, 변형 또는 가공할 수 없습니다.

- 귀하는, 이 저작물의 재이용이나 배포의 경우, 이 저작물에 적용된 이용허락조건을 명확하게 나타내어야 합니다.
- 저작권자로부터 별도의 허가를 받으면 이러한 조건들은 적용되지 않습니다.

저작권법에 따른 이용자의 권리는 위의 내용에 의하여 영향을 받지 않습니다.

이것은 [이용허락규약\(Legal Code\)](#)을 이해하기 쉽게 요약한 것입니다.

[Disclaimer](#)

Doctor of Philosophy

**Study on catalytic properties and applications
of metal-doped NiTiO₃ materials**

The Graduate School of the University of Ulsan

Department of Chemical Engineering

Kaiming Jiang

**Study on catalytic properties and applications of metal-doped
NiTiO₃ materials**

Advisor: Professor Eun Woo Shin Professor Yong Men

A Dissertation

Submitted to

The Graduate School of the University of Ulsan

In partial Fulfillment of the Requirements

for the Degree of

Doctor of philosophy

By

Kaiming Jiang

Department of Chemical Engineering

Ulsan, South Korea

July 2021

**Study on catalytic properties and applications of metal-doped
NiTiO₃ materials**

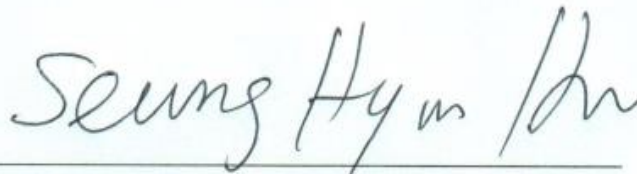
This certifies that the dissertation of
Kaiming Jiang is approved.



Committee Chair Prof. Sung Gu Kang



Committee Member Prof. Won Mook Choi



Committee Member Prof. Seung Hyun Hur



Committee Member Prof. Eun Woo Shin



Committee Member Prof. Yong Men

Department of Chemical Engineering
University of Ulsan
Ulsan, South Korea
July 2021

Abstract

The development of human society and industry is inseparable from the application of catalysts. Current serious environmental problems and huge energy problem make us vulnerable to disasters and tragedies, now and in the future. As a promising oxidation technology, semiconductor catalysis has become a frontier subject that has attracted much attention. Among many materials, perovskite materials have attracted much attention due to their special electronic structure, unique photophysical and chemical properties. Through different preparation methods and several kinds of modification methods, such as transition metal loading or semiconductor compound-ing, this research hopes to conduct more research and explore its applications on perovskite materials.

1 Photocatalytic Decomposition of Toluene by NiTiO₃

In this study, we prepared a nickel titanate (NTN) photocatalyst by a facile synthesis process with microwave method for photocatalytic decomposition of gas phase toluene. P25, a commercial photocatalyst, was also employed for the photo-catalytic decomposition to compare their photocatalytic performance. P25 showed better catalytic performance under UV irradiation, while NTN exhibited a higher re-action rate constant under visible light irradiation. Moreover, NTN generated more CO₂ after the photocatalytic reaction than P25. From XRD patterns and Raman spec-tra, P25 consisted of anatase and rutile TiO₂ structures and NTN existed pure nickel titanate structure. Based on UV-Vis spectra, the bandgaps of P25 and NTN were ob-tained at 3.2 and 2.47 eV, respectively, implying that NTN would be a visible light-responded photocatalyst.

2 Modification of NiTiO₃ materials by transition metal dopants: The dopant size effect

Metal doping is a common modification method. In this study, we investigat-ed the changes of the structural and optical properties of NiTiO₃ materials modified by transition metal doping. Cobalt or tungsten-doped NiTiO₃ materials were success-fully prepared by a modified Pechini method via solvothermal treatment. Raman, FTIR, and XRD spectroscopic analyses showed that the Co²⁺ ions were selectively doped into Ni²⁺ sites in the NiTiO₃ lattice while maintaining an ilmenite structure,

resulting in a solid solution of triple transition metal oxides. The size similarity between Co and Ni induced the formation of a solid solution, $\text{Co}_x\text{Ni}_{1-x}\text{TiO}_3$, in the ilmenite structure. In contrast, W doping into the NiTiO_3 ilmenite structure resulted in an irregularity of the materials due to the characteristics of the heavy transition metal dopant. Along with increasing the W content, the crystallite size in the ilmenite structure decreased from 90.2 to 74.5 nm and new Raman bands at 831 and 892 cm^{-1} for WO_x appeared at high W contents. However, the PL emission intensities gradually decreased with increasing doping content, implying that the recombination process was inhibited in the NiTiO_3 materials by the dopants.

3 Modification of NiTiO_3 by Nb doping and NbO_x heterojunction: Effect of oxygen vacancy

In this research, Nb-doped NiTiO_3 and $\text{NbO}_x/\text{NiTiO}_3$ photocatalysts are prepared with various Nb amounts to enhance photocatalytic activity for dye photodegradation under visible light irradiation. Nb-doped NiTiO_3 exhibits higher photocatalytic activity than pure NiTiO_3 , whereas the inappropriate band structures of NbO_x and NiTiO_3 decrease photocatalytic activity. Incorporation of Nb into the NiTiO_3 lattice induces Ti^{3+} sites and oxygen vacancies. Eventually, the Nb-doped NiTiO_3 photocatalyst at the highest Nb content sample was transformed into a triple metal oxide phase with the highest surface area and oxygen vacancy. The abundant oxygen vacancy of NT-Nb-10 resulted in the lowest photoluminescence emission intensity, which resulted in the highest apparent photocatalytic reaction rate constant (k_{app}) of 14.1 min^{-1} owing to the suppression of the recombination process. The formation of the triple metal oxide phase in this study may allow a potential way to modify low cost visible light-driven NiTiO_3 photocatalysts for sustainable photocatalytic application.

4 Highly stable and selective $\text{Co}_x\text{Ni}_y\text{TiO}_3$ for CO_2 methanation

CO_2 methanation with Sabatier reaction is an effective way to convert the greenhouse gases into valuable industrial product. In this work, we designed and developed a stable and effective Co modified NiTiO_3 catalyst. The best catalyst exhibits high CO_2 conversion (86%) and high methane selectivity (nearly 100%), which can work continuously for 16 hours without significant deactivation at 350 °C. As evidenced by various characterization methods, like XPS, H_2 -TPD and CO_2 -TPR, Co doping is found to influence the electron distribution of the catalyst, change the size

of metal particle and the interaction of metal and support, which in turn has positive impact on methanation performance, while NiTiO₃ support improve the ability to capture CO₂ because of its abundant basic oxide and oxygen vacancies after reduction. Cobalt modification proved to be an potential way to construct Ti-O-Ni interfacial structure, and increase the hydrogen activation site and carbon dioxide activation site simultaneously. This work may provide useful information for designing and optimizing multi-metal modified catalyst for CO₂ methanation.

Key word: NiTiO₃, transition metal doping, heterojunction, photocatalytic, size effect, oxygen vacancy, CO₂ methanation, synergy effect

Acknowledgements

The road ahead will be long and our climb will be steep. When the ten-year studying journey in university was about to be completed, many memories suddenly flashed in my mind: When I was child, my parents took me to the library on weekends. The book 《Hundred Thousand Whys》 caught my attention, and when one question after another was answered, I felt the charm of acquiring knowledge. I remember the copper sulfate crystal growth experiment in science class, and when I finally held the cultivated copper sulfate crystals in my hands, I felt the charm of science. I remember when I was young when someone asked what I wanted to do in the future, my answer was that I wanted to be a scientist. I am lucky, I realized my childhood dream, became a scientist and got a Ph.D.

I am lucky, because I meet excellent tutors during my studies, Professor Eun Woo Shin in University of Ulsan. I would like to express my deep gratitude to Professor Shin. It is he who guided me to carry out this doctoral dissertation work in the lab in University of Ulsan, and he has been paying attention to my work enthusiastically. I also learned a lot from professors, about research and about the love for family. I want to thank him for his advice and support throughout my work. I want to show my most sincere thanks to Professor Men Yong in Shanghai University of Engineering Science. Thanks to the professor Men for his support and help in my studies. I will always remember what professor taught me, about critic thinking, that we need to read literature, but could not follow them blindly. We must keep our own ideas. Believe in the conclusion that I have verified with our own hands.

I also get advice and help from Professor Kang, Sung Gu, Professor Wang Jinguo, Professor An Wei and Professor Liu Shuang. I am glad to meet Chan-yi Park, Nguyen-Huy Chinh, Thanh-Truc Pham, Nguyen-Phu Huy and Do-Thi Lien in the lab in University of Ulsan for warmly welcome my arrival and patiently teach me to do experiments. I must thank all friends studying together in Ulsan University, Yu Hongyan, Li Yuanyuan, Liu Di, Huang Xiaoxiong and He Chengxiang. Huang Haiji, Sui Lijun, Xu Yue, Wang Yuanyuan, Qi Yanchunxiao, Wang Mingyan, Wang zhonghua, Lin Ming, Wang Shiliang for their help and friendship. I will thank all laboratory members in Shanghai, Ji Fei, Wang Xuefei, Song Qiaolin, Wang kang, Li Yingying, Tang Yuhan, Chen Shuyuan, Tian Dandan, Shi Tianle, Li Zhuping, Xiong Liang-

min,Niu xiaoda for their help and friendship.

I am lucky because I also have good parents. I am especially grateful to my parents for their help and caring in all aspects. They show great patience and tolerance for me when I was headstrong and ignorant. They gave me encouragement and help when I fell and deny myself.

Thank professor for reviewing my doctoral thesis and participating in my defense as an expert on the defense committee.

I will start my next journey, and once again sincerely thank all those who have helped me and supported me.

List of Tables

Table 2.1 Properties and photocatalytic reaction rate constants (k_{app}).....	35
Table 3.1 Properties of Co-NT-x and W-NT-x materials	49
Table 3.2 Relative nominal and actual compositions calculated from the EDS analysis of the Co-NT-x and W-NT-x materials.....	52
Table 4.1 Physicochemical properties of the prepared photocatalysts	74
Table 4.2 Optical properties and photocatalytic reaction rate constants (k_{app}) of the prepared photocatalysts	86
Table 5.1 Physico-chemical properties of the prepared materials	107
Table 5.2 Chemical adsorption of H ₂ -TPR and CO ₂ -TPD.....	114
Table 5.3 Selectivity of CH ₄ , CO ₂ conversion, CH ₄ yield and selectivity of CO.	118

List of Figures

Figure 1.1 Band structures of dielectric, semiconductor and metal.....	3
Figure 1.2 Reaction mechanism of photocatalysis	5
Figure 1.3 The ABO ₃ perovskite structure.....	8
Figure 1.4 The unit cell of NiTiO ₃	9
.Figure 1.5 Bandgap energies, and conduction and valence band energy levels of various semiconductors	12
Figure 2.1 XRD patterns of NTN and P25	33
Figure 2.2. Raman spectra NTN and P25	34
Figure 2.3 UV-VIS absorption spectra of NTN and P25	36
Figure 2.4 Photo-degradation of gas phase toluene	37
Figure 2.5 Photo-degradation of gas phase toluene (kinetic)	38
Figure 2.6 The CO ₂ increase of effect on photo-degradation	39
Figure 3.1 XRD patterns of the (A) Co-NT-x and (B) W-NT-x materials	48
Figure 3.2 FE-SEM images of the Co-NT-x materials: (a) x = 0, (b) x = 3, (c) x = 5, (d) x = 7, and (e) x = 10.	50
Figure 3.3 FE-SEM images of the W-NT-x materials: (a) x = 0, (b) x = 3, (c) x = 5, (d) x = 7, and (e) x = 10.	50
Figure 3.4 FE-SEM/EDS elemental mapping of Co-NT-7.	51
Figure 3.5 FE-SEM/EDS elemental mapping of (A) W-NT-7 and (B) marked area of W-NT-7.	51
Figure 3.6 FTIR spectra of the (A) Co-NT-x and (B) W-NT-x materials	53
Figure 3.7 Raman spectra of the (A) Co-NT-x and (B) W-NT-x materials	55
Figure 3.8 The positions of the Ag ² and Eg ³ Raman bands as a function of the Co or W content.	56
Figure 3.9 PL emission spectra ($\lambda_{ex} = 385$ nm) of the (A) Co-NT-x and (B) W-NT-x materials. (C) Variation of intensity ratios of visible emission peaks with Co and W concentration.	58
Figure 3.10 UV-Visible diffuse reflectance spectra of the (A) Co-NT-x and (B) W-NT-x materials:	60
Figure 3.11 Schematic illustrations of the modification of the NiTiO ₃ ilmenite structure by the transition metal dopants.	61
Figure 3.12 MB photocatalytic degradation of pure NiTiO ₃ , Co-NT-3, Co-NT-10, W-NT-3, W- NT-10.	62

Figure 4.1 XRD patterns of Nb-doped NiTiO ₃ (A), and NbO _x /NiTiO ₃ heterojunction (B), and the magnified view of Nb-doped NiTiO ₃ and Nb ₂ O ₅ /NiTiO ₃ (C).....	74
Figure 4.2 Raman spectra of Nb-doped NiTiO ₃ (A) and NbO _x /NiTiO ₃ heterojunction (B)...	76
Figure 4.3 FT-IR spectra of Nb-doped NiTiO ₃ (A) and NbO _x /NiTiO ₃ heterojunction (B). ...	77
Figure 4.4 FE-SEM images of NT (a), NT-Nb-1 (b), NT-Nb-5 (c), and NT-Nb-10 (d).	78
Figure 4.5 FE-SEM images of NT-NbO _x -5 (a), NT-NbO _x -10 (b), NT-NbO _x -20 (c), and NbO _x (d).....	79
Figure 4.6 XPS data of Ni 2p (A), and Ti 2p (B) for NbO _x , pristine NiTiO ₃ , NT-Nb-1, NT-Nb-5, NT-Nb-10, and NT-NbO _x -10.....	80
Figure 4.7 Deconvoluted XPS data of Ti 2p (A) and Nb 3d (B) for pristine and modified NiTiO ₃ materials. Black dashed line is the experimental data and yellow/blue/red/green lines are the fitted data.	81
Figure 4.8 XPS data of O 1s for pristine NiTiO ₃ , NT-Nb-1, NT-Nb-5, NT-Nb-10, and NT-NbO _x -10. Black dashed line is the experimental data, and yellow/blue/red lines are the fitted data.	83
Figure 4.9 Schematic illustration of oxygen vacancy generation in the NiTiO ₃ lattice structure by Nb doping. NiTiO ₃ lattice structure (A) and Nb-doped NiTiO ₃ lattice structure (B).	84
Figure 4.10 UV-VIS absorption spectra of Nb-doped NiTiO ₃ (A) and NbO _x /NiTiO ₃ heterojunction (B).....	85
Figure 4.11 Tauc plots for the photocatalysts to calculate E _g	86
Figure 4.12 PL emission spectra of Nb-doped NiTiO ₃ photocatalysts (A), NbO _x /NiTiO ₃ heterojunction photocatalysts (B), and PL emission peak intensities at 528 nm vs. Nb loading concentrations (C).....	88
Figure 4.13 EIS Nyquist plots of the photocatalysts.	89
Figure 4.14 MB photocatalytic degradation of pure NiTiO ₃ , Nb-doped NiTiO ₃ , and NbO _x /NiTiO ₃ heterojunction photocatalysts.	90
Figure 4.15 Radical trapping experiment results of the MB photocatalytic degradation for NT-Nb-10.....	91
Figure 4.16 Band diagrams for NiTiO ₃ and NbO _x in the NbO _x /NiTiO ₃ heterojunction	93
Figure 4.17 MO photocatalytic degradation of all the photocatalysts.	94
Figure 4.18 Zeta potential of NT, NT-Nb-10 and NT-NbO _x -10.	94
Figure 5.1 XRD result of (A) before hydrogen reduction and (B) after reaction CoNT-X catalysts.	106
Figure 5.2 N ₂ sorption isotherms for fresh CoNT-X catalysts.....	108
Figure 5.3 SEM images for a)NT b)CoNT-0.5 c)CoNT-1 d)CoNT-5 and e)CoNT-25	109
Figure 5.4 XPS result of Ti 2p and Ni 2p of CoNT-X.	110

Figure 5.5 Deconvoluted XPS data of Ni 2p and O1s for CoNT-X catalyst. Black line is the experimental data and yellow/blue/red/green lines are the fitted data.....	112
Figure 5.6 Deconvoluted XPS data of Co 2p for CoNT-X catalyst. Black line is the experimental data and yellow/blue/red/green lines are the fitted data, the peak value of CoNT-0.5,1,5 was magnified twice.	113
Figure 5.7 H ₂ -TPR result for CoNT-X catalyst.	115
Figure 5.8 CO ₂ -TPD result for CoNT-X catalyst.....	116
Figure 5.9 A) CO ₂ conversion, B) CH ₄ selectivity and C) CO selectivity of CoNT-x catalyst at 12000h ⁻¹ , m _{cat} = 0.1 g, H ₂ /CO ₂ = 4.....	118
Figure 5.10 Arrhenius plot for NT and CoNT-1 catalyst at 12000h ⁻¹ around 200 °C.....	119
Figure 5.11 Activity test of CoNT-1 catalyst at different space velocities, 350 °C, m _{cat} = 0.1 g, H ₂ /CO ₂ = 4	120
Figure 5.12 Stability test on the CoNT-1 catalyst at 350 °C, m _{cat} = 0.1g, 12000h ⁻¹ , H ₂ /CO ₂ = 4.....	121
Figure 5.13 Proposed mechanism of CO ₂ methanation on the CoNT catalyst.	122

Table of Contents

Abstract	iv
Acknowledgements	vii
List of Tables	ix
List of Figures.....	x
Table of Contents.....	xiii
1 Introduction:.....	1
1.1 Catalysis and catalytic reaction	1
1.2 Semiconductor photocatalyst.....	2
1.2.1 Introduction of semiconductor.....	2
1.2.2 Semiconductor photocatalysis mechanism	4
1.2.3 Application of photocatalytic technology.....	6
1.3 Research status of photocatalysts	7
1.3.1 Lattice structure of perovskite photocatalyst	7
1.3.2 Preparation method of photocatalysts.....	9
1.3.3 Effect factors of catalyst activity	11
1.4 Modification of perovskite catalyst	14
1.4.1 Metal modification.....	14
1.4.2 Semiconductor heterojunction structure	15
1.5 Motivation	16
References	19
2 Photocatalytic decomposition of toluene by NiTiO ₃ photocatalysts under visible-light irradiation.....	30
2.1 Introduction	30
2.2 Experiment.....	31
2.2.1 Catalyst synthesis.....	31
2.2.2 Catalyst characterization.....	31
2.2.3 Photodegradation experiments.....	31
2.3 Results and discussion	32
2.3.1 Structural properties of photocatalysts.....	32
2.3.2 Optical properties of the photocatalysts.....	36
2.4 Conclusions	40
References	41
3 Modification of the structural properties of NiTiO ₃ materials by transition metal dopants (Co and W).....	44

3.1	Introduction	44
3.2	Experiment.....	45
3.2.1	Catalyst synthesis.....	45
3.2.2	Catalyst characterization.....	46
3.2.3	Photocatalysis and analyse	46
3.3	Results and discussion	47
3.3.1	Structural properties of photocatalysts	47
3.3.2	Photocatalytic behavior of the photocatalysts	62
3.4	Conclusion.....	63
	References	64
4	Modification of NiTiO ₃ visible light-driven photocatalysts by Nb doping and NbOx heterojunction	67
4.1	Introduction	67
4.2	Experimental.....	68
4.2.1	Materials preparation.....	68
4.2.2	Characterization.....	69
4.2.3	Photocatalysis and analyses	71
4.3	Results and discussion	71
4.3.1	Structural properties of photocatalysts	71
4.3.2	Electronic properties of photocatalysts.....	79
4.3.3	Optical properties of the photocatalysts.....	84
4.3.4	Photocatalytic behavior of the photocatalysts	89
4.4	Conclusion.....	95
	References	96
5	Highly stable and selective Co _x Ni _y TiO ₃ for CO ₂ methanation	101
5.1	Introduction	101
5.2	Experimental.....	103
5.2.1	Materials preparation	103
5.2.2	Characterization	103
5.2.3	Catalytic performance.....	104
5.3	Results and discussion	105
5.3.1	Catalysts characterization	105
5.3.2	CO ₂ methanation performance.....	116
5.3.3	Catalytic mechanism analysis.....	121
5.4	Conclusion.....	123
	References	123
6.	Summary.....	129

6.1 Summary of this work	129
6.2 Prospect	130
7.Papers Published During the Study for Ph. Degree	132

1 Introduction:

1.1 Catalysis and catalytic reaction

Catalysis is an important phenomenon that exists widely in nature, which plays an important role in the maintenance of life and the circulation of matter[1-3]. The discovery and application of catalysis by mankind has deeply affected the development and process of the world[4-12]. In 1910, the industry successfully synthesized ammonia for the first time and achieved large-scale production, which was the most important milestone in the history of catalytic development[13]. In the modern industrial production process, the production of various products is almost inseparable from the use of catalysts. Industrial manufacturing processes often produce nasty by-products which can cause harm to a person or the environment. Catalysts can also help solve that problem. Appropriate choice of better catalyst actually produces fewer toxic by-products—making the whole reaction more environmentally friendly. Catalysts are also the important key to unlocking biofuels to solve energy problem. Transferring biomass, such as corn, trees, or straw into biofuel requires an efficient conversion of cellulose. Synthesizing the suitable catalyst would make biofuels economically feasible and work as a renewable energy source[14-16]. Nowadays, variety of catalysts have been widely used in various fields around the world, from the necessities of daily life to drug research, the update of various technologies requires the use of catalysts. The research on catalysts and catalytic systems will help promote the development of human society.

Development of efficient catalysts with excellent activity, controlled and well stability and is a desirable goal for researchers around the world. These new catalysts may be new prepared materials or modified existing catalysts, including supporting metals, supporting non-metals and forming composite heterojunction structures.[17-19] Adjusting the exposed crystal planes, oxygen vacancy concentration, electron density, metal carrier interaction, etc. may all be potential ways to understand the internal mechanism of the reaction[20-33].

1.2 Semiconductor photocatalyst

This rapid industrialization process promoted human social, but also causing many environmental pollution problems. Air pollution, water pollution and soil pollution caused by organic residues have become a serious threat to the health of organisms. These organic pollutants affect human health and the growth of animals and plants, destroying the ecological balance[34-36]. These pollutants may bring the risk of cancer; continue to react in the environment and cause secondary harm to the ecology; pollutants will accumulate in the environment and organisms and accumulate along the food chain. Therefore, find the high-efficiency and cost-effective treatment technology with mild reaction conditions, no secondary pollution and fast degradation rate has become the key research topic today [37-39].

Sunlight can be converted into electricity or hydrogen energy. It also can be used to degrade organic pollutants [40]. The development and utilization of solar energy has become one of the most promising options to alleviate the energy crisis and reduce environmental pressure [41]. Early 20th century, researchers discovered that TiO_2 has a bleaching effect on dyes. However, due to theoretical limitations, this phenomenon was simply classified as UV light-induced effect and did not attract enough attention. In 1972, Fujishima firstly discovered that TiO_2 can catalyze the decomposition reaction of H_2O to generate hydrogen (H_2) and oxygen (O_2) under ultraviolet light irradiation [42]. After that, photocatalytic technology began to enter a new field. In 1977, Frank et al. found that TiO_2 can degrade hydroquinone under xenon lamp irradiation and discussed its degradation mechanism [24]. In recent years, semiconductor photocatalysis technology has attracted widespread attention, and a large number of photocatalytic materials and applications have been reported in the literature [43-47].

1.2.1 Introduction of semiconductor

According to the conductivity, material can be divided into three categories: insulators, semiconductors and conductors, as shown in **Figure 1.1**. The conductivity of a material is determined by the number of free electrons in the material.

According to the basic assumptions of quantum mechanics, the electrons outside atoms can only obtain certain specific energies under certain conditions, called energy level. When there are many atoms in the system, due to the interaction between the atoms, the energy levels of the atoms will move. The same energy level has become a

group of energy levels with very little difference, called energy band. Since the energy difference of different energy levels in the energy band is very small, they are continuous. The energy band is the same as the energy level. There is a gap without energy level between each other. This gap is the band gap. When the atom is in the ground state, all its electrons are filled in sequence starting from the lowest energy level. For semiconductors, electrons just fill up to a certain energy band, and the next energy band is completely empty. The one with the highest energy among these filled energy bands is called the valence band. Since the generation of electric current requires the directional movement of carriers, the electrons in the valence band cannot move because they have occupied almost all the positions. Therefore, the electrons in the valence band can be considered non-conductive. If these electrons transition to the next empty energy band, they can migrate freely, and this energy band is the conduction band. There is a forbidden band between the conduction band and the valence band. The band gap of the insulator is too large for electrons to transition. For metals, the conduction band and the valence band directly overlap.

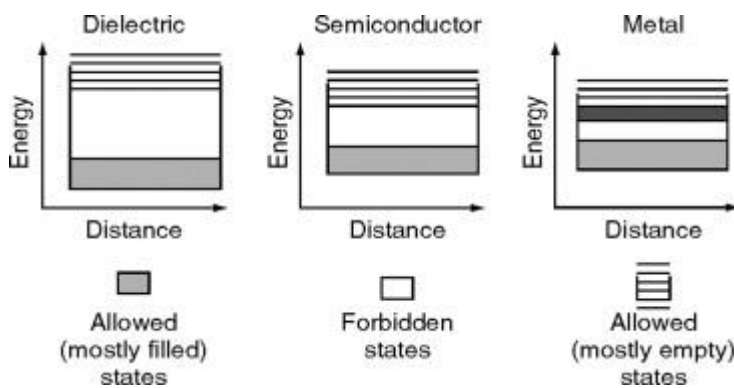


Figure 1.1 Band structures of dielectric, semiconductor and metal.[48]

New energy levels can be introduced by doping impurities and the width of the band gap can be changed. Taking silicon as an example, doping with phosphorus or arsenic can introduce a set of full energy levels at a position close to the conduction band. The electrons at this level can easily transition to the conduction band and become conduction band electrons. This is N Type semiconductor. Doping with boron can introduce a set of empty energy levels near the valence band. The electrons in the valence band can easily transition to this energy level. The holes left in the valence

band after the electron transition. This is p-type semiconductor. Free electrons and holes in semiconductors are called carriers. Semiconductors without doping also have free electrons and holes, but the number is relatively small.

1.2.2 Semiconductor photocatalysis mechanism

Semiconductors are those materials which has conductivity between conductors and insulators at room temperature. Semiconductor photocatalyst is a material which absorbs light and provides such energy to a reacting substance to promote the synthesis or decomposition of compounds.

Photocatalyst is a serious of chemistry concerned with the chemical effects under light irradiation. Photocatalytic reaction is a combination of photoreaction and catalytic reaction. According to the theory of energy band, the band structure of semiconductors is including the forbidden band between the valency band and conductivity bands. There are two types of charge carriers, the electrons in the conductivity band and holes in the valency band. There are no electrons in the forbidden band, and the electrons will not stay there after being excited. The energy difference between the upper and lower edges of the forbidden band is called the forbidden band width or band gap (E_g). When light with energy equal to or higher than the forbidden band width is irradiated, electrons in the semiconductor valence band are excited to transition to the conduction band, and corresponding holes are generated in the valence band, so that corresponding electron-hole pairs are formed on the semiconductor. If the electrons and holes are separated and migrate to different positions on the particle surface, they can undergo redox reactions with surface adsorption material [49].

The specific process of photocatalytic reaction includes those processes: photon absorption, exciton generation, carrier diffusion, carrier separation and recombination and catalytic reaction. As **Figure 1.2**, photo-generated holes have strong oxidizing properties and generate $\cdot\text{OH}$. It has stronger oxidizing properties which can non-selectively oxidize more kinds of organic substances. Photogenerated electrons can react with O_2 to generate O^{2-} and other reactive oxygen species, and they can also degrade the adsorbed organic matter. After the semiconductor is irradiated by photons with energy greater than the band gap, the electrons transition from the valence band to the conduction band, resulting in electron-hole pairs. The electrons are reducible, and the holes are oxidizing.

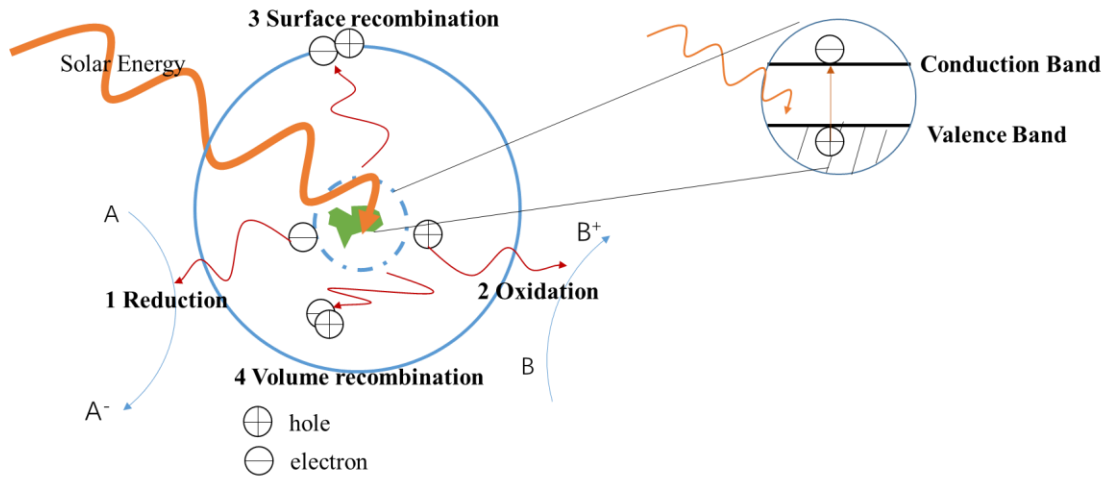
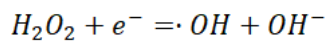
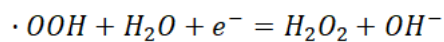
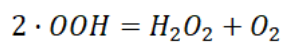
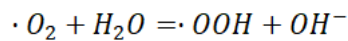
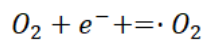
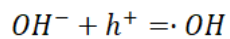
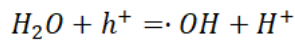


Figure 1.2 Reaction mechanism of photocatalysis

As an advanced oxidation technology, semiconductor photocatalysis technology has shown broad application prospects in environmental pollution control. The semiconductor catalyst could use the extremely strong redox ability of electrons and holes, and the photo-generated electrons and photo-generated holes continue to react with different substances adsorbed on the surface of the semiconductor catalyst to form new active substances. The process is as follow:



1.2.3 Application of photocatalytic technology

In our daily lives, we are at risk of lung damage and asthma attacks because of toxic air, such as formaldehyde, SO₂ and NO₂. Exposure to harmful environment may cause damage to our health and may threaten our lives in severe cases. Besides, volatile organic compounds (VOC) can also cause various physiological and psychological disorders to living organisms. Because of their very low vapor pressures, they are capable of vaporizing at normal atmospheric conditions. Photocatalyst can effectively degrade these toxic gases and will not produce other pollutants. Therefore, this type of catalyst has become one of the indispensable components in air purification devices [50-59].

Environment safety is not only focus on the harmful effects of people's health, but also refers to human and national survival development free from environmental pollution and persecution. Water environmental safety has also received more attention. The problem of the water environment from contamination by series types of discharges, such as heavy metals, dyes, now has been concern. It can also be completely degraded by using the redox ability of the photocatalyst[60-66]. Chen et al. synthesized g-C₃N₄/Bi₂WO₆ heterojunction photocatalysts and investigated the practical photocatalytic performance for water purification with organic dyes and antibiotics under visible-light irradiation [67]. Xiong et al. prepared Ag/TiO₂ photocatalyst for photocatalytic degradation of RhB and inactivation of E. coli which shows the application potential in water purification field [68].

The development of human society relies on energy. Scientists have proposed various solutions to the current energy shortage. The development of hydrogen energy is one of them. Hydrogen is a clean, efficient, renewable energy. It would be better if it is created using renewable energy instead of fossil fuels, like hydrogen production by photolysis of water. Under the irradiation of ultraviolet light, the water molecules adsorbed on the surface of the catalyst are oxidized to oxygen, and the H⁺ in the electrolyte is reduced to hydrogen by electrons [2, 18, 69-73].

The growth in the industrialized has contributed to a serious of problem such as energy shortage and environmental pollution. Excessive burning of fossil fuels has led to a continuous increase in the concentration of carbon dioxide, leading to the greenhouse effect, which will cause glaciers and sea ice melting, more frequent and severe weather, higher sea levels and more acidic oceans. Transfer carbon dioxide to fuel with

photocatalyst will be a futuristic way to combat the energy crisis and CO₂ emission issues [74-76]. Duo et al. reported a high CH₄ generation rate (241.6 μmol h⁻¹ g⁻¹) with the high selectivity (96 %) ZnO/CuO_x catalysts for CO₂ reduction reaction, which turn greenhouse gas into valuable hydrocarbons [71]. Moradi et al. prepared Pt@Bi-TiO₂ via sol-gel and photodeposition techniques High capability of CO₂ adsorption from Bi doping and efficient charge separation caused by Pt nanoparticles enhanced the performance of CO₂ photo-reduction into CH₄ [77].

1.3 Research status of photocatalysts

1.3.1 Lattice structure of perovskite photocatalyst

Multi-element metal oxides have important applications in electronic equipment materials, industrial catalysts and other fields.[78-84] It is the basic material of various important technologies. Multi-element metal oxides have always been the focus of research. We need to design new solid materials to use energy more efficiently. Perovskite-type oxides belong to a large class of inorganic materials, which can contain various cations in the periodic table, and can also be doped with anions to change the physical and chemical properties of the sample. Perovskite oxide has a wide range of research applications in the fields of photocatalysis, electronics, and energy storage [73, 85-91].

Typically, the general chemical formula of perovskite material is ABO₃, as shown in Figure 1.3 where A represents alkaline earth elements or rare earth metals, and B represents transition metal elements. There are many types of perovskite materials, such as tantalate, titanate and niobate. The large ionic radius cations occupy the A position in the structure and coordinate with 12 oxygen atoms, and the small radius cations occupy the B position and form coordination with the surrounding 6 oxygen atoms. Different coordination environments also determine the different valence states of cations. Perovskite has an open lattice structure, and the two positions A and B can be occupied by most of the metal elements. These metal atoms can be effectively incorporated into the perovskite lattice and keep the original basic structure unchanged. Due to the different degrees of lattice distortion in the perovskite structure, expect ABO₃ cubic perovskite structure, perovskite also could be orthogonal, rhombic, te-

tragonal, monoclinic or triclinic. Different crystal structures may affect the crystal field, change the electronic band structure and dipole of the perovskite, which change its reactivity. The change of the electronic energy band structure will also affect the catalytic reaction of the photo-generated charge.

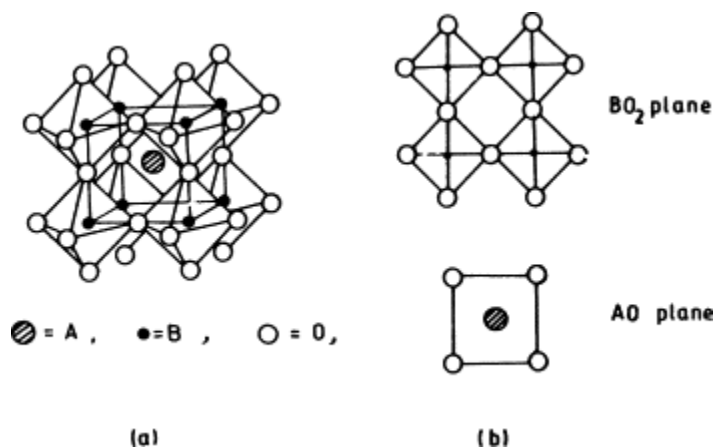


Figure 1.3 The ABO₃ perovskite structure.[92]

Among many catalytic materials, perovskite materials have attracted much attention due to their special electronic structure and crystal structure, unique photophysical and electrochemical properties. General perovskite materials have a wide band gap structure. This kind of ultraviolet light active semiconductor photocatalyst has a higher efficiency but shows a faster carrier recombination rate. The band gap and band edge potential of the perovskite crystal structure can be adjusted according to the specific photocatalytic reactions [93, 94].

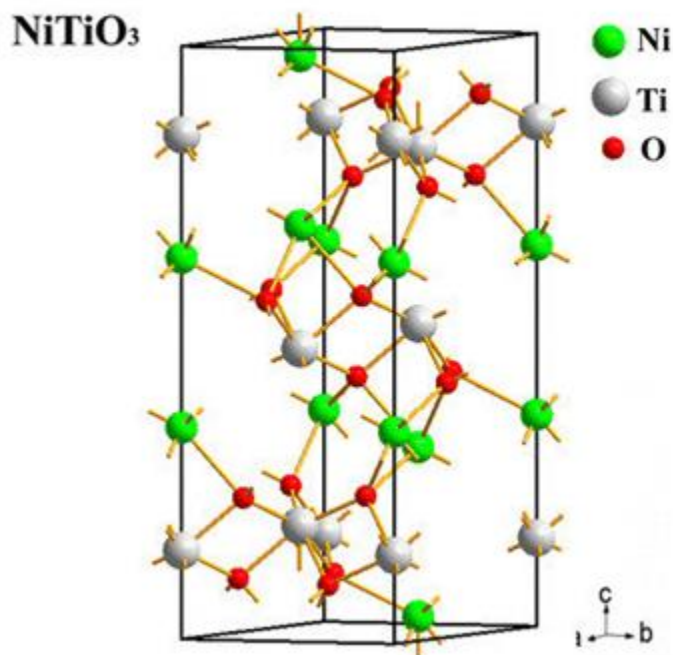


Figure 1.4 The unit cell of NiTiO₃[95]

Nickel titanate (NiTiO₃) is a double-metal semiconductor with an ilmenite structure; which Ni and Ti both prefer octahedral coordination with alternating cation layers occupied by Ni and Ti alone. It is known as a potential visible light-driven photocatalyst owing to its acceptable cost, high stability under light illumination, nontoxicity for humans body and great durability in an oxidizing environment. NiTiO₃ has a narrow band gap of ca. 2.18 eV where electrons in the valence band can be excited to conduction band under visible light irradiation.

1.3.2 Preparation method of photocatalysts

Over the years, different preparation methods of perovskite materials have also received extensive attention. The synthesis method of metal oxide samples has a significant impact on the catalytic efficiency. Researchers can optimize the catalyst by improving the crystallinity of the sample, increasing surface defects, creating a porous structure, adjusting the exposed surface, and reducing the particle size.

1.3.2.1 Hydrothermal and Solvothermal

In a closed container, the method of using temperature and pressure to dissolve and recrystallize a substance is called hydrothermal method. When the solvent is other solution instead of water, it is called solvothermal method. During the reaction process,

temperature and pressure are important factors that affect the synthesis of materials. In addition, reaction conditions such as reaction time, raw material ratio, pH, and solvent types will affect the structure and performance of the sample. The synthesis environment of the hydrothermal method determines that it has higher requirements for equipment, but relatively, the method has a faster chemical reaction rate and a relatively simple preparation process. The sample prepared by the hydrothermal method has fewer impurities, uniform particles and no agglomeration. Therefore, the hydrothermal method is popular choice for preparing catalyst in the laboratory. Singh et al. successfully prepared double perovskites oxides $\text{La}_2\text{CuMnO}_6$ through hydrothermal synthesis method and investigated the electrochemical performance [96]. Pei et al. reported a hierarchical single-crystal like structure CaTiO_3 photocatalyst prepared by hydrothermal. This material shows well H_2 evolution rate under visible-light irradiation [70].

1.3.2.2 Sol-gel method

The sol-gel method uses alkoxides or inorganic salts as precursors to hydrolyze and polycondensate the solution into a sol, then age to obtain a gel, heat the gel to remove excess solvent, and finally prepare the required material through drying and heat treatment. This method needs to concerned the types and amounts of precursors, solvents, complexes, and calcination temperature. The adjustment of parameters will affect the particle size and morphology of the sample, and even the crystal form. The biggest advantage of this method is simplicity, low requirements for operating equipment, and easy operation. The disadvantage of this method is the sample may agglomerate during the subsequent gel drying and high-temperature calcination. Nevertheless, the sol-gel method is a popular and commonly method in laboratory [22, 38, 55, 61, 77].

1.3.2.3 Coprecipitation method

Coprecipitation is a simple, economically friendly, fast process method for synthesizing nanoparticles which frequently quoted in the research and selected for industrial applications. In a typical reaction, a salt precursor, for example, nitrate or chloride and base such as ammonium hydroxide or sodium hydroxide is dissolved in aqueous solution to get the corresponding hydroxides. In this step, if more types of precursor salt was added into this solution, multi-metal oxides may can be formed by coprecipitation

of the corresponding hydroxides. After washing, drying and calcination, hydroxides resulting in target metal oxide nanoparticles powders. Few Challenges still limit this method, for example, the precipitation rate has a great influence on the grain size of the final product. The particle size and shape, crystallinity, defects and chemical composition of the target nanoparticles can be controlled by a series of reaction parameters, including but not limited to reaction temperature, the type of precursors, the precursor ratio and the pH value [97-99].

In addition to the above-mentioned several common synthetic methods, there are microwave method, electrochemical deposition method, electrostatic spinning method, precipitation method and so on. The structure, morphology, and performance of the catalyst synthesized by various methods are likely to vary greatly, so it is necessary to select a suitable synthesis method according to specific needs.

1.3.3 Effect factors of catalyst activity

1.3.3.1 Crystal phase

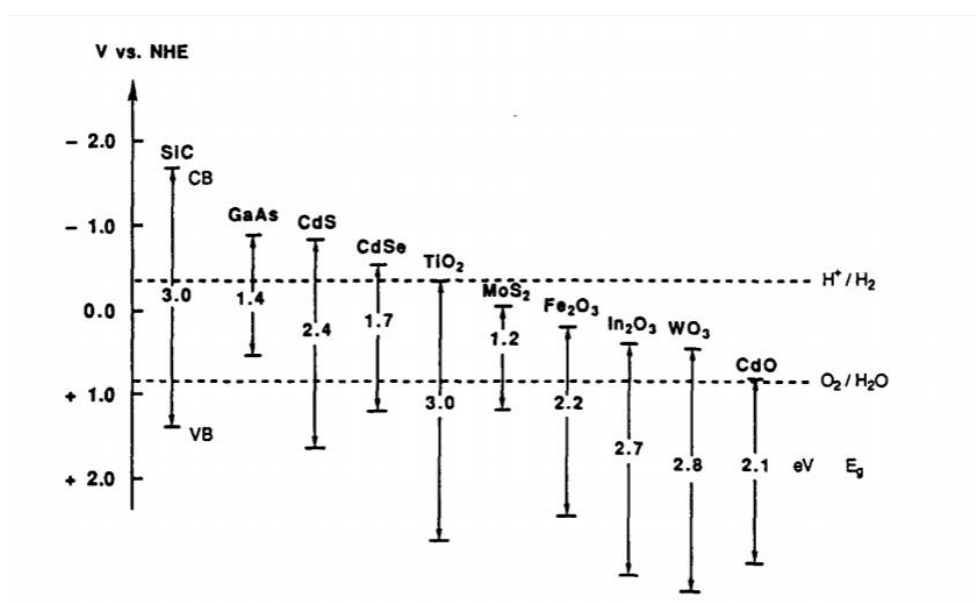
Compounds may have multiple crystal structures, for example, TiO_2 shows three types of crystal structure, rutile, anatase and brookite [100, 101]. Anatase TiO_2 exhibits higher activity performance than rutile TiO_2 in many photocatalytic reactions and water reduction, while rutile TiO_2 shows superior activity than anatase in water oxidation reaction. However, brookite phase also could show the best performance compared to other two structure in several photocatalytic reactions. Electron diffusion coefficient, the probability of simple recombination of electron-hole and the absorption capacity of organic matter on its surface are considered as the reason may influence the catalyst performances [72, 102].

1.3.3.2 Influence of band gap and band position

For photocatalysts, the width of the energy band directly affects the capacity of solar energy utilization. Only ultraviolet light can be absorbed and utilized under width band gap. Adjusted the band gap of this material so that it can be responded to visible light irradiation will be a good way to have a better use of the visible light part of solar energy. Besides, the energy band position of the semiconductor and the oxidation-reduction potential of the adsorbed species also determine the photocatalytic reaction

capability of the semiconductor. The photocatalytic redox reaction requires that the relative potential energy of the acceptor species is lower than the potential energy of the semiconductor conduction band and the potential energy of the donor species that can provide electrons to holes should higher than the position of the semiconductor valence band [16, 35, 37, 87, 100, 103, 104].

The band gap of common semiconductor photocatalysts and the relative position of the standard hydrogen electrode potential and vacuum energy level are shown in Figure 1.5 [105].



.Figure 1.5 Bandgap energies, and conduction and valence band energy levels of various semiconductors

1.3.3.3 Influence of grain size

The catalytic reaction occurs on the surface of the catalyst, and the specific surface area of the sample will have a significant impact on the catalytic activity. Generally, the larger the specific surface area, the more catalytically active sites may be exposed on the surface, and the greater the concentration of active free radicals generated on the surface. In addition, when the specific surface area increases, the time required for the reaction substrate to reach adsorption equilibrium on the catalyst surface is shorter, thereby increasing the probability of substrate degradation.

The grain size will have a complicated effect on the catalytic reaction. On the one hand, the specific surface area of the catalyst is affected by the grain size. Generally

speaking, the smaller the grain size, the larger the specific surface area. On the other hand, grain size affects carrier migration speed. In the crystal grains of the catalyst, the photo-generated charge will diffuse from the inside of the crystal to the surface of the crystal grain. When the grain size decreases, the carrier diffusion time shows a quadratic decrease in relation to the diffusion radius. The earlier the carrier arrives at the surface of the crystal grain, the smaller the probability of recombination, which shows that the sample has higher catalytic activity.

When the grain size decreases, more surface defects will be generated, and the probability of recombination of electrons and holes separated in the bulk phase on the surface will increase. When the recombination rate is large, the catalytic activity will also decrease. The activity of the catalyst is the result of the combined effect determined by the difference in specific surface area, carrier separation and recombination, and light absorption ability caused by different crystal grain sizes [54, 80, 85].

1.3.3.4 Influence of crystallinity and oxygen deficiency

The higher the degree of crystallinity in the photocatalytic material, the greater the dipole moment of the polyhedral unit constituting the crystal structure, the faster the charge transfer and the higher the activity. There is no perfect crystal without defects. Therefore, when carriers diffuse from the bulk to the catalyst surface, crystal defects must be considered. When the defect captures only one type of photo-generated carrier (electron or hole), it can effectively separate the electron and the hole and improve the catalytic activity. However, when the defect concentration is too high and electrons and holes are trapped at the same time, instead, a region where electrons and holes recombine are formed, resulting in a decrease in catalytic activity. In the preparation process of the catalyst, the formation of bulk defects in the crystal lattice and surface defects on the crystal surface in the catalyst could be observed after heat treatment or impurity doping. Photocatalysis active centers in catalyst often have a close relationship with these lattice defects [9, 26, 33, 70, 106, 107].

In general, the surface defects of particles are the active centers, where electron donors and electron acceptors are highly concentrated. Therefore, the presence of moderate surface defects is beneficial to the photocatalytic activity. Bulk defects are the main place for electron-hole recombination. The increasing of bulk defects may have negative effects on photocatalytic activity.

1.4 Modification of perovskite catalyst

Taking titanium dioxide as an example, anatase-type titanium dioxide has strongest photocatalytic activity with high chemical stability, low cost, and harmless to the human body. It has been gradually used in wastewater treatment, water purification and air purification. TiO_2 also shows the ability of non-selectively degradation of almost all organic compounds at room temperature. However, the commercial nanopowders, due to its relatively large particle size, small specific surface area, and wide band gap, the utilization rate of sunlight is low. The recombination rate of electrons and holes generated by light excitation is high, which leads to the decrease of light quantum efficiency. In order to overcome the above shortcomings, people have conducted a lot of research, the main way is to modify.

1.4.1 Metal modification

Metal doping can introduce defects in the crystal lattice and change the crystallinity, thereby affecting the recombination rate of electrons and holes. If it is doped with transition metals which can change the valence, these transition metal ions can form a shallow potential trap of photo-generated electron-hole pairs, prolong the recombination time of electrons and holes, thereby improving the photocatalytic activity [65, 106, 108-110]. In addition, transition metal ions usually have a wider light absorption range, which can extend the absorbed light to the visible light region. In order to achieve better results, the dopant should be able to capture electrons and holes at the same time, so that they can be separated locally. In Pham et al.'s reach, Mo was introduced to modify nickel titanate and proved that Mo doping can effectively inhibit the recombination in the composite photocatalyst [106]. Mi et al report that Ag-coupling and V-doping NiTiO_3 nanorods have a smaller band energy compare with the pure NiTiO_3 and the photocatalytic activities of photodegradation of Rhodamine was enhanced after modification [108]. The dopant concentration also has a great influence on the reaction activity, and there is an optimal concentration value. Excessive doping concentration has negative effect on the reaction. Conversely, too low doping concentration hard to provide enough traps which will reduce the rate of reactivity.

Precious metal deposition is also a good choice. When the precious metal is deposited on the surface of the catalysts, the electrons generated by the light excitation will be transferred to the precious metal, and then the oxidizing component adsorbed

on the surface of the precious metal will be reduced, and the reducing component will be oxidized by the photo-generated holes on the surface. Thereby avoiding the recombination of electrons and holes, effectively improving the photoactivity. In addition, noble metals themselves have high catalytic activity, it can modify the photocatalytic properties of semiconductors by changing the distribution of electrons. Generally speaking, the work function of the deposited precious metal is higher, so when the two materials are connected together, the electrons will continue to migrate from the catalyst to the deposited metal until the Fermi energy levels of the two are equal. A shallow potential well schottky energy barrier that can trap electrons is formed at the metal-catalyst interface, which can further inhibit the recombination of photo-generated electrons and holes. Liu et al. reported a high stability and efficient Pt/NaNbO₃ nanowire photocatalyst for H₂ production [69]. Thiagarajan et al prepared Pt-Ru-NiTiO₃ nanoparticles for the methanol oxidation reaction via two-step procedure using a wet chemical method and found that the addition of Ru enhances the methanol oxidation reaction [111].

1.4.2 Semiconductor heterojunction structure

Two kinds of semiconductor catalysis could form a heterojunction structure. This kind of semiconductor recombination is carried out by recombining two kinds of semiconductors with different band gap widths. The heterojunction structure can not only provide active centers for reactants and reaction intermediates, but also change the band structure, help change the band gap absorption and separate light-excited electron-hole pairs. There are many factors that affect the band bending between two semiconductors, including doping type, concentration, particle size and surface structure.

Wang et al designed hierarchically one-dimensional Zn_xCd_{1-x}S/NiTiO₃ nanofibers and the investigations of their photocatalytic of water splitting performance. The matched band alignments and hierarchical heterostructures enhanced the transfer and spatial separation of photogenerated electron hole pairs and provide superior photocatalytic performance [112]. Huang et al synthesized a series of NiTiO₃/TiO₂ with different NiTiO₃ contents by an in-situ reaction method for hydrogen generation from reaction and found that the composite structure enhanced the water splitting performance and optimum NiTiO₃ content is 1.77 mol.% [73].

Besides, graphitic carbon nitride (g-C₃N₄) also received more and more attention as semiconductor photocatalyst. This metal-free polymeric n-type semiconductor exhibits a band gap of ca. 2.7 eV, high chemical stability, special electronic structure, good thermo-chemical stability and facile preparation. It has been widely used for organic pollution degradation, water splitting and photocatalytic CO₂ reduction. However, the poor visible light response and inefficient separation efficiency of photogenerated carriers limited the photocatalytic activity of pure g-C₃N₄ [93, 106, 113, 114]. GUO et al. use NiTiO₃/g-C₃N₄ photocatalyst to turn carbon dioxide into methanol. It was found that the increase of CH₃OH yield can be attributed to the coupling structure reform by NiTiO₃ and g-C₃N₄ which inhibit the recombination of charge carriers, keep redox ability and enhance the spatial separation of hole-electron pairs [115].

1.5 Motivation

Nowadays, public concern about sustainable development of human society issues is high, especially environmental problems and energy problem. Catalysis is an important phenomenon that exists widely in nature, which plays an important role in the maintenance of life and the circulation of matter. Developing better catalysts and catalytic technology may be the key to solving these problems.

Every year, the solar energy that irradiates on the earth's surface is about 10²⁴ J, which far exceeds the global annual energy consumption. The development of photocatalyst technology about finding effective way to storage, transfer and utilization of solar energy is of great significance to the sustainable development of mankind. The two main processes of photocatalysis are light absorption and carrier transfer. Researchers will improve the performance of materials through kinds of modification way like element doping or semiconductor loading. However, some methods have complex synthesis process, high cost, or certain environmental pollution. Among many materials, perovskite materials NiTiO₃ have attracted attention due to their special electronic structure, unique photophysical and chemical properties.

In addition to the development and utilization of solar energy, the treatment of carbon dioxide has always been a hot topic of research. Excessive carbon dioxide emission due to over-consumption of fossil fuels of modern industry has caused severe environmental problems such as ocean acidification and global warming. Methanation

of carbon dioxide to methane could be a promising way for sustainable development. NiTiO₃ perovskite material provide controllable structure, and Ni is also primarily used as the catalyst for carbon dioxide methanation. This article also attempts to expand the application of perovskite materials in the energy field.

1 Photocatalytic Decomposition of Toluene by NiTiO₃

In the first work, nickel titanate (NTN) photocatalyst was prepared by a facile synthesis process with microwave method for photocatalytic decomposition of gas phase toluene. P25, a commercial photocatalyst, was also employed for the photocatalytic decomposition to compare their photocatalytic performance. P25 showed better catalytic performance under UV irradiation, while NTN exhibited a higher reaction rate constant under visible light irradiation. Moreover, NTN generated more CO₂ after the photocatalytic reaction than P25. From XRD patterns and Raman spectra, P25 consisted of anatase and rutile TiO₂ structures and NTN existed pure nickel titanate structure. Based on UV-Vis spectra, the bandgaps of P25 and NTN were obtained at 3.2 and 2.47 eV, respectively, implying that NTN would be a visible light-responded photocatalyst.

2 Modification of NiTiO₃ materials by transition metal dopants: The dopant size effect

In this study, we investigated the changes of the structural and optical properties of NiTiO₃ materials modified by transition metal doping. cobalt or tungsten-doped NiTiO₃ materials were successfully prepared by a modified Pechini method via solvothermal treatment. Raman, FTIR, and XRD spectroscopic analyses showed that the Co²⁺ ions were selectively doped into Ni²⁺ sites in the NiTiO₃ lattice while maintaining an ilmenite structure, resulting in a solid solution of triple transition metal oxides. The size similarity between Co and Ni induced the formation of a solid solution, Co_xNi_{1-x}TiO₃, in the ilmenite structure. In contrast, W doping into the NiTiO₃ ilmenite structure resulted in an irregularity of the materials due to the characteristics of the heavy transition metal dopant. Along with increasing the W content, the crystallite size in the ilmenite structure decreased from 90.2 to 74.5 nm and new Raman bands at 831 and 892 cm⁻¹ for WO_x appeared at high W contents. However, the PL emission intensities gradually decreased with increasing doping content, implying that the recombination process was inhibited in the NiTiO₃ materials by the dopants.

3 Modification of NiTiO₃ by Nb doping and NbO_x heterojunction: Effect of oxygen vacancy

In this research, Nb-doped NiTiO₃ and NbO_x/NiTiO₃ photocatalysts are prepared with various Nb amounts to enhance photocatalytic activity for dye photodegradation under visible light irradiation. Nb-doped NiTiO₃ exhibits higher photocatalytic activity than pure NiTiO₃, whereas the inappropriate band structures of NbO_x and NiTiO₃ decrease photocatalytic activity. Incorporation of Nb into the NiTiO₃ lattice induces Ti³⁺ sites and oxygen vacancies. Eventually, the Nb-doped NiTiO₃ photocatalyst at the highest Nb content sample was transformed into a triple metal oxide phase with the highest surface area and oxygen vacancy. The abundant oxygen vacancy of NT-Nb-10 resulted in the lowest photoluminescence emission intensity, which resulted in the highest apparent photocatalytic reaction rate constant (k_{app}) of 14.1 min⁻¹ owing to the suppression of the recombination process. The formation of the triple metal oxide phase in this study may allow a potential way to modify low cost visible light-driven NiTiO₃ photocatalysts for sustainable photocatalytic application.

4 Highly stable and selective Co_xNi_yTiO₃ for CO₂ methanation

CO₂ methanation with Sabatier reaction is an effective way to convert the greenhouse gases into valuable industrial product. In this work, we designed and developed a stable and effective Co modified NiTiO₃ catalyst. The best catalyst exhibits high CO₂ conversion (86%) and high methane selectivity (nearly 100%), which can work continuously for 16 hours without significant deactivation at 350 °C. As evidenced by various characterization methods, like XPS, H₂-TPD and CO₂-TPR, Co doping are found to influence the electron distribution of the catalyst, change the size of metal particle and the interaction of metal and support, which in turn has positive impact on methanation performance, while NiTiO₃ support improve the ability to capture CO₂ because of its abundant basic oxide and oxygen vacancies after reduction. Cobalt modification proved to be an potential way to construct Ti-O-Ni interfacial structure, and increase the hydrogen activation site and carbon dioxide activation site simultaneously. This work may provide ideas for the synthesis of multi-metal modified catalysts.

References

- [1] R. Daghrir, P. Drogui, D. Robert, Modified TiO₂ For Environmental Photocatalytic Applications: A Review, *Ind. Eng. Chem. Res.*, 52 (2013) 3581-3599.
- [2] A. Naldoni, M. Altomare, G. Zoppellaro, N. Liu, Š. Kment, R. Zbořil, P. Schmuki, Photocatalysis with Reduced TiO₂: From Black TiO₂ to Cocatalyst-Free Hydrogen Production, *ACS catal.*, 9 (2019) 345-364.
- [3] P.K. de Bokx, R.L.C. Bonne, J.W. Geus, Strong metal-support interaction in Ni/TiO₂ catalysts: The origin of TiO_x moieties on the surface of nickel particles, *Appl. Catal.*, 30 (1987) 33-46.
- [4] M. Aresta, A. Dibenedetto, A. Angelini, Catalysis for the Valorization of Exhaust Carbon: from CO₂ to Chemicals, Materials, and Fuels. Technological Use of CO₂, *Chem. Rev.*, 114 (2014) 1709-1742.
- [5] K. Saravanan, H. Ham, N. Tsubaki, J.W. Bae, Recent progress for direct synthesis of dimethyl ether from syngas on the heterogeneous bifunctional hybrid catalysts, *Appl. Catal. B Environ.*, 217 (2017) 494-522.
- [6] Q.X. Yang, A. Skrypnik, A. Matvienko, H. Lund, M. Holena, E.V. Kondratenko, Revealing property-performance relationships for efficient CO₂ hydrogenation to higher hydrocarbons over Fe-based catalysts: Statistical analysis of literature data and its experimental validation, *Appl. Catal. B Environ.*, 282 (2021) 11.
- [7] J.J. Gao, Q. Liu, F.N. Gu, B. Liu, Z.Y. Zhong, F.B. Su, Recent advances in methanation catalysts for the production of synthetic natural gas, *RSC Adv.*, 5 (2015) 22759-22776.
- [8] M. Saric, J.W. Dijkstra, W.G. Haije, Economic perspectives of Power-to-Gas technologies in bio-methane production, *J. CO₂ Util.*, 20 (2017) 81-90.
- [9] T. Jomjaree, P. Sintuya, A. Srifa, W. Koo-amornpattana, S. Kiatphuengporn, S. Assabumrungrat, M. Sudoh, R. Watanabe, C. Fukuhara, S. Ratchahat, Catalytic performance of Ni catalysts supported on CeO₂ with different morphologies for low-temperature CO₂ methanation, *Catal. Today*, (2020).
- [10] A.H. Zamani, R. Ali, W.A.W. Abu Bakar, Optimization of CO₂ methanation reaction over M*/Mn/Cu–Al₂O₃ (M*: Pd, Rh and Ru) catalysts, *J. Ind. Eng. Chem.*, 29 (2015) 238-248.
- [11] Y. Yang, J. Liu, F. Liu, D. Wu, Reaction mechanism of CO₂ methanation over Rh/TiO₂ catalyst, *Fuel*, 276 (2020) 118093.

- [12] Y. Tang, Y. Wei, Z. Wang, S. Zhang, Y. Li, L. Nguyen, Y. Li, Y. Zhou, W. Shen, F.F. Tao, P. Hu, Synergy of Single-Atom Ni-1 and Ru-1 Sites on CeO₂ for Dry Reforming of CH₄, *J. Am. Chem. Soc.*, 141 (2019) 7283-7293.
- [13] J.N. Armor, A history of industrial catalysis, *Catal. Today*, 163 (2011) 3-9.
- [14] J.N. Appaturi, R.J. Ramalingam, M. Selvaraj, S. Chia, S.H. Tan, F. Khoerunnisa, T.C. Ling, E.-P. Ng, Selective synthesis of triacetyl glyceride biofuel additive via acetylation of glycerol over NiO-supported TiO₂ catalyst enhanced by non-microwave instant heating, *Appl. Surf. Sci.*, 545 (2021) 149017.
- [15] X.Y. Ooi, L.E. Oi, M.-Y. Choo, H.C. Ong, H.V. Lee, P.L. Show, Y.-C. Lin, J.C. Juan, Efficient deoxygenation of triglycerides to hydrocarbon-biofuel over mesoporous Al₂O₃-TiO₂ catalyst, *Fuel Process. Technol.*, 194 (2019) 106120.
- [16] S. L., A. K., R. V., J.A. B.M., Synthesis, characterization and application of TiO₂-Bi₂WO₆ nanocomposite photocatalyst for pretreatment of starch biomass and generation of biofuel precursors, *J. Environ. Chem. Eng.*, 6 (2018) 3306-3321.
- [17] J. Tian, T. Yan, Z. Qiao, L. Wang, W. Li, J. You, B. Huang, Anion-exchange synthesis of Ag₂S/Ag₃PO₄ core/shell composites with enhanced visible and NIR light photocatalytic performance and the photocatalytic mechanisms, *Appl. Catal. B Environ.*, 209 (2017) 566-578.
- [18] X. Li, Z. Ge, F. Xue, H. Liu, B. Lyu, M. Liu, Lattice-oriented contact in Pd/SrTiO₃ heterojunction for rapid electron transfer during photocatalytic H₂ production, *Mater. Res. Bull.*, 123 (2020) 110722.
- [19] D.-C. Liu, D.-C. Zhong, T.-B. Lu, Non-noble metal-based molecular complexes for CO₂ reduction: From the ligand design perspective, *EnergyChem*, 2 (2020) 100034.
- [20] M. Pudukudy, Z. Yaakob, Z.S. Akmal, Direct decomposition of methane over SBA-15 supported Ni, Co and Fe based bimetallic catalysts, *Appl. Surf. Sci.*, 330 (2015) 418-430.
- [21] A. Vita, C. Italiano, L. Pino, M. Lagana, M. Ferraro, V. Antonucci, High-temperature CO₂ methanation over structured Ni/GDC catalysts: Performance and scale-up for Power-to-Gas application, *Fuel Process. Technol.*, 202 (2020).
- [22] Z. Yan, Q. Liu, L. Liang, J. Ouyang, Surface hydroxyls mediated CO₂ methanation at ambient pressure over attapulgite-loaded Ni-TiO₂ composite catalysts with high activity and reuse ability, *J. CO₂ Util.*, 47 (2021) 101489.
- [23] Y. Wang, X. Chen, Q. Wang, Y. Zeng, K. Liao, S. Zhang, Q. Zhong, Novel 3D hierarchical bifunctional NiTiO₃ nanoflower for superior visible light photoreduction

performance of CO₂ to CH₄ and high lithium storage performance, *Energy*, 169 (2019) 580-586.

[24] L. Zhang, X.G. Wang, C.J. Chen, X.J. Zou, X.F. Shang, W.Z. Ding, X.G. Lu, Investigation of mesoporous NiAl₂O₄/MO_x (M = La, Ce, Ca, Mg)-gamma-Al₂O₃ nanocomposites for dry reforming of methane, *RSC Adv.*, 7 (2017) 33143-33154.

[25] S. Roensch, J. Schneider, S. Matthischke, M. Schlueter, M. Goetz, J. Lefebvre, P. Prabhakaran, S. Bajohr, Review on methanation - From fundamentals to current projects, *Fuel*, 166 (2016) 276-296.

[26] Z. Bian, Y.M. Chan, Y. Yu, S. Kawi, Morphology dependence of catalytic properties of Ni/CeO₂ for CO₂ methanation: A kinetic and mechanism study, *Catal. Today*, 347 (2020) 31-38.

[27] P. Shafiee, S.M. Alavi, M. Rezaei, Solid-state synthesis method for the preparation of cobalt doped Ni-Al₂O₃ mesoporous catalysts for CO₂ methanation, *Int. J. Hydrog. Energy*, 46 (2021) 3933-3944.

[28] R. Darouhegi, F. Meshkani, M. Rezaei, Enhanced low-temperature activity of CO₂ methanation over ceria-promoted Ni-Al₂O₃ nanocatalyst, *Chem. Eng. Sci.*, 230 (2021), 116194

[29] S. He, H. Wu, W. Yu, L. Mo, H. Lou, X. Zheng, Combination of CO₂ reforming and partial oxidation of methane to produce syngas over Ni/SiO₂ and Ni-Al₂O₃/SiO₂ catalysts with different precursors, *J. Hydrog. Energy*, 34 (2009) 839-843.

[30] J.Y. Do, N.-K. Park, M.W. Seo, D. Lee, H.-J. Ryu, M. Kang, Effective thermocatalytic carbon dioxide methanation on Ca-inserted NiTiO₃ perovskite, *Fuel*, 271 (2020). 117624

[31] W. Zhan, Q. He, X. Liu, Y. Guo, Y. Wang, L. Wang, Y. Guo, A.Y. Borisevich, J. Zhang, G. Lu, S. Dai, A Sacrificial Coating Strategy Toward Enhancement of Metal-Support Interaction for Ultrastable Au Nanocatalysts, *J. Am. Chem. Soc.*, 138 (2016) 16130-16139.

[32] K. Cao, M. Gong, J. Yang, J. Cai, S. Chu, Z. Chen, B. Shan, R. Chen, Nickel catalyst with atomically-thin meshed cobalt coating for improved durability in dry reforming of methane, *J. Catal.*, 373 (2019) 351-360.

[33] X.Y. Jia, X.S. Zhang, N. Rui, X. Hu, C.J. Liu, Structural effect of Ni/ZrO₂ catalyst on CO₂ methanation with enhanced activity, *Appl. Catal. B Environ.*, 244 (2019) 159-169.

- [34] M. Akatsuka, Y. Kawaguchi, R. Itoh, A. Ozawa, M. Yamamoto, T. Tanabe, T. Yoshida, Preparation of Ga₂O₃ photocatalyst highly active for CO₂ reduction with water without cocatalyst, *Appl. Catal. B Environ.*, 262 (2020) 118247.
- [35] M.I. Hossain, A.M. Saleque, S. Ahmed, I. Saidjafarzoda, M. Shahiduzzaman, W. Qarony, D. Knipp, N. Biyikli, Y.H. Tsang, Perovskite/perovskite planar tandem solar cells: A comprehensive guideline for reaching energy conversion efficiency beyond 30%, *Nano Energy*, 79 (2021) 105400.
- [36] K. Moore, W. Wei, Applications of carbon nanomaterials in perovskite solar cells for solar energy conversion, *Nano mater. sci.*, (2021).
- [37] M. Amoli-Diva, A. Anvari, R. Sadighi-Bonabi, Synthesis of magneto-plasmonic Au-Ag NPs-decorated TiO₂ -modified Fe₃O₄ nanocomposite with enhanced laser/solar-driven photocatalytic activity for degradation of dye pollutant in textile wastewater, *Ceram. Int.*, 45 (2019) 17837-17846.
- [38] D.P. Macwan, P.N. Dave, S. Chaturvedi, A review on nano-TiO₂ sol-gel type syntheses and its applications, *J. Mater. Sci.*, 46 (2011) 3669-3686.
- [39] C.B. Ong, L.Y. Ng, A.W. Mohammad, A review of ZnO nanoparticles as solar photocatalysts: Synthesis, mechanisms and applications, *Renew. Sust. Energ. Rev.*, 81 (2018) 536-551.
- [40] R. Ma, S. Zhang, T. Wen, P. Gu, L. Li, G. Zhao, F. Niu, Q. Huang, Z. Tang, X. Wang, A critical review on visible-light-response CeO₂-based photocatalysts with enhanced photooxidation of organic pollutants, *Catal. Today*, 335 (2019) 20-30.
- [41] H. Zhang, Y. Lu, W. Han, J. Zhu, Y. Zhang, W. Huang, Solar energy conversion and utilization: Towards the emerging photo-electrochemical devices based on perovskite photovoltaics, *Chem. Eng. J.*, 393 (2020) 124766.
- [42] A. Fujishima, K. Honda, Electrochemical Photolysis of Water at a Semiconductor Electrode, *Nature*, 238 (1972) 37-38.
- [43] W. Cui, L. Chen, J. Li, Y. Zhou, Y. Sun, G. Jiang, S.C. Lee, F. Dong, Ba-vacancy induces semiconductor-like photocatalysis on insulator BaSO₄, *Appl. Catal. B Environ.*, 253 (2019) 293-299.
- [44] M.C. Ariza-Tarazona, J.F. Villarreal-Chiu, V. Barbieri, C. Siligardi, E.I. Cedillo-González, New strategy for microplastic degradation: Green photocatalysis using a protein-based porous N-TiO₂ semiconductor, *Ceram. Int.*, 45 (2019) 9618-9624.

- [45] M. Tschurl, Semiconductor/Metal (Oxide) Hybrid Materials for Applications in Photocatalysis, in: K. Wandelt (Ed.) Encyclopedia of Interfacial Chemistry, Elsevier, Oxford, 2018, pp. 573-580.
- [46] U. Rafiq, K. Majid, Mitigating the charge recombination by the targeted synthesis of $\text{Ag}_2\text{WO}_4/\text{Bi}_2\text{Fe}_4\text{O}_9$ composite: The facile union of orthorhombic semiconductors towards efficient photocatalysis, *J. Alloys Compd.*, 842 (2020) 155876.
- [47] Z. Li, Z. Zhang, L. Wang, X. Meng, Bismuth chromate (Bi_2CrO_6): A promising semiconductor in photocatalysis, *J. Catal.*, 382 (2020) 40-48.
- [48] A. Bose, 1 - Three-Phase Alternating Current Systems, in: W.-K. Chen (Ed.) The Electrical Engineering Handbook, Academic Press, Burlington, 2005, pp. 709-711.
- [49] M. Alshehri, F. Al-Marzouki, A. Alshehrie, M. Hafez, Synthesis, characterization and band alignment characteristics of NiO/SnO_2 bulk heterojunction nanoarchitecture for promising photocatalysis applications, *J. Alloys Compd.*, 757 (2018) 161-168.
- [50] Z. Shayegan, F. Haghghat, C.-S. Lee, Surface fluorinated Ce-doped TiO_2 nanostructure photocatalyst: A trap and remove strategy to enhance the VOC removal from indoor air environment, *Chem. Eng. J.*, 401 (2020) 125932.
- [51] Z. Shayegan, F. Haghghat, C.-S. Lee, Anatase/brookite biphasic surface fluorinated Fe- TiO_2 photocatalysts to enhance photocatalytic removal of VOCs under visible and UV light, *J. Clean. Prod.*, 287 (2021) 125462.
- [52] P. Chen, W. Cui, H. Wang, X.a. Dong, J. Li, Y. Sun, Y. Zhou, Y. Zhang, F. Dong, The importance of intermediates ring-opening in preventing photocatalyst deactivation during toluene decomposition, *Appl. Catal. B Environ.*, 272 (2020) 118977.
- [53] C.H. Ao, S.C. Lee, J.Z. Yu, J.H. Xu, Photodegradation of formaldehyde by photocatalyst TiO_2 : effects on the presences of NO , SO_2 and VOCs, *Appl. Catal. B Environ.*, 54 (2004) 41-50.
- [54] M.T. Merajin, M. Nasiri, E. Abedini, S. Sharifnia, Enhanced gas-phase photocatalytic oxidation of n-pentane using high visible-light-driven Fe-doped WO_3 nanostructures, *J. Environ. Chem. Eng.*, 6 (2018) 6741-6748.
- [55] D. Jung, G. Kim, M.-S. Kim, B.-W. Kim, Evaluation of photocatalytic activity of carbon-doped TiO_2 films under solar irradiation, *Korean J. Chem. Eng.*, 29 (2012) 703-706.
- [56] M.A. Lillo-Ródenas, D. Cazorla-Amorós, A. Linares-Solano, Behaviour of activated carbons with different pore size distributions and surface oxygen groups for benzene and toluene adsorption at low concentrations, *Carbon*, 43 (2005) 1758-1767.

- [57] B. Liu, X. Li, Q. Zhao, J. Ke, J. Liu, S. Liu, M. Tade, Photocatalytic degradation of gaseous toluene with multiphase $Ti_xZr_{1-x}O_2$ synthesized via co-precipitation route, *J. Colloid Interface Sci.*, 438 (2015) 1-6.
- [58] J.-L. Shie, C.-H. Lee, C.-S. Chiou, Y.-H. Chen, C.-Y. Chang, Photocatalytic characteristic and photodegradation kinetics of toluene using N-doped TiO_2 modified by radio frequency plasma, *Environ. Tech.*, 35 (2014) 653-660.
- [59] J. Sun, X. Li, Q. Zhao, J. Ke, D. Zhang, Novel $V_2O_5/BiVO_4/TiO_2$ Nanocomposites with High Visible-Light-Induced Photocatalytic Activity for the Degradation of Toluene, *J.Phys.Chem.C*, 118 (2014) 10113-10121.
- [60] Z. Youssef, L. Colombeau, N. Yesmurzayeva, F. Baros, R. Vanderesse, T. Hamieh, J. Toufaily, C. Frochot, T. Roques-Carmes, S. Acherar, Dye-sensitized nanoparticles for heterogeneous photocatalysis: Cases studies with TiO_2 , ZnO, fullerene and graphene for water purification, *Dyes Pigm.*, 159 (2018) 49-71.
- [61] L. Wang, W. Fu, Y. Zhuge, J. Wang, F. Yao, W. Zhong, X. Ge, Synthesis of polyoxometalates (POM)/ TiO_2/Cu and removal of nitrate nitrogen in water by photocatalysis, *Chemosphere*, 278 (2021) 130298.
- [62] K. Wetchakun, N. Wetchakun, S. Sakulsermsuk, An overview of solar/visible light-driven heterogeneous photocatalysis for water purification: TiO_2 - and ZnO-based photocatalysts used in suspension photoreactors, *J. Ind. Eng. Chem.*, 71 (2019) 19-49.
- [63] I.J. Ochuma, O.O. Osibo, R.P. Fishwick, S. Pollington, A. Wagland, J. Wood, J.M. Winterbottom, Three-phase photocatalysis using suspended titania and titania supported on a reticulated foam monolith for water purification, *Catal. Today*, 128 (2007) 100-107.
- [64] R. Hou, Y. Gao, H. Zhu, G. Yang, W. Liu, Y. Huo, Z. Xie, H. Li, Coupling system of Ag/BiOBr photocatalysis and direct contact membrane distillation for complete purification of N-containing dye wastewater, *Chem. Eng. J.*, 317 (2017) 386-393.
- [65] K. Sharma, V. Dutta, S. Sharma, P. Raizada, A. Hosseini-Bandegharai, P. Thakur, P. Singh, Recent advances in enhanced photocatalytic activity of bismuth oxyhalides for efficient photocatalysis of organic pollutants in water: A review, *J. Ind. Eng. Chem.*, 78 (2019) 1-20.
- [66] Q. Zou, Z. Zhang, H. Li, W. Pei, M. Ding, Z. Xie, Y. Huo, H. Li, Synergistic removal of organic pollutant and metal ions in photocatalysis-membrane distillation system, *Appl. Catal. B Environ.*, 264 (2020) 118463.

- [67] F. Chen, D. Li, B. Luo, M. Chen, W. Shi, Two-dimensional heterojunction photocatalysts constructed by graphite-like C_3N_4 and Bi_2WO_6 nanosheets: Enhanced photocatalytic activities for water purification, *J. Alloys Compd.*, 694 (2017) 193-200.
- [68] Z. Xiong, J. Ma, W.J. Ng, T.D. Waite, X.S. Zhao, Silver-modified mesoporous TiO_2 photocatalyst for water purification, *Water Research*, 45 (2011) 2095-2103.
- [69] Q. Liu, Y. Chai, L. Zhang, J. Ren, W.-L. Dai, Highly efficient $Pt/NaNbO_3$ nanowire photocatalyst: Its morphology effect and application in water purification and H_2 production, *Appl. Catal. B Environ.*, 205 (2017) 505-513.
- [70] J. Pei, J. Meng, S. Wu, Q. Lin, J. Li, X. Wei, G. Han, Z. Zhang, Hierarchical $CaTiO_3$ nanowire-network architectures for H_2 evolution under visible-light irradiation, *J. Alloys Compd.*, 806 (2019) 889-896.
- [71] Y. Dou, A. Zhou, Y. Yao, S.Y. Lim, J.-R. Li, W. Zhang, Suppressing hydrogen evolution for high selective CO_2 reduction through surface-reconstructed heterojunction photocatalyst, *Appl. Catal. B Environ.*, 286 (2021) 119876.
- [72] K. Maeda, Direct splitting of pure water into hydrogen and oxygen using rutile titania powder as a photocatalyst, *ChemComm*, 49 (2013) 8404-8406.
- [73] J. Huang, Y. Jiang, G. Li, C. Xue, W. Guo, Hetero-structural $NiTiO_3/TiO_2$ nanotubes for efficient photocatalytic hydrogen generation, *Renewable Energy*, 111 (2017) 410-415.
- [74] Y. Fu, X. Zhu, L. Huang, X. Zhang, F. Zhang, W. Zhu, Azine-based covalent organic frameworks as metal-free visible light photocatalysts for CO_2 reduction with H_2O , *Appl. Catal. B Environ.*, 239 (2018) 46-51.
- [75] Q. Zhang, M. Mao, Y. Li, Y. Yang, H. Huang, Z. Jiang, Q. Hu, S. Wu, X. Zhao, Novel photoactivation promoted light-driven CO_2 reduction by CH_4 on Ni/CeO_2 nanocomposite with high light-to-fuel efficiency and enhanced stability, *Appl. Catal. B Environ.*, 239 (2018) 555-564.
- [76] B. Lin, A. Chaturvedi, J. Di, L. You, C. Lai, R. Duan, J. Zhou, B. Xu, Z. Chen, P. Song, J. Peng, B. Ma, H. Liu, P. Meng, G. Yang, H. Zhang, Z. Liu, F. Liu, Ferroelectric-field accelerated charge transfer in 2D $CuInP_2S_6$ heterostructure for enhanced photocatalytic H_2 evolution, *Nano Energy*, 76 (2020).
- [77] M. Moradi, F. Khorasheh, A. Larimi, Pt nanoparticles decorated Bi-doped TiO_2 as an efficient photocatalyst for CO_2 photo-reduction into CH_4 , *Solar Energy*, 211 (2020) 100-110.

- [78] M. Guo, X. Wang, L. Liu, X. Min, X. Hu, W. Guo, N. Zhu, J. Jia, T. Sun, K. Li, Recovery of cathode materials from spent lithium-ion batteries and their application in preparing multi-metal oxides for the removal of oxygenated VOCs: Effect of synthetic methods, *Environ. Res.*, 193 (2021) 110563.
- [79] Y.-J. Lin, Y.-H. Chang, G.-J. Chen, Y.-S. Chang, Y.-C. Chang, Effects of Ag-doped NiTiO₃ on photoreduction of methylene blue under UV and visible light irradiation, *J. Alloys Compd.*, 479 (2009) 785-790.
- [80] T.-T. Pham, S.G. Kang, E.W. Shin, Optical and structural properties of Mo-doped NiTiO₃ materials synthesized via modified Pechini methods, *Appl. Surf. Sci.*, 411 (2017) 18-26.
- [81] S.M. Hosseinpour-Mashkani, M. Maddahfar, A. Sobhani-Nasab, Novel Silver-doped NiTiO₃ : Auto-combustion Synthesis, Characterization and Photovoltaic Measurements, *South African J. Chem.-Suid-Afrikaanse Tydskrif Vir Chemie*, 70 (2017) 44-48.
- [82] N. Lenin, A. Karthik, M. Sridharpanday, M. Selvam, S.R. Srither, S. Arunmetha, P. Paramasivam, V. Rajendran, Electrical and magnetic behavior of iron doped nickel titanate (Fe³⁺/NiTiO₃) magnetic nanoparticles, *J. Magn. Magn. Mater.*, 397 (2016) 281-286.
- [83] Y. Zhang, J. Gu, M. Muruganathan, Y. Zhang, Development of novel α -Fe₂O₃/NiTiO₃ heterojunction nanofibers material with enhanced visible-light photocatalytic performance, *J. Alloys Compd.*, 630 (2015) 110-116.
- [84] R.P. Souza, T.K.F.S. Freitas, F.S. Domingues, O. Pezoti, E. Ambrosio, A.M. Ferrari-Lima, J.C. Garcia, Photocatalytic activity of TiO₂, ZnO and Nb₂O₅ applied to degradation of textile wastewater, *J. Photoch. Photobio. A*, 329 (2016) 9-17.
- [85] M. Azam, S. Yue, K. Liu, Y. Sun, J. Liu, K. Ren, Z. Wang, S. Qu, Z. Wang, Insights on the correlation of precursor solution, morphology of the active layer and performance of the perovskite solar cells, *J. Alloys Compd.*, 731 (2018) 375-380.
- [86] H. Ziaei-Azad, A. Khodadadi, P. Esmailnejad-Ahranjani, Y. Mortazavi, Effects of Pd on enhancement of oxidation activity of LaBO₃ (B=Mn, Fe, Co and Ni) perovskite catalysts for pollution abatement from natural gas fueled vehicles, *Appl. Catal. B Environ.*, 102 (2011) 62-70.
- [87] B. Paul, K.-H. Choo, Visible light active Ru-doped sodium niobate perovskite decorated with platinum nanoparticles via surface capping, *Catal. Today*, 230 (2014) 138-144.

- [88] T.-T. Pham, C. Nguyen-Huy, E.W. Shin, NiTiO₃/reduced graphene oxide materials synthesized by a two-step microwave-assisted method, *Mater. Lett.*, 184 (2016) 38-42.
- [89] B. Inceesungvorn, T. Teeranunpong, J. Nunkaew, S. Suntalelat, D. Tantraviwat, Novel NiTiO₃/Ag₃VO₄ composite with enhanced photocatalytic performance under visible light, *Catal. Commun.*, 54 (2014) 35-38.
- [90] J. Yan, G. Wu, N. Guan, L. Li, Nb₂O₅/TiO₂ heterojunctions: Synthesis strategy and photocatalytic activity, *Appl. Catal. B Environ.*, 152-153 (2014) 280-288.
- [91] J. Xing, Z. Shan, K. Li, J. Bian, X. Lin, W. Wang, F. Huang, Photocatalytic activity of Nb₂O₅/SrNb₂O₆ heterojunction on the degradation of methyl orange, *J Phys. Chem. Solids*, 69 (2008) 23-28.
- [92] R.A. Meyers, Authors, in: R.A. Meyers (Ed.) *Encyclopedia of Physical Science and Technology* (Third Edition), Academic Press, New York, 2003, pp. 1-32.
- [93] S.-R. Kim, W.-K. Jo, Application of a photostable silver-assisted Z-scheme NiTiO₃ nanorod/g-C₃N₄ nanocomposite for efficient hydrogen generation, *Int. J. Hydrog. Energy*, 44 (2019) 801-808.
- [94] S.K. Lakhera, H.Y. Hafeez, P. Veluswamy, V. Ganesh, A. Khan, H. Ikeda, B. Neppolian, Enhanced photocatalytic degradation and hydrogen production activity of in situ grown TiO₂ coupled NiTiO₃ nanocomposites, *Appl. Surf. Sci.*, 449 (2018) 790-798.
- [95] M.-W. Li, J.-P. Yuan, X.-M. Gao, E.-Q. Liang, C.-Y. Wang, Structure and optical absorption properties of NiTiO₃ nanocrystallites, *Appl. Phys. A*, 122 (2016) 725.
- [96] J. Singh, U.K. Goutam, A. Kumar, Hydrothermal synthesis and electrochemical performance of nanostructured cobalt free La₂CuMnO₆, *Solid State Sci.*, 95 (2019) 105927.
- [97] K. Agilandeswari, A. Ruban Kumar, Synthesis, characterization, microstructure, optical and magnetic properties of strontium cobalt carbonate precursor and Sr₂Co₂O₅ oxide material, *Superlattices Microst.*, 68 (2014) 27-37.
- [98] S. Thakur, R. Rai, S. Sharma, Structural characterization and magnetic study of NiFe_xO₄ synthesized by co-precipitation method, *Mater. Lett.*, 139 (2015) 368-372.
- [99] H. Zhan, Z. Wu, N. Zhao, W. Liu, W. Wei, Structural properties and catalytic performance of the LaCuZn mixed oxides for CO₂ hydrogenation to methanol, *J. Rare Earths*, 36 (2018) 273-280.

- [100] A. Yamakata, J.J.M. Vequizo, Curious behaviors of photogenerated electrons and holes at the defects on anatase, rutile, and brookite TiO₂ powders: A review, *J Photoch. Photobio. C*, 40 (2019) 234-243.
- [101] R. Kaplan, B. Erjavec, G. Dražić, J. Grdadolnik, A. Pintar, Simple synthesis of anatase/rutile/brookite TiO₂ nanocomposite with superior mineralization potential for photocatalytic degradation of water pollutants, *Appl. Catal. B Environ.*, 181 (2016) 465-474.
- [102] T. Ohno, T. Higo, H. Saito, S. Yuajn, Z. Jin, Y. Yang, T. Tsubota, Dependence of photocatalytic activity on aspect ratio of a brookite TiO₂ nanorod and drastic improvement in visible light responsibility of a brookite TiO₂ nanorod by site-selective modification of Fe³⁺ on exposed faces, *J Mol.Catal.A-Chem.*, 396 (2015) 261-267.
- [103] M.M. Abouelela, G. Kawamura, A. Matsuda, A review on plasmonic nanoparticle-semiconductor photocatalysts for water splitting, *J. Clean. Prod.*, 294 (2021) 126200.
- [104] L. Wang, J. Zhao, H. Liu, J. Huang, Design, modification and application of semiconductor photocatalysts, *J Taiwan Inst. Chem.Eng.*, 93 (2018) 590-602.
- [105] P.V. Kamat, N.M. Dimitrijević, Colloidal semiconductors as photocatalysts for solar energy conversion, *Solar Energy*, 44 (1990) 83-98.
- [106] T.-T. Pham, E.W. Shin, Inhibition of charge recombination of NiTiO₃ photocatalyst by the combination of Mo-doped impurity state and Z-scheme charge transfer, *Appl. Surf. Sci.*, 501 (2020) 143992.
- [107] G.I. Siakavelas, N.D. Charisiou, S. AlKhoori, A.A. AlKhoori, V. Sebastian, S.J. Hinder, M.A. Baker, I.V. Yentekakis, K. Polychronopoulou, M.A. Goula, Highly selective and stable nickel catalysts supported on ceria promoted with Sm₂O₃, Pr₂O₃ and MgO for the CO₂ methanation reaction, *Appl. Catal. B Environ.*, 282 (2021) 19.
- [108] L. Mi, Y. Huang, L. Qin, H.J. Seo, Improved photo-degradation of dyes over Ag-loaded NiTiO₃:V nanorods on visible-light-irradiation, *Mater. Res. Bull.*, 102 (2018) 269-276.
- [109] X. Xu, Y. Tong, J. Huang, J. Zhu, X. Fang, J. Xu, X. Wang, Insights into CO₂ methanation mechanism on cubic ZrO₂ supported Ni catalyst via a combination of experiments and DFT calculations, *Fuel*, 283 (2021) 118867.
- [110] Y. Yan, Y. Dai, H. He, Y. Yu, Y. Yang, A novel W-doped Ni-Mg mixed oxide catalyst for CO₂ methanation, *Appl. Catal. B Environ.*, 196 (2016) 108-116.

- [111] V. Thiagarajan, R. Manoharan, P. Karthikeyan, E. Nikhila, A. Hernandez-Ramirez, F.J. Rodriguez-Varela, Pt nanoparticles supported on NiTiO₃/C as electrocatalyst towards high performance Methanol Oxidation Reaction, *International Int. J. Hydrog. Energy*, 42 (2017) 9795-9805.
- [112] L. Wang, G. Yang, S. Wang, J. Wang, M.S. Nasir, C. Wang, S. Peng, W. Yan, S. Ramakrishna, Fabrication of hierarchically one-dimensional Zn_xCd_{1-x}S/NiTiO₃ nanostructures and their enhanced photocatalytic water splitting activity, *Int. J. Hydrog. Energy*, 44 (2019) 30974-30985.
- [113] T.-T. Pham, E.W. Shin, Thermal formation effect of g-C₃N₄ structure on the visible light driven photocatalysis of g-C₃N₄/NiTiO₃ Z-scheme composite photocatalysts, *Appl. Surf. Sci.*, 447 (2018) 757-766.
- [114] Y. Zeng, Y. Wang, J. Chen, Y. Jiang, M. Kiani, B. Li, R. Wang, Fabrication of high-activity hybrid NiTiO₃/g-C₃N₄ heterostructured photocatalysts for water splitting to enhanced hydrogen production, *Ceram. Int.*, 42 (2016) 12297-12305.
- [115] H. Guo, S. Wan, Y. Wang, W. Ma, Q. Zhong, J. Ding, Enhanced photocatalytic CO₂ reduction over direct Z-scheme NiTiO₃/g-C₃N₄ nanocomposite promoted by efficient interfacial charge transfer, *Chem. Eng. J.*, 412 (2021) 128646.

2 Photocatalytic decomposition of toluene by NiTiO₃ photocatalysts under visible-light irradiation

2.1 Introduction

Indoor air quality at home or inside car has been paid a great attention to due to continuous reports that even a small amount of volatile organic compounds (VOCs) is released from interior products in a car or at home and threatens the health of human beings [1]. Correspondingly, people request a free VOCs environment for indoor air condition and governmental regulation for indoor air quality becomes stricter. VOCs have been known as typical indoor air pollutants for long time and among diverse VOCs, toluene, a well known carcinogen like benzene and xylene has been issued due to increase in its concentration under indoor air condition [2].

Photocatalytic decomposition of toluene over photocatalysts is a powerful and attractive method for removing it from indoor air. Due to stability, non-toxicity, strong oxidative power, and low cost, TiO₂ is the best photocatalyst and has been used for photocatalytic decomposition of toluene in the gas phase in a number of research [3-8]. However, conventional TiO₂ photocatalysts are utilized only under UV light irradiation due to its wide band gap of 3.2 eV and therefore it is limited to be for used indoor air or inside vehicles. Recent trend in the developing of novel photocatalysts is to extend the photoresponse from UV to visible light and to enlarge photocatalytic efficiency under visible light irradiation. Nickel titanate (NiTiO₃, NTN) has been reported to show effective photocatalysis under visible light irradiation [9]. NTN is titanium-based perovskite oxides such as MTiO₃ (M = Ni, Sr, Ca and Ba) and belong to the ilmenite structure with a narrow band gap of approximately 2.18 eV, in which both Ni and Ti atoms prefer octahedral coordination with alternating cation layers solely occupied by either Ni or Ti [8-10]. There have been some studies to improve photocatalytic performance of NTN by controlling the morphology of NTN powder or by increasing the purity of NTN with different preparation methods [10-15].

In this study, we prepared a nickel titanate photocatalyst with high purity using a facile microwave-assisted method and applied it for photooxidation of gas phase toluene in air. For comparison, P25, a widely used commercial photocatalyst, was also employed for the photooxidation of toluene. In the results, the NTN photocatalyst exhibited better photodecomposition rate for toluene and more CO₂ generation under

visible light irradiation than P25, implying that it is a visible light-responded photocatalyst.

2.2 Experiment

2.2.1 Catalyst synthesis

Nickel Titanate photocatalysts was prepared by a microwave-assisted synthesis method. Nickel nitrate hexahydrate ($\text{NiNO}_3 \cdot 6\text{H}_2\text{O}$) (Sigma-Aldrich Korea) and titanium n-butoxide ($\text{Ti}(\text{OC}_4\text{H}_9)_4$) (Sigma-Aldrich Korea) were dissolved in to 50 ml ethylene glycol ($\text{C}_2\text{H}_6\text{O}$) (SK Chemicals) in a flask. A magnetic stirrer was used to improve dissolving. The homogeneous solution was sonicated for 1h and then it was transferred to a household microwave oven. At this stage the color of precursor mixture was light green. After irradiation (stage 1: 10 cycles, on 10s /off 15s , stage 2: 5 cycles, on 20s/off 20s), the yellowish-green mixture was cooled to room temperature immediately by water fluid. The precipitate was washed several times by water and collected by centrifugation (4000rpm, 15min). Finally the powder was dried at 80 °C overnight and calcined in high-pure nitrogen at 600°C for 5h (heating ramp: 2°C /min). The detailed description for the preparation of NTN was elsewhere. [16]

2.2.2 Catalyst characterization

The structure and morphology of the materials were determined by X-ray diffraction (XRD, Rigaku D/MAZX 2500V/PC high-power diffractometer, Japan). The XRD data for crystalline structure of the NTN and P25 were obtained in the 2θ range from 10° to 65°. Raman spectra were measured by DXR Raman spectrometer (ThermoFisher Scientific) under 632 nm laser excitation. The specific surface areas and pore volume of the samples were measured by Brunauer-Emmett-Teller (BET) and Barrett-Joyner-Halenda (BJH) with N_2 isotherms (Micromeritics ASAP2020 Surface Area and Porosity). The UV-vis absorption spectra of catalyst were determined by UV-vis spectrophotometer.

2.2.3 Photodegradation experiments

Photocatalytic decomposition of toluene by nickel titanate photocatalysts experiments were conducted by varying lamp source, separated by visible light region (20W

400nm~800nm) and ultraviolet region (20w 315nm~380nm). 0.1g catalyst was put into the 3L gas sampling bag and re-sealed this bag. Then a 10 μ l of liquid toluene (200 ppm) was injected into the reaction bag by a micro syringe. Keep the bag away from light until the toluene inside is completely converted into a gaseous state and reach adsorption equilibrium on catalyst surface. Recorded the amount of toluene as the initial concentration. After an hour in the dark box, turned the light on. The sample was analyzed by gas chromatogram (YL-6100, Porapack Q packed column 80/100) immediately every 40 min. The reaction time would lasted 4h.

2.3 Results and discussion

2.3.1 Structural properties of photocatalysts

The XRD patterns of the NTN and P25 are shown in Figure 2.1. The XRD peaks of P25 appearing at $2\theta = 25.3^\circ, 37.8^\circ, 48.0^\circ, 53.9^\circ, 55.1^\circ$ and 62.8° correspond the characteristic peaks of anatase TiO_2 structure, respectively (JCPDS 21-1272) [17,18]. In addition, some other characteristic peaks of titanium dioxide structure are also observed at $2\theta = 27.4^\circ, 36.1^\circ$ and 54.3° , representing rutile TiO_2 structure (JCPDS 21-1276). This indicates that P25 is an ordinary mixed structure of the anatase and rutile phase. NTN shows the peaks at $2\theta = 24.1^\circ, 33.1^\circ, 35.7^\circ, 40.8^\circ, 49.4^\circ$, and 54.0° , which correspond a rhombohedral nickel titanium oxide structure (JCPDS 33-0960), which also have a good agreement with previous reports [19,20]. There are almost no peaks observed on impurity level in the XRD patterns of NTN, implying that NTN is relatively a high purity material.

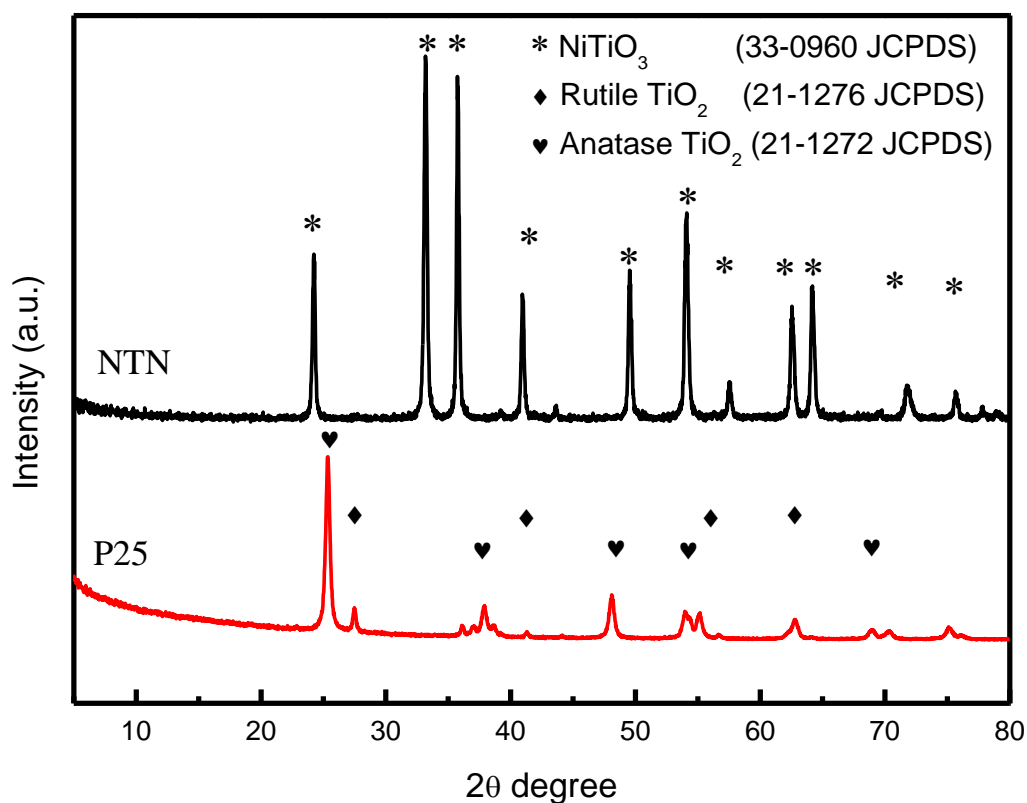


Figure 2.1 XRD patterns of NTN and P25

Figure 2.2 shows Raman spectra of the catalysts. The results are in good agreement with the XRD results. For P25, vibration frequencies were observed in the catalysts at 148, 203, 400, 509 and 619 cm⁻¹ corresponding to Eg(1), Eg(2), B1g(1), B1g(2), A1g and Eg(3) Raman active modes of tetragonal anatase TiO₂, respectively. As for NTN, nickel titanate characteristic bands were evidenced 189, 227, 242, 289, 344, 393, 461, 611, 705 and 764 cm⁻¹ showed the rhombohedral mode (5Ag+5Eg). Because of different synthesis method and the structural order degree, there are still some slight shifts of the some NiTiO₃ peaks can be observed [21].

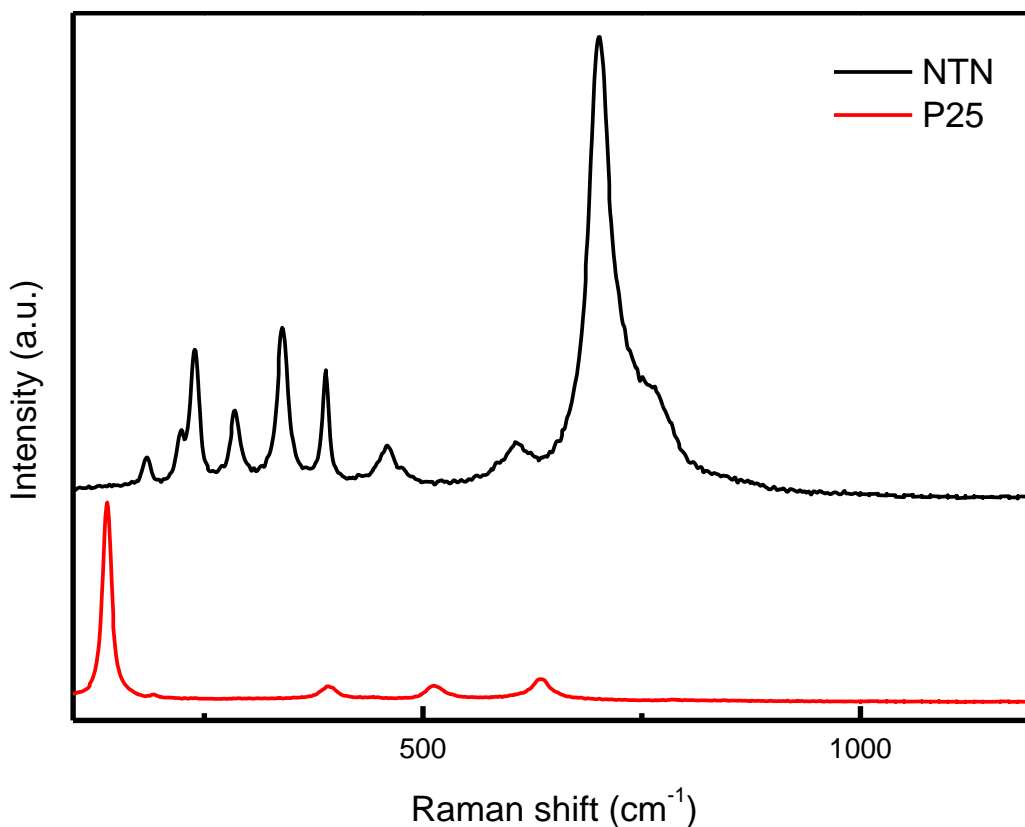


Figure 2.2. Raman spectra NTN and P25

The surface area and the pore volume for the catalysts are analysed and compared, as given in Table 2.1. The specific surface areas of NTN and P25 was 14.41 m^2/g ,53.35 m^2/g , respectively. The specific surface area of P25 is higher than that of NTN. The pore volumes also show the same tendency (0.1041 cm^3/g for NTN and 0.1501 cm^3/g for P25). These figures are similar to those reported previously [22].

Table 2.1 Properties and photocatalytic reaction rate constants (k_{app})

Samples	S_{BET}^a (m^2/g)	Pore Volume (cm^3/g)	Band gap ^b E(eV)	Constant k_{app}^c ($\times 10^{-3}min^{-1}$)	
				UV light	Vis-light
NTN	14.41	0.1041	2.19	2.4	4.8
P25	53.35	0.1501	3.2	3.9	0.8

^aSpecific surface areas were calculated from the fit of the Brunauer–Emmett–Teller (BET) equation for N_2 adsorption–desorption isotherms

^bThe values were obtained from the Tauc plot of UV-Vis spectra.

^cThe values were obtained from the fit of $-\ln(C/C_0)$ vs. t

Figure 2.3 shows the UV-Vis spectra of the two catalysts. When the wavelength was below 400nm, P25 showed a higher absorbance than NTN. For P25, a continuing increase ranging from 200 to 375 cm^{-1} was observed. This increase was particularly noticeable, where the intensity of the p25 was double than NTN. However, there was a significantly decline and almost disappear in the number of absorbance of P25 when the wavelength range was 400-800nm. This implied that the P25 has weak or even no photocatalytic activity. In the case of NTN catalyst, a wider range of light absorption in the visible region can be confirmed with this figure. The range from 400 to 800 saw an slightly upward trend in the intensity of absorbent, which shows the potential to be a efficient photocatalysts under visible light irradiation. On the other hand, with the method of Tauc plots, the band gap of NTN is estimated to about 2.19 eV, whereas the band gap of P25 to be about 3.2 eV (Table1). These results are in agreement to those previous reports (NTN 2.18ev) [23,24,25]. The result indicates that the fabricated material would enhance the visible light absorption, compared with P25 [26].

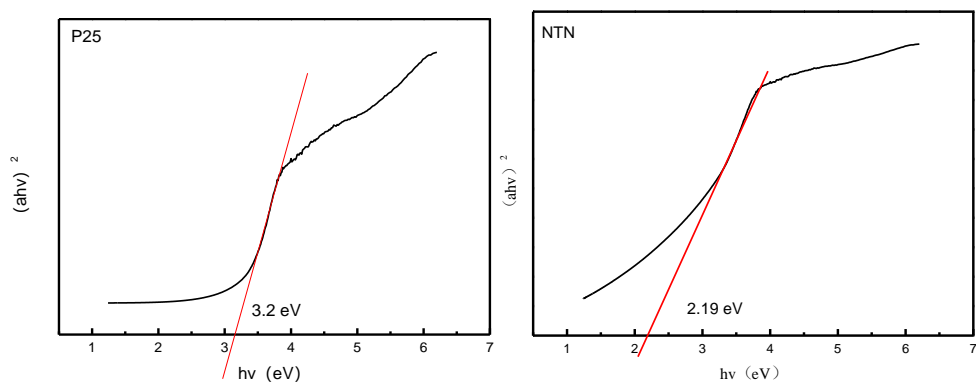
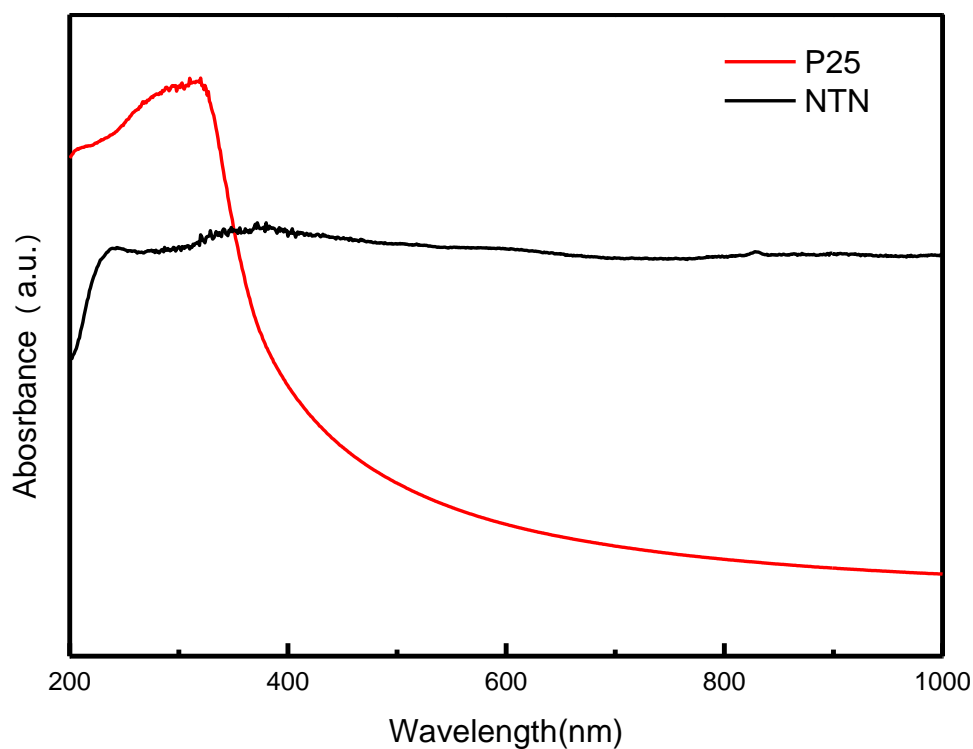


Figure 2.3 UV-VIS absorption spectra of NTN and P25

2.3.2 Optical properties of the photocatalysts

The toluene photodecomposition result of these catalysts are shown in Figure 2.4. The first 60 min had no observable decomposition result because of no irradiation. These four adsorption curves almost coincided with each other in this time, implying that there was no big difference in adsorption capacity between the catalysts. For P25, the toluene conversion was about 65% after 4 h reaction time under uv-light, while the removal efficiency was reduced to 20% when using the visible light irradiation. However, NTN shows the opposite trend under the same experimental conditions. The

toluene conversion were about 55% and 75% under uv-light and under vs-light, respectively.

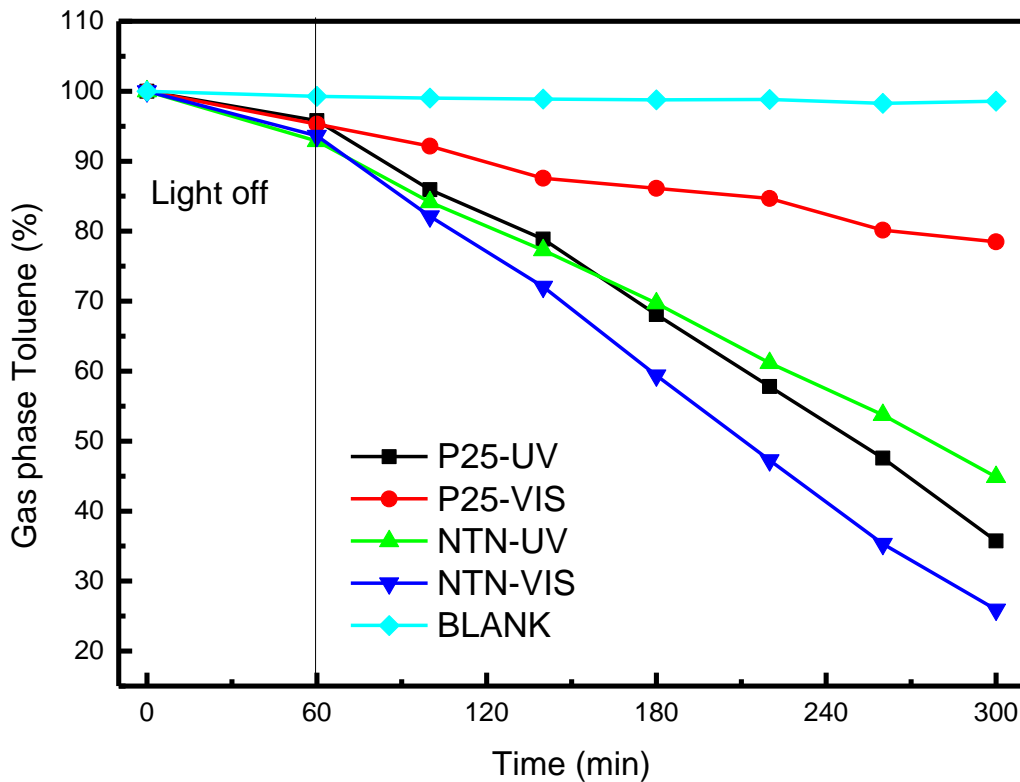


Figure 2.4 Photo-degradation of gas phase toluene

In order to quantitative analysis this photocatalytic reaction, Langmuir–Hinshelwood model was used to describe the reaction [27].

$$r = -\frac{dC}{dt} = \frac{k_a KC}{1 + KC}$$

This equation can be integrated between the limits:

$C = C_0$ at $t = 0$ and $C = C$ at $t = t$. The integrated expression is given by:

$$\ln\left(\frac{C_0}{C}\right) + K(C_0 - C) = k_a Kt$$

If the term $KC \ll 1$ then

$$r = k_a KC$$

L-H expression reduces to a first order kinetics and is given by[28]:

$$\ln \frac{C}{C_0} = -k_a t$$

Where C_0 and C_t are the initial concentration and concentration at time t for the toluene, respectively. k_a is apparent reaction rate constant.

k_a value of the P25 was measured to be $0.0008(\text{min}^{-1})$ under visible light and $0.0039(\text{min}^{-1})$ under UV irradiation (Figure 2.5). The result clearly showed that the P25 was an ultraviolet responsive photocatalyst. On the other hand, as for NTN, toluene photodecomposition showed a higher efficiency under vis-light ($k_a = 0.0048 \text{ min}^{-1}$) than in uv-light ($k_a = 0.0024 \text{ min}^{-1}$). Since the k_a was twice as high in vis-light as it was in uv-light, the NTN could be proved to be a vis-light photocatalyst. In addition, in this experiment, the apparent reaction rate constant k_a of NTN under vis-light was higher than the record rate constant of P25 under UV light, implying that NTN is a potential photocatalyst which can be commercialized under visible light irradiation. This result is better than previous research [29,30].

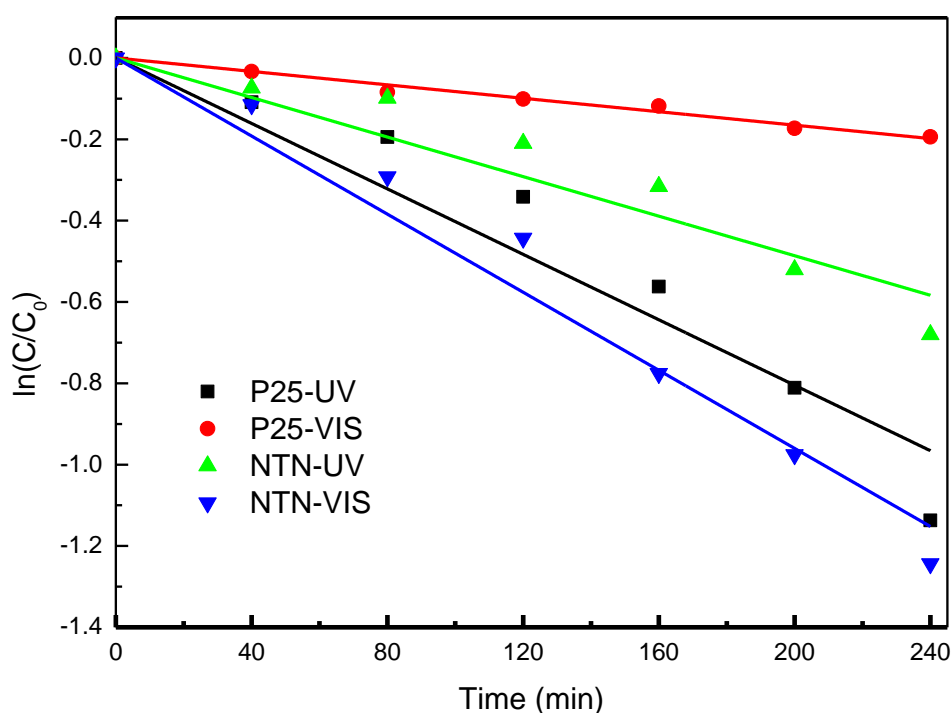


Figure 2.5 Photo-degradation of gas phase toluene(kinetic)

Figure 2.6 showed the concentration of carbon dioxide in the toluene photo-decomposition. carbon dioxide was the final product of toluene photodecomposition reaction, which could be consider as the key performance indicator when evaluating

the performance of the photocatalytic reaction. Without irradiation, for P25, no carbon dioxide could be detected on the first 60 min. While for NTN, a slight increase can be observed between 50-60 min. Since no light can be used to irradiate the photocatalyst, this point may be considered as a dating error. This result also agrees with the fact of low degradation rate of toluene in Fig5. NTN and P25 catalyze the production of carbon dioxide in different situations. For NTN, the concentration of CO₂ showed a sharp increase under visible light, while it showed a slight rise under UV light in the same reaction time. Irokawa confirmed that 89% of the toluene was photooxidized initially to CO₂ and H₂O under visible light irradiation, which shows a higher toluene degradation rate. It is noteworthy that at the end of the experiment, the concentration of CO₂ was 15 ppm, while there were 200 ppm of toluene in the first and the conversion of toluene was 75% [7]. This may be due to intermediates, such as oxalic, acetic, and formic acid, according to the reference, which means that the photocatalytic decomposition of toluene is not completely [7].

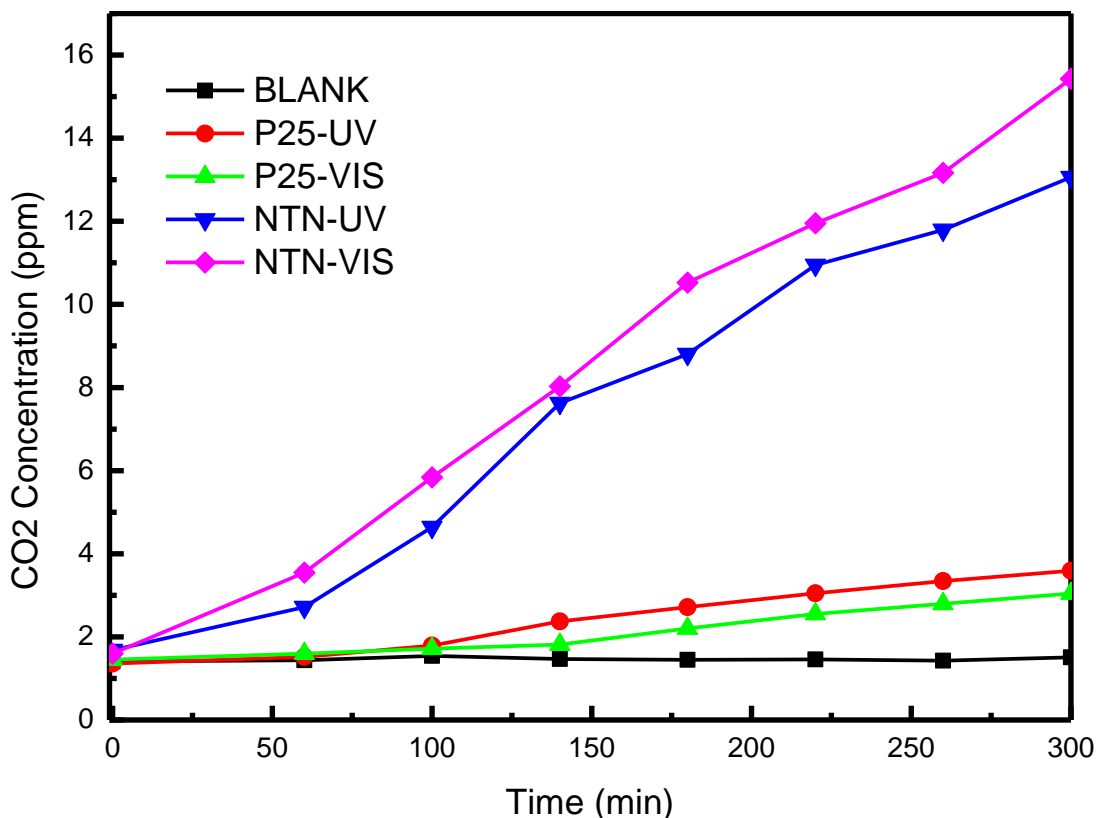


Figure 2.6 The CO₂ increase of effect on photo-degradation

2.4 Conclusions

In this study, a nickel titanate photocatalyst using a facile synthesis process with microwave method had been successfully synthesized. NTN exhibited higher reaction rate constant under visible light irradiation while P25 showed better catalytic performance under UV light. Ni metal provided a favorable photocatalytic activity under visible light irradiation. In addition, the bandgaps of P25 and NTN were obtained at 3.2 and 2.47 eV, implying that NTN would be a visible light-responded photocatalyst.

References

- [1] Jung, D., Kim, G., Kim, M. S., & Kim, B. W. Evaluation of photocatalytic activity of carbon-doped TiO₂ films under solar irradiation[J]. *Korean Journal of Chemical Engineering* 29 (2012) 703-706.
- [2] Lillo-Ródenas, M. A., Cazorla-Amorós, D., & Linares-Solano, A. Behaviour of activated carbons with different pore size distributions and surface oxygen groups for benzene and toluene adsorption at low concentrations[J]. *Carbon*, 43 (2005) 1758-1767.
- [3] Sun, J., Li, X., Zhao, Q., Ke, J., & Zhang, D. Novel V₂O₅/BiVO₄/TiO₂ nanocomposites with high visible-light-induced photocatalytic activity for the degradation of toluene[J]. *The Journal of Physical Chemistry C*, 118 (2014) 10113-10121.
- [4] Shie, J. L., Lee, C. H., Chiou, C. S., Chen, Y. H., & Chang, C. Y. Photocatalytic characteristic and photodegradation kinetics of toluene using N-doped TiO₂ modified by radio frequency plasma[J]. *Environmental technology*, 35 (2014) 653-660.
- [5] Kang, M., Kim, B. J., Cho, S. M., Chung, C. H., Kim, B. W., Han, G. Y., & Yoon, K. J. Decomposition of toluene using an atmospheric pressure plasma/TiO₂ catalytic system[J]. *Journal of molecular catalysis A: chemical*, 180 (2002) 125-132.
- [6] Liu, B., Li, X., Zhao, Q., Ke, J., Liu, J., Liu, S., & Tadé, M. Photocatalytic degradation of gaseous toluene with multiphase Ti_xZr_{1-x}O₂ synthesized via co-precipitation route[J]. *Journal of colloid and interface science*, 438 (2015) 1-6.
- [7] Irokawa, Y., Morikawa, T., Aoki, K., Kosaka, S., Ohwaki, T., & Taga, Y. Photodegradation of toluene over TiO_{2-x}N_x under visible light irradiation[J]. *Physical Chemistry Chemical Physics*, 8 (2006) 1116-1121.
- [8] Chen, C., Ma, W., & Zhao, J. Photocatalytic degradation of organic pollutants by co-doped TiO₂ under visible light irradiation[J]. *Current Organic Chemistry*, 14 (2010) 630-644.
- [9] Tada, H., Kiyonaga, T., & Naya, S. I. Rational design and applications of highly efficient reaction systems photocatalyzed by noble metal nanoparticle-loaded titanium (IV) dioxide[J]. *Chemical Society Reviews*, 38 (2009) 1849-1858.
- [10] Liu, X., Hong, R., & Tian, C. Tolerance factor and the stability discussion of ABO₃-type ilmenite[J]. *Journal of Materials Science: Materials in Electronics*, 20 (2009) 323-327.
- [11] Sadjadi, M. S., Zare, K., Khanahmadzadeh, S., & Enhessari, M. Structural characterization of NiTiO₃ nanopowders prepared by stearic acid gel method[J]. *Materials letters*, 62 (2008) 3679-3681.
- [12] Taylor, D. J., Fleig, P. F., & Page, R. A. Characterization of nickel titanate synthesized by sol-gel processing[J]. *Thin Solid Films*, 408 (2002) 104-110.

- [13] Phani, A. R., & Santucci, S. Structural characterization of iron titanium oxide synthesized by sol–gel spin-coating technique[J]. *Materials Letters*,50 (2001) 240-245.
- [14] Murugan, A. V., Samuel, V., Navale, S. C., & Ravi, V. Phase evolution of NiTiO₃ prepared by coprecipitation method[J]. *Materials letters*, 60 (2006) 1791-1792.
- [15] Lin, Y. J., Chang, Y. H., Yang, W. D., & Tsai, B. S. Synthesis and characterization of ilmenite NiTiO₃ and CoTiO₃ prepared by a modified Pechini method[J]. *Journal of non-crystalline solids*, 352 (2006) 789-794.
- [16] Nguyen-Phan T D, Huy C N, Kim C K, et al. Facile microwave-assisted synthesis and controllable architecture of three-dimensional nickel titanate[J]. *CrystEngComm*, 17 (2015) 4562-4574.
- [17] Liu, S., Sun, H., Liu, S., & Wang, S. Graphene facilitated visible light photodegradation of methylene blue over titanium dioxide photocatalysts[J]. *Chemical Engineering Journal*, 214 (2013) 298-303.
- [18] Jiang, G., Zheng, X., Wang, Y., Li, T., & Sun, X. Photo-degradation of methylene blue by multi-walled carbon nanotubes/TiO₂ composites[J]. *Powder Technology*, 207 (2011) 465-469.
- [19] Nguyen-Phan, T. D., Huy, C. N., Kim, C. K., & Shin, E. W. Facile microwave-assisted synthesis and controllable architecture of three-dimensional nickel titanate[J]. *CrystEngComm*.17 (2015) 4562-4574
- [20] Sadjadi, M. S., Zare, K., Khanahmadzadeh, S., & Enhessari, M. Structural characterization of NiTiO₃ nanopowders prepared by stearic acid gel method[J]. *Materials letters*, 62 (2008) 3679-3681.
- [21] Lopes, K. P., Cavalcante, L. S., Simões, A. Z., Varela, J. A., Longo, E., & Leite, E. R. NiTiO₃ powders obtained by polymeric precursor method: synthesis and characterization[J]. *Journal of Alloys and Compounds*, 468 (2009) 327-332.
- [22] Keshmiri, M., Troczynski, T., & Mohseni, M. Oxidation of gas phase trichloroethylene and toluene using composite sol–gel TiO₂ photocatalytic coatings[J]. *Journal of hazardous materials*,128 (2006) 130-137.
- [23] Grabowska, E. Selected perovskite oxides: Characterization, preparation and photocatalytic properties—A review[J]. *Applied Catalysis B: Environmental*, 186 (2016) 97-126.
- [24] Zhu, J., Li, H., Zhong, L., Xiao, P., Xu, X., Yang, X., ... & Li, J. Perovskite Oxides: Preparation, Characterizations, and Applications in Heterogeneous Catalysis[J]. *ACS Catalysis*, 4 (2014) 2917-2940.
- [25] Shu, X., He, J., & Chen, D. (2008). Visible-light-induced photocatalyst based on nickel titanate nanoparticles[J]. *Industrial & Engineering Chemistry Research*, 47, (2008) 4750-4753.

- [26] Qu, Y., Zhou, W., Ren, Z.8, Du, S., Meng, X., Tian, G., ... & Fu, H. Facile preparation of porous NiTiO₃ nanorods with enhanced visible-light-driven photocatalytic performance[J]. *Journal of Materials Chemistry*, 22(2012). 16471-16476.
- [27] Ching, W. H., Leung, M., & Leung, D. Y. (2004). Solar photocatalytic degradation of gaseous formaldehyde by sol-gel TiO₂ thin film for enhancement of indoor air quality[J]. *Solar Energy*, 77(2), 129-135.
- [28] Kumar, K. V., Porkodi, K., & Rocha, F. Langmuir-Hinshelwood kinetics—a theoretical study[J]. *Catalysis Communications*, 9 (2008) 82-84.
- [29] Bouzaza, A., & Laplanche, A. Photocatalytic degradation of toluene in the gas phase: comparative study of some TiO₂ supports[J]. *Journal of Photochemistry and Photobiology A: Chemistry*, 150 (2002) 207-212.
- [30] Kim, S. B., & Hong, S. C. Kinetic study for photocatalytic degradation of volatile organic compounds in air using thin film TiO₂ photocatalyst[J]. *Applied Catalysis B: Environmental*, 35 (2002) 305-315

3 Modification of the structural properties of NiTiO₃ materials by transition metal dopants (Co and W).

3.1 Introduction

Nickel titanate (NiTiO₃) is a double transition metal oxide which has an ilmenite structure in which the Ni and Ti atoms prefer octahedral coordination with alternating cation layers occupied exclusively by Ni²⁺ or Ti⁴⁺ [1-3]. NiTiO₃ is a promising candidate for visible light-driven photocatalysis due to its narrow band gap, where electrons in the material can be excited to the conduction band under visible light irradiation [4]. However, NiTiO₃ also has weaknesses such as a poor quantum efficiency and a fast recombination rate when applied as an individual phase photocatalyst.

To overcome the fast recombination rate, there have been several attempts to modify the properties of NiTiO₃ including the formation of a composite with carbon-based materials [4-6], the use of heterojunctions with inorganic nanoparticles [3], and metal doping into the ilmenite structure [1,7-11]. Among these, metal-doped NiTiO₃ can be readily obtained by various means, resulting in modifications of the optical or structural properties of the materials. NiTiO₃ doped by transition metals such as Fe, Mo, and Ag have been prepared and their properties characterized [1,7,8]. In Ag-doped NiTiO₃ materials, Ag²⁺ ions were not included in the NiTiO₃ ilmenite structure but precipitated on the surface as silver metal [1]. In the case of Mo-doped NiTiO₃ materials, the Mo doping changed the structural properties such as the grain size and optical properties, including its photoluminescence emission, thus maintaining the NiTiO₃ ilmenite structure [7]. For Fe/NiTiO₃ materials, the NiTiO₃ ilmenite structure was barely maintained in the presence of other iron-related phases [8]. Depending on the transition metal dopants, the properties of NiTiO₃ materials were modified in various ranges. Therefore, in order to further understand the effect of the transition metal dopants on the modification of the properties of NiTiO₃ materials, it is necessary to prepare other transition metal-doped NiTiO₃ materials and evaluate their properties.

In this study, two additional transition metals were chosen as dopants for the NiTiO₃ ilmenite structure: cobalt (Co) and tungsten (W), which are widely used as promoters in Ni- or Ti-based catalysts [12-15]. We prepared transition metal (Co or

W)-doped NiTiO₃ materials as a function of the metal dopant content *via* a modified Pechini method followed by a solvothermal treatment. We investigated the effects of transition metal doping on the optical and structural properties of the NiTiO₃ materials. Both of the transition metal-doped NiTiO₃ materials were successfully prepared, maintaining the NiTiO₃ ilmenite structure. However, due to the size of the transition metal dopant, the Co dopant was selectively doped into Ni²⁺ ion sites in the NiTiO₃ ilmenite structure, resulting in a solid solution of triple transition metal oxides, whereas the W dopant induced an irregularity in the NiTiO₃ ilmenite structure.

3.2 Experiment

3.2.1 Catalyst synthesis

In this work, the modified Pechini method was employed to fabricate pure and transition metal-doped NiTiO₃ materials. Citric acid monohydrate (C₆H₈O₇·H₂O) was purchased from OCI Company Ltd (Seoul, South Korea). Anhydrous ethyl alcohol (C₂H₅OH 99.9%) was purchased from Samchun Pure Chemical Company Ltd. (PyeongTaek, South Korea). Titanium n-butoxide (Ti(OC₄H₉)₄), nickel nitrate hexahydrate (Ni(NO₃)₂·6H₂O), and cobalt nitrate hexahydrate (Co(NO₃)₂·6H₂O) were purchased from Sigma-Aldrich Korea (Gyeonggi, South Korea). Tungsten (VI) isopropoxide, 5% w/v in isopropanol (W[OCH(CH₃)₂]₆), was purchased from Alfa Aesar (Great Britain).

The Co-doped NiTiO₃ materials were prepared by the following procedure. 0.75 g of citric acid was added to 100 ml of ethyl alcohol and magnetically stirred at room temperature for 15 min. Subsequently, cobalt nitrate hexahydrate and nickel nitrate hexahydrate were respectively dissolved in the mixture. Afterwards, titanium-butoxide, which was used as the titanium source, was added dropwise to this mixed aqueous solution. Each time a new chemical was added, the resulting solution was continuously stirred for 60 mins until a uniform mixture was achieved. The resultant mixture was then transferred to a Teflon-lined stainless-steel autoclave, which was kept at 160 °C for 6 h (ramp rate = 2 °C/min). After solvothermal treatment, the precipitate was collected via centrifugation, washed several times using ethyl alcohol, air dried overnight, grounded, and finally calcined at 600 °C for 5 h (ramp rate = 2 °C/min). The preparations of the W-doped NiTiO₃ materials utilized the same method except for using

tungsten(VI) isopropoxide as the W precursor. The final powder products were designated as Co-NT-x and W-NT-x, where x is the Co or W mass (x= 0, 3, 5, 7, and 10 wt.%) relative to the total weight of the Co-doped NiTiO₃ materials or W-doped NiTiO₃ materials.

3.2.2 Catalyst characterization

The crystalline structures of these products were determined via X-ray diffraction (XRD, Rigaku D/MAZX 2500V/PC high-power diffractometer, Japan) with a Cu Ka X-ray source (wavelength $\lambda = 1.5415 \text{ \AA}$, scanning rate of $2^\circ (2\theta)/\text{min}$). Raman spectra were obtained using a DXR Raman microscope (Thermo Fisher Scientific, USA) under 533 nm laser excitation. The Fourier transform infrared (FTIR) spectra of the materials were obtained using a Nicolet 380 spectrometer (Thermo Electron Co., USA). Photoluminescence (PL) measurements were performed at room temperature using a Cary Eclipse fluorescence spectrophotometer (Agilent Technologies, Australia). UV-vis diffuse reflectance spectra (UV-vis-DRS) were obtained using a SPECORD 210 Plus spectroscope (Analytik Jena, Germany). The morphologies of the materials were observed by field-emission scanning electron microscopy (FE-SEM, JSM- 600F, JEOL, Japan).

3.2.3 Photocatalysis and analyse

Photocatalytic activities were evaluated via the degradation of a methylene blue aqueous solution (MB, Sigma-Aldrich, CAS:7220-79-3) In a typical photocatalytic degradation, 10 mg of as-prepared catalysts were dispersed into 50 ml MB solution (initial concentration :5 mg/L) and transferred into a Quartz-made photoreactor which covered with aluminum foils to minimize the losses of light-energy. Subsequently, the solution was irradiated for 120 min with a 300 W xenon lamp coupled with a 420 nm cut-off filter at 15 cm away from the solution. For each analysis, 3.0 mL of liquid sample was collected 3 and filtered by a membrane filter to remove the catalyst particles. The MB concentrations for those samples were analyzed by absorbance at $\lambda_{\text{max}} = 664 \text{ nm}$ in a Quartz cuvette. Degradation efficiency (%) were determined by following.

$$\text{Degradation efficiency}(\%) = \frac{C(\text{concentration of MB at } t)}{C_0(\text{initial concentration of MB})}$$

3.3 Results and discussion

3.3.1 Structural properties of photocatalysts

The XRD patterns of all of the materials are shown in Figure 3.1. All samples clearly exhibited major characteristic peaks for the nickel titanium oxide phase at 2θ values of 33.1, 35.7, and 54.2, reflecting the maintenance of the ilmenite structure with an R3 space group (JCPDS No. 33-0960), regardless of the existence of the transition metal dopants. For Co doping (Co-NT-x), the NiTiO₃ ilmenite structure was the only phase observed in the XRD patterns without impurities or any great variation of the peak intensity (Fig. 3.1A). When W was doped, the same characteristic XRD peaks were also clearly detected without any impurity peaks (Fig. 3.1B). However, the XRD peak intensities decreased with increasing W content, implying a change of the crystallite size. The crystallite sizes in both materials were calculated using the Scherrer equation and the values are listed in Table 3.1. As shown in the table, the D values of the Co-doped NiTiO₃ ilmenite structure remained almost the same in the range of 90.3-95.7 nm, indicating no effect of Co doping on the NiTiO₃ crystallite size. In contrast, the D values of the W-NT-x materials decreased with increasing W content except for W-NT-5, indicating that the W doping induced the reduction of the NiTiO₃ crystallite size as a whole. This is similar to the behavior observed for Mo-doped NiTiO₃ materials [7]. The grain sizes and D values in Mo-doped NiTiO₃ materials decreased with increasing Mo content.

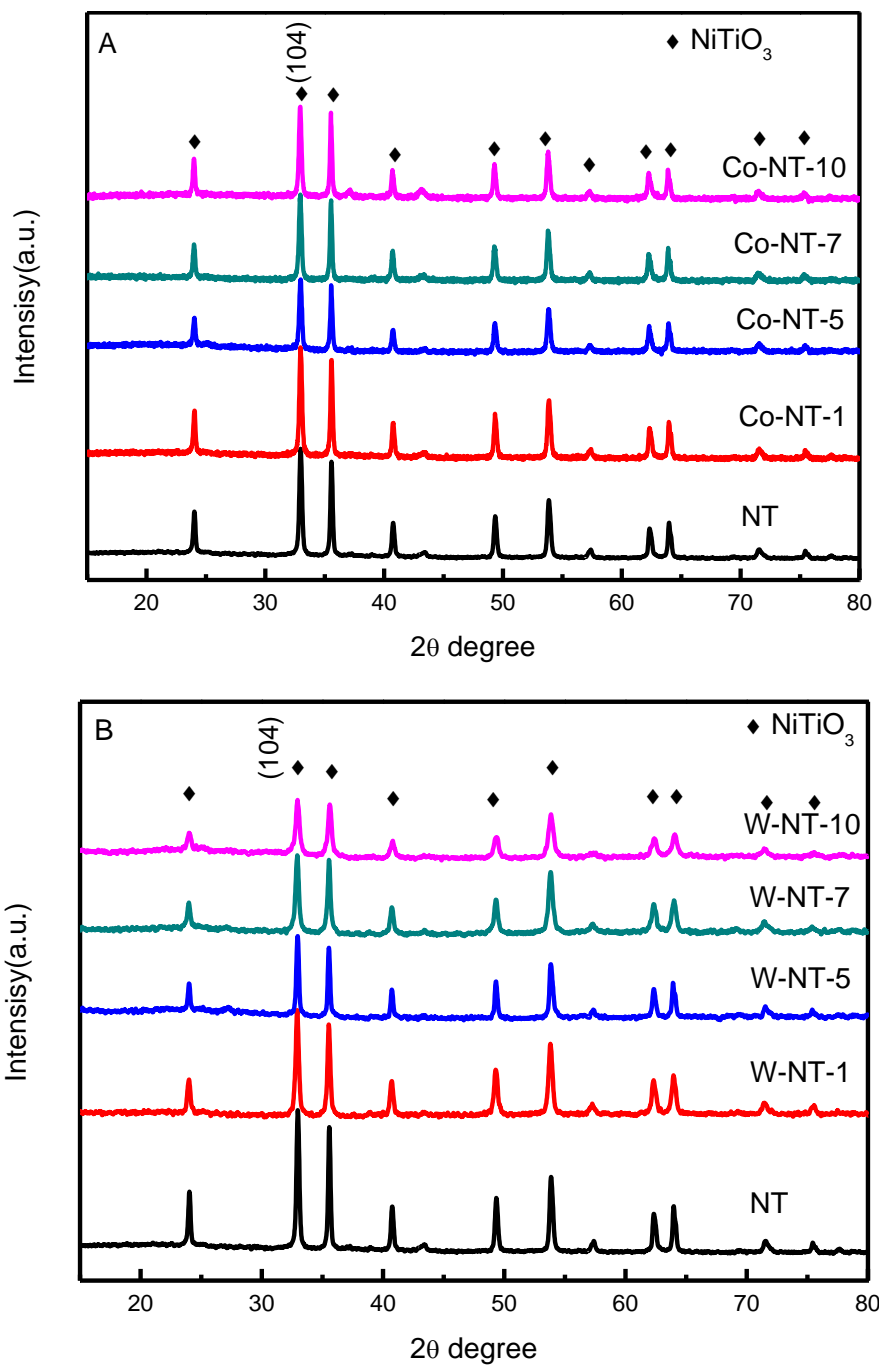


Figure 3.1 XRD patterns of the (A) Co-NT-x and (B) W-NT-x materials

Table 3.1 Properties of Co-NT-x and W-NT-x materials

Samples	Surface Area (m ² /g)	Pore Volume (cm ³ /g)	d(104), NT (nm)	Band gap (eV)
Co-NT-0 (W-NT-0)	11.46	0.093	90.28	2.48
Co-NT-3	14.64	0.078	90.57	1.91
Co-NT-5	16.96	0.088	93.16	2.25
Co-NT-7	18.42	0.103	94.26	2.68
Co-NT-10	13.77	0.092	95.72	2.55
W-NT-3	36.148	0.155	78.80	2.52
W-NT-5	12.92	0.093	99.79	2.12
W-NT-7	42.903	0.115	79.02	2.69
W-NT-10	51.954	0.140	74.51	2.82

The FE-SEM images of the materials reveal their morphologies. The FE-SEM images of the Co-NT-x materials show no variation of the grain sizes as a function of the Co concentration in Figure 3.2, which is in good agreement with the XRD results. Similarly, the FE-SEM images of the W-NT-x materials are also in good agreement with the XRD results. With increasing W content, the grain sizes of the W-NT-x materials decreased except for W-NT-5 in Figure 3.3. Moreover, the EDS elemental mapping results for Co-NT-7 and W-NT-7 confirmed the homogeneous distribution of each element including Co and W are shown in Figure 3.4 and Figure 3.5. The relative nominal and actual compositions (calculated from the EDS analysis) in the materials are additionally listed in Table 3.2.

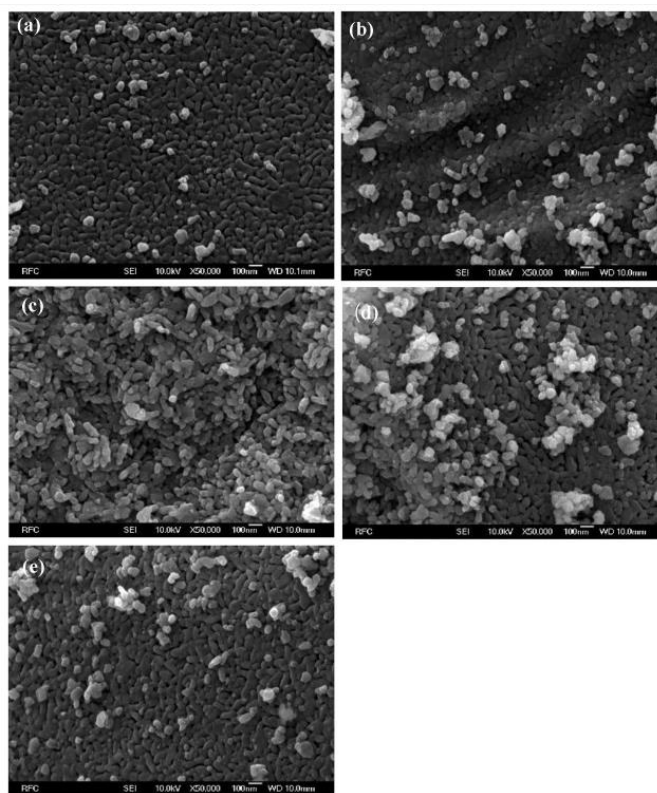


Figure 3.2 FE-SEM images of the Co-NT-x materials: (a) $x = 0$, (b) $x = 3$, (c) $x = 5$, (d) $x = 7$, and (e) $x = 10$.

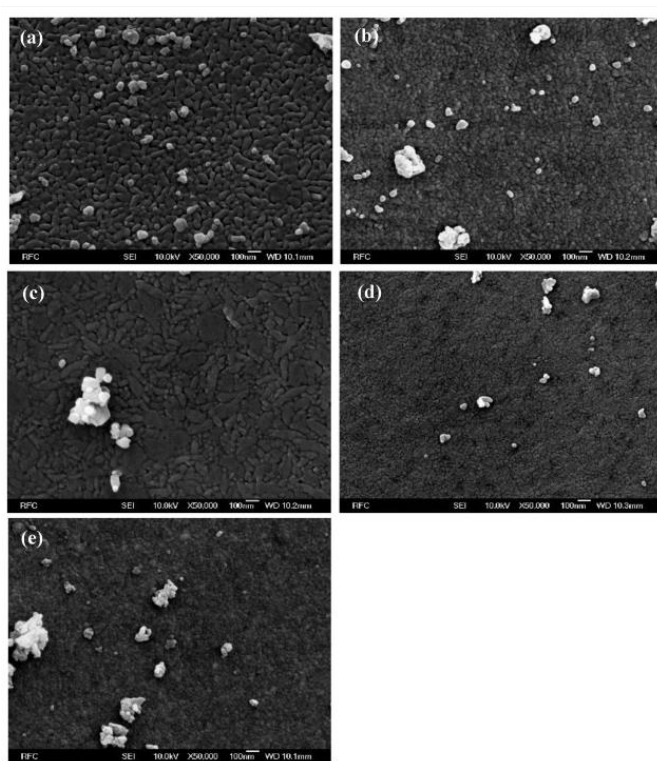


Figure 3.3 FE-SEM images of the W-NT-x materials: (a) $x = 0$, (b) $x = 3$, (c) $x = 5$, (d) $x = 7$, and (e) $x = 10$.

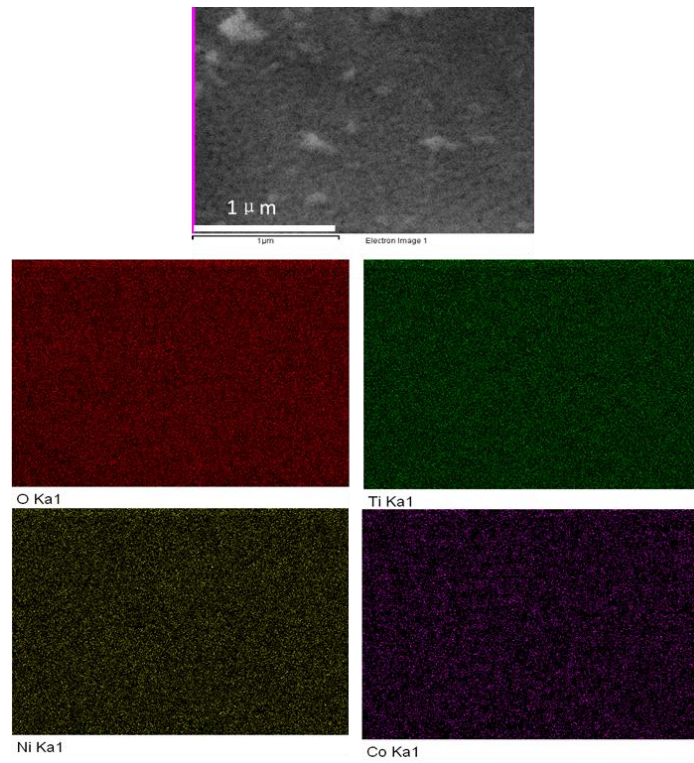


Figure 3.4 FE-SEM/EDS elemental mapping of Co-NT-7.

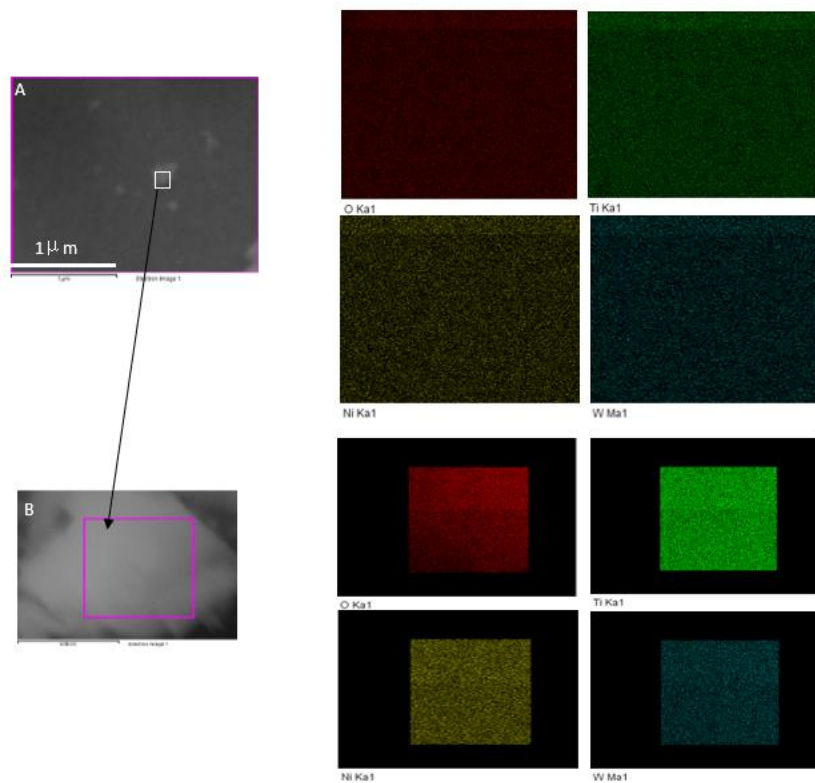


Figure 3.5 FE-SEM/EDS elemental mapping of (A) W-NT-7 and (B) marked area of W-NT-7.

Table 3.2 Relative nominal and actual compositions calculated from the EDS analysis of the Co-NT-x and W-NT-x materials.

Samples	Nominal content (wt.%)		Actual content (wt.%)	
	Co (or W)	NiTiO ₃	Co (or W)	NiTiO ₃
Co-NT-0 (W-NT-0)	0	100	0	100
Co-NT-3	3	97	2.29	97.71
Co-NT-5	5	95	2.33	97.67
Co-NT-7	7	93	4.06	95.94
Co-NT-10	10	90	4.55	95.45
W-NT-3	3	97	3.27	96.73
W-NT-5	5	95	0.6	99.4
W-NT-7	7	93	7.37(6.89*)	92.63(93.11*)
W-NT-10	10	90	12.6	87.4

* The values were calculated from the EDS elemental analysis for the marked area of W-NT- 7 in Figure 3.5.

The FTIR spectra of the materials are shown in Figure 3.6. The characteristic vibration bands corresponding to metal-oxygen bonds appear in the range of 400–700 cm⁻¹. The peaks at 457, 554, 640, and 722 cm⁻¹ correspond to the stretching modes of Ti-O-Ni bonds, Ni-O bonds, Ti-O bonds, and the bending of O-Ti-O bonds, respectively [7,18]. There was no shift of the band position in the FTIR spectra with increasing Co or W content. Instead, when high amounts of W were added to the materials (W-NT-7 and W-NT-10), additional bands were detected at 960 and 884 cm⁻¹, which correspond to the stretching vibrations of W-O-W in WO₄ or WO₆ units and the stretching vibrations of W-O⁻ and W=O bonds associated with WO₄ and WO₆ units, respectively (Figure 3.6 B(d) and (e)) [19]. The XRD patterns of the W-NT-x materials show no characteristic peaks related to WO_x crystallite phases, even at high W contents (Figure 3.1 B). Therefore, the appearance of new FTIR bands for the W-NT-7 and W-NT-10 materials demonstrates that WO_x phases were formed but highly dispersed on the surface of the materials. However, in the case of the Co-NT-x materials, Co doping induced no change in the FTIR spectra, implying that CoO_x phases are not formed, even at high Co contents.

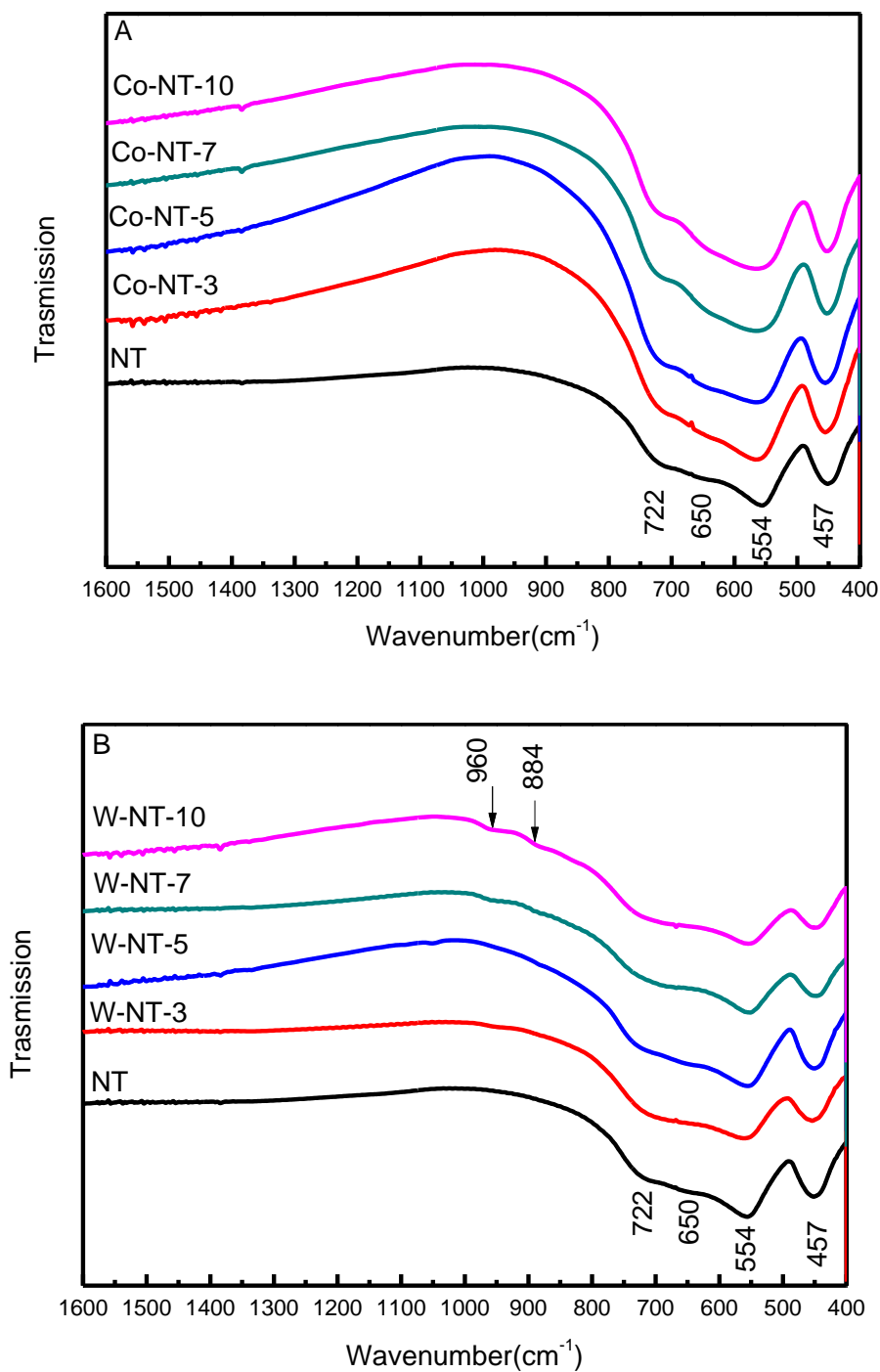


Figure 3.6 FTIR spectra of the (A) Co-NT-x and (B) W-NT-x materials

The Raman spectra of the materials were obtained to evaluate transition metal doping in the NiTiO_3 materials (Figure 3.7). Five A_g and five E_g Raman active modes were observed in the ilmenite structure, which confirmed the rhombohedral structure of NiTiO_3 [11]. The band positions were located at 183.3, 224.3, 237.8, 286.0, 340.0,

390.2, 457.7, 606.2, 701.6, and 772 cm^{-1} , which are in good agreement with results reported previously [7,11]. According to the calculation performed by Baraton et al. [20], the clear presence of ten Raman active fundamental modes indicates a good crystalline structure. The Raman signals showed a decreasing trend in the intensity with increasing Co doping content, implying that the added Co atoms influenced on the lattice bonding (Figure 3.7A). Moreover, it is interesting that there is a clear red shift in the band positions ranging from 200 to 500 cm^{-1} when Co was added. However, the W doping into the NiTiO_3 ilmenite structure did not result in a red shift of the bands positioned from 200 to 500 cm^{-1} , which is different from Co doping. However, the Raman band intensities decreased, which is the same behavior as observed for Co doping. Among the diverse Raman bands in the range, the positions of the A_g^2 and E_g^3 bands are plotted as a function of the transition metal dopant concentration (Co, or W) in Figure 3.8. Here, the different behaviors of the Raman band position shift for the Co and W dopants are clearly observed where red shifts are observed with the Co dopant and no shifts are observed for the W-NT-x materials. The Co substitution for Ti/Ni in the NiTiO_3 ilmenite lattice caused a red shift in the band positions in a previous study [11]. According to da Costa et al. [9], a clear red shift in the Raman spectra for $\text{Ni}_x\text{Pb}_{1-x}\text{TiO}_3$ materials resulted from the formation of a $\text{Ni}_x\text{Pb}_{1-x}\text{TiO}_3$ solid solution, indicating Pb^{2+} substitution for Ni^{2+} in the lattice. Baraton et al. [20] also reported the Raman band positions for ilmenite-type mixed oxides where the Raman bands for CoTiO_3 were located at lower frequencies than those for NiTiO_3 . However, in the case of Co-doped TiO_2 nanoparticles, the incorporation of the Co dopant into the TiO_2 lattice resulted in a blue shift of the E_{1g} mode in the Raman spectra, which was explained by oxygen vacancy formation in the Co-doped TiO_2 materials [21]. For the Co-doped TiO_2 materials, the Co dopants substituted only for Ti^{4+} ion sites in the lattice structure since there was no alternative cation site. Therefore, the red shift of the Raman bands by Co doping in this study proved that the Co^{2+} ions selectively substituted for Ni^{2+} ions in the NiTiO_3 ilmenite lattice structure, resulting in the formation of a solid solution of triple transition metal oxides.

In the Raman spectra of the W-NT-x materials (Figure 3.7B), there was little shift of the Raman bands in the range of 200–500 cm^{-1} . Instead, in the case of high W contents, additional Raman bands for WO_x phases appeared at 831 and 892 cm^{-1} , corresponding to the stretching vibrations of W-O-W in WO_4 or WO_6 units and vibrations of W-O⁻ or W=O in the tetrahedral or octahedral units, respectively [19]. This is similar to the

FTIR results obtained for the W-NT-x materials in this study, where no band position shift was observed and the appearance of additional bands for WO_x phases was obtained at high W contents. Accordingly, it was concluded that W doping at high contents (W-NT-7 and W-NT-10) allowed the formation of WO_x phases which were highly dispersed over the NiTiO_3 materials.

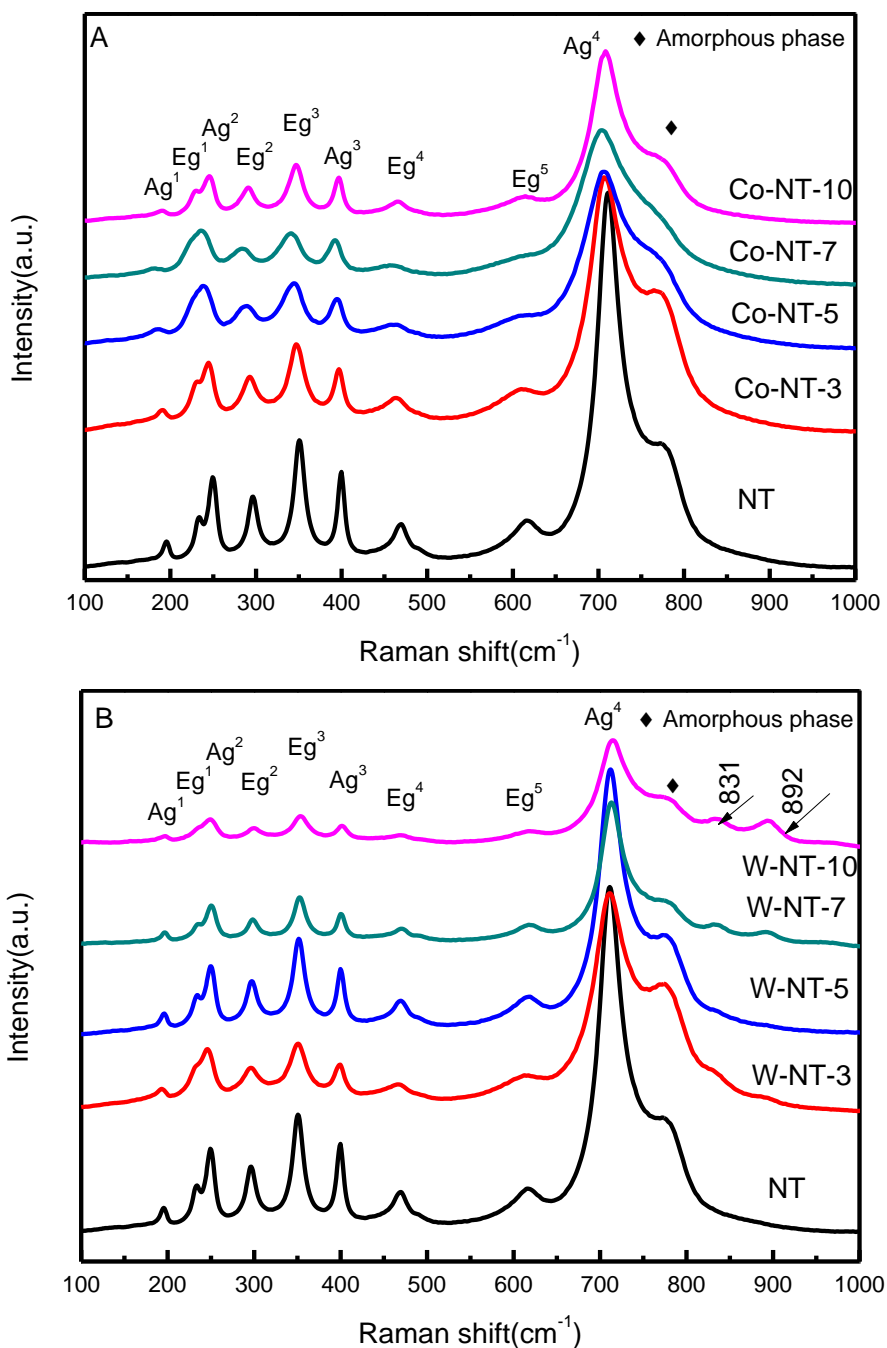


Figure 3.7 Raman spectra of the (A) Co-NT-x and (B) W-NT-x materials

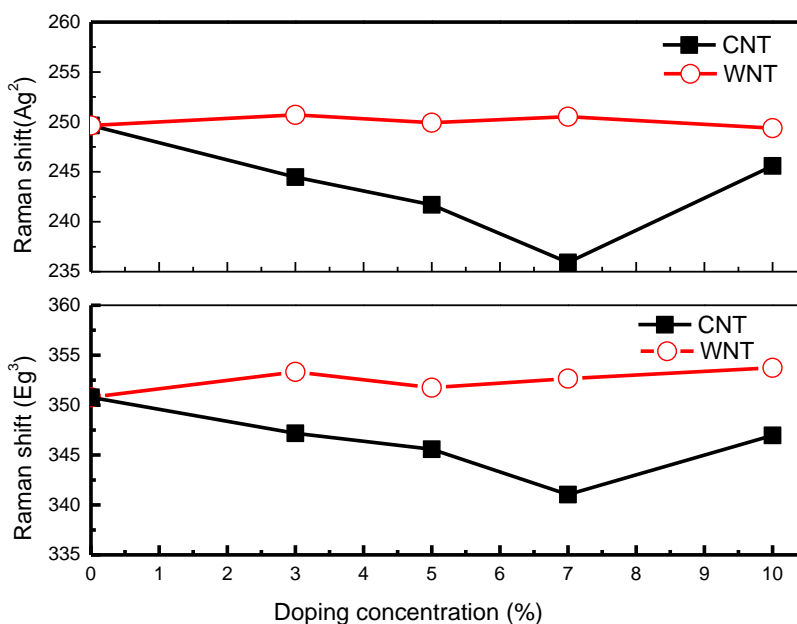
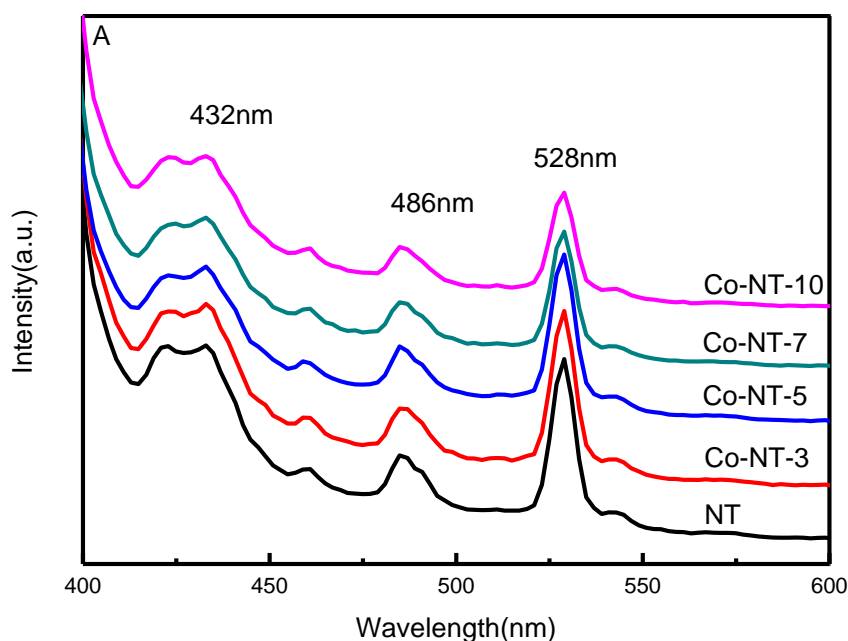


Figure 3.8 The positions of the Ag² and Eg³ Raman bands as a function of the Co or W content.

The textural properties of the prepared NiTiO₃ materials are presented in Table 1. Co doping into the NiTiO₃ ilmenite structure had no influence on the textural properties such as the surface area, pore volume, or average pore size. The values were similar regardless of the Co content in the materials, as shown in Table 1. This is in good agreement with other results obtained for the materials used in this study. Since Co is next to Ni on the periodic table and their sizes are similar [11], the doped Co²⁺ ions easily fit into Ni²⁺ sites in the NiTiO₃ ilmenite structure, forming a solid solution of triple transition metal oxides. However, for W-NT-x materials, the physicochemical properties were changed by W doping with an increase of the surface area and a decrease of the crystallite size, which is similar to the results of Mo-doped NiTiO₃ materials. In the case of Mo-doped NiTiO₃, the Mo doping induced a gradual increase of the surface area, which was explained to be due to a decrease of the grain sizes of Mo-doped NiTiO₃ materials [7]. In Ag-doped NiTiO₃ materials, the surface areas decreased with increasing Ag content, resulting from increased grain sizes. The Ag atoms did not fit into the ilmenite lattice and were mainly deposited on the surface [1]. Similarly, since W is a large transition metal dopant, W doping induced the formation of a WO_x phase with high W contents instead of W ion substitution in the ilmenite lattice structure.

The PL spectra of the Co-doped NiTiO₃ materials are shown in Figure 3.9A. Three strong emission peaks were observed at 432, 486, and 528 nm. There were no noticeable shifts of the emission peaks with increasing Co content. Instead, the intensities of all of the emission peaks gradually decreased along with increasing Co content, implying that Co doping into the NiTiO₃ ilmenite structure inhibited the recombination process of the materials. The PL emission spectra of the W-NT-x materials are shown in Figure 3.9B, where three strong PL emission peaks are also detected at the same positions without any peak shift along with the W content, representing that the relaxation process for the W-NT-x materials is the same as that for the Co-NT-x materials. In addition, the PL emission intensity behavior for the W-NT-x materials is consistent with that of the Co-NT-x materials, where a gradual decrease was obtained with increasing W concentration except for W-NT-5. The normalized intensities of the emission peak at 528 nm are additionally plotted as a function of the Co concentration in Figure 3.9C. The normalized emission intensities decreased with increasing concentration of the transition metal dopants.



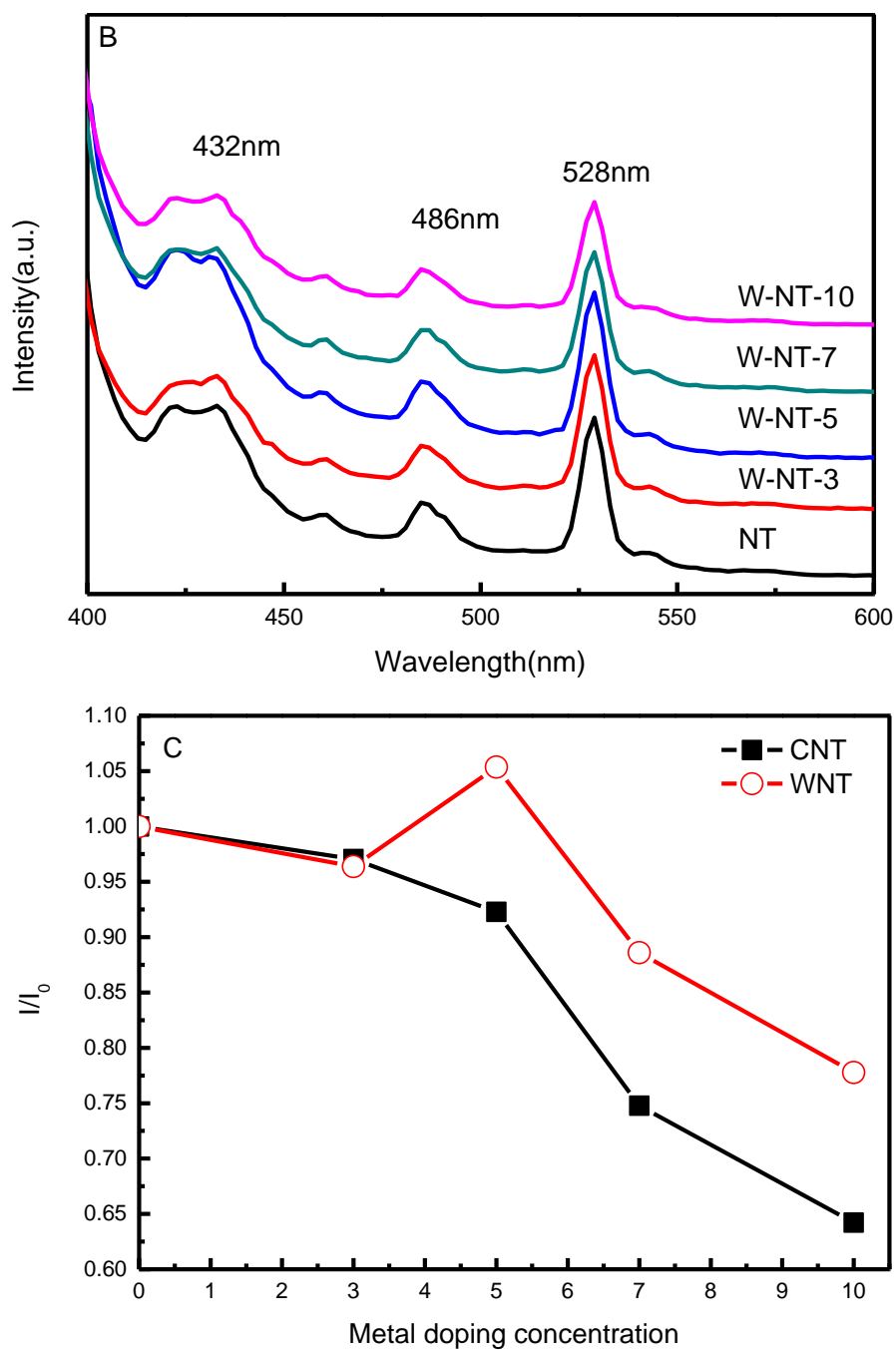


Figure 3.9 PL emission spectra ($\lambda_{ex} = 385$ nm) of the (A) Co-NT-x and (B) W-NT-x materials. (C) Variation of intensity ratios of visible emission peaks with Co and W concentration.

The UV–visible diffuse reflectance spectra of the materials are shown in Figure 3.10 and the bandgaps of the materials calculated from the UV–visible diffuse reflectance spectra are listed in Table 1. All of the materials are visible light responding materials since their bandgaps are in the range of 1.91–2.82 eV. However, no trends of

the UV–visible adsorption intensity and bandgap as a function of the Co or W concentrations in the materials were observed.

Figure 3.11 illustrates the modification of the NiTiO₃ ilmenite structure by the transition metal dopants. In this study, we employed Co and W as new transition metal dopants for NiTiO₃ ilmenite material, since Co and W are widely used as promoters for Ni or Ti-based catalysts [14-17]. However, Co is next to Ni in the periodic table and is expected to be similar to Ni, whereas W is a heavy transition metal and far away from Ni and Ti in the periodic table. Therefore, the sizes of the transition metal dopants are greatly different, which can result in different doping effects on the NiTiO₃ ilmenite structure. Based on the spectroscopic analysis, the Co²⁺ ions were doped into the NiTiO₃ ilmenite structure by the selective substitution for Ni²⁺ ion sites, resulting in a solid solution of triple transition metal oxides. The microstructural properties of the Co-doped NiTiO₃ materials including their grain sizes and surface areas remained nearly unchanged, even after Co doping. The changes of the microstructure and ilmenite lattice of the NiTiO₃ materials due to Co doping are illustrated in Figure 3.11. Meanwhile, W doping induced a change of the microstructure of the W-doped NiTiO₃ materials with a decrease of the grain size and an increase of the surface area. In addition, non-crystalline WO_x phases were partially formed at high W contents based on the FTIR, and Raman results.

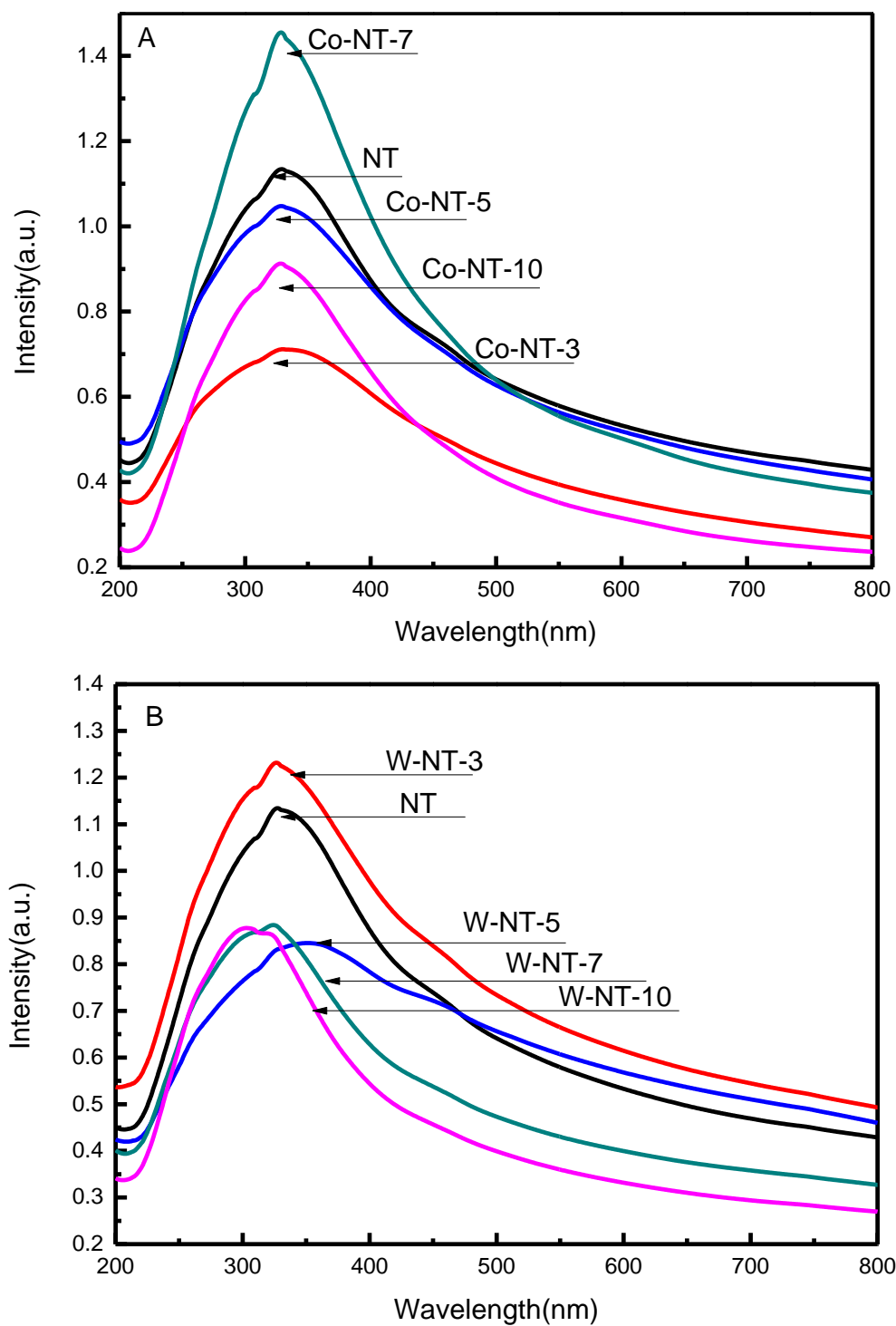


Figure 3.10 UV-Visible diffuse reflectance spectra of the (A) Co-NT-x and (B) W-NT-x materials:

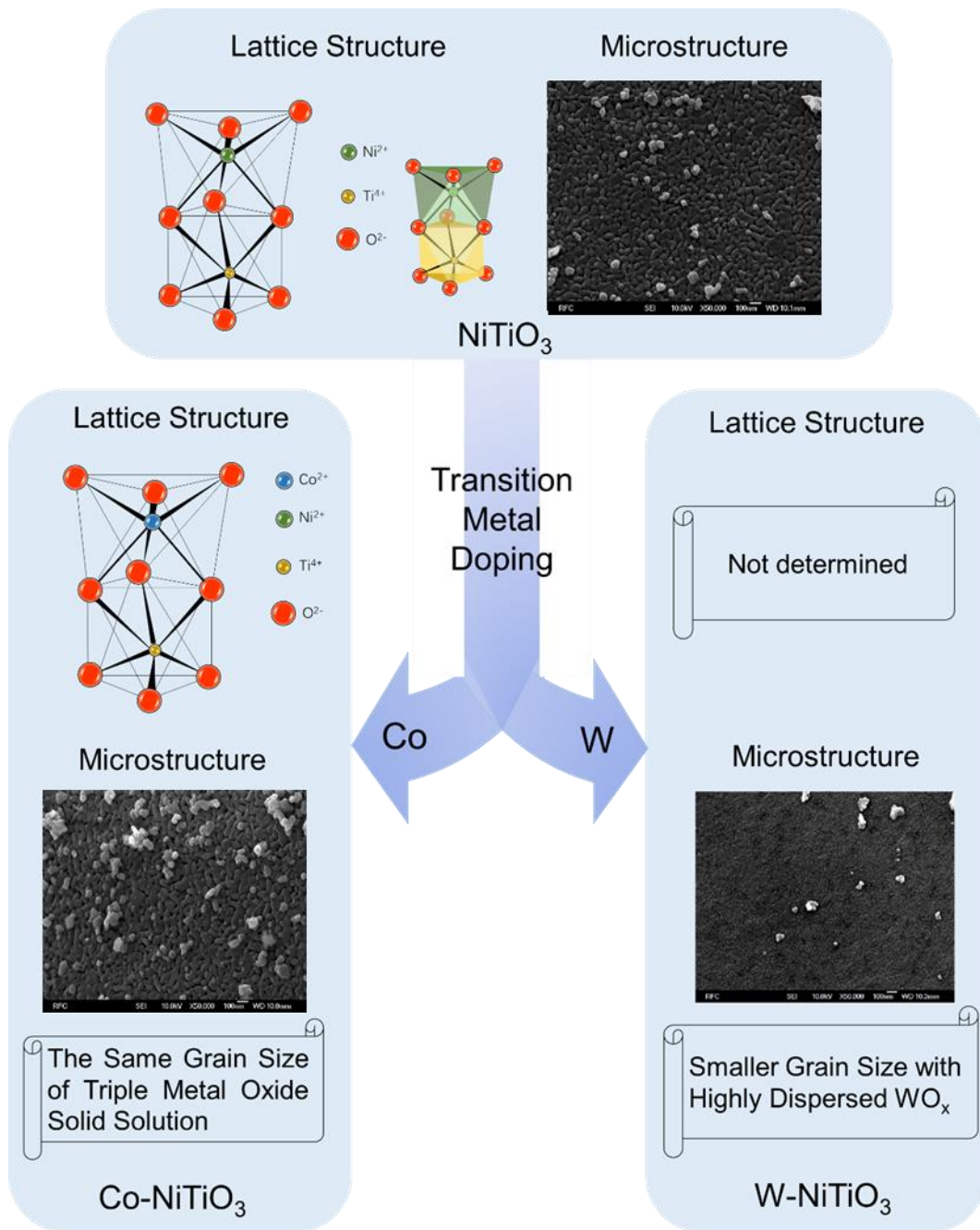


Figure 3.11 Schematic illustrations of the modification of the NiTiO_3 ilmenite structure by the transition metal dopants.

3.3.2 Photocatalytic behavior of the photocatalysts

To compare the performance of modified material with that of its raw components of NiTiO₃, the photocatalytic activity was investigated through the MB photodegradation, the result are shown in Figure 3.12. The MB photodegradation rates for W-NT-x photocatalysts were higher than that of pure NT, which indicated that W doping enhance the performance of photocatalytic activity of the NiTiO₃ photocatalyst. As for Co doped sample, whether in high-concentration or low-concentration doping, cobalt has a slight effect on activity. The quantitative evaluation of the photocatalytic activity need obtained the apparent photocatalytic rate constant k_a , which was calculated by the fitting curve of $\ln(C/C_0)$ vs. t . The results are provided in Table 3.3. Clearly, the highest k_a value was $3.69 \times 10^{-2} \text{ min}^{-1}$ for W-NT-3. Consequently, the W doping into the NiTiO₃ photocatalyst enhanced the photocatalytic activity during the MB photocatalytic degradation.

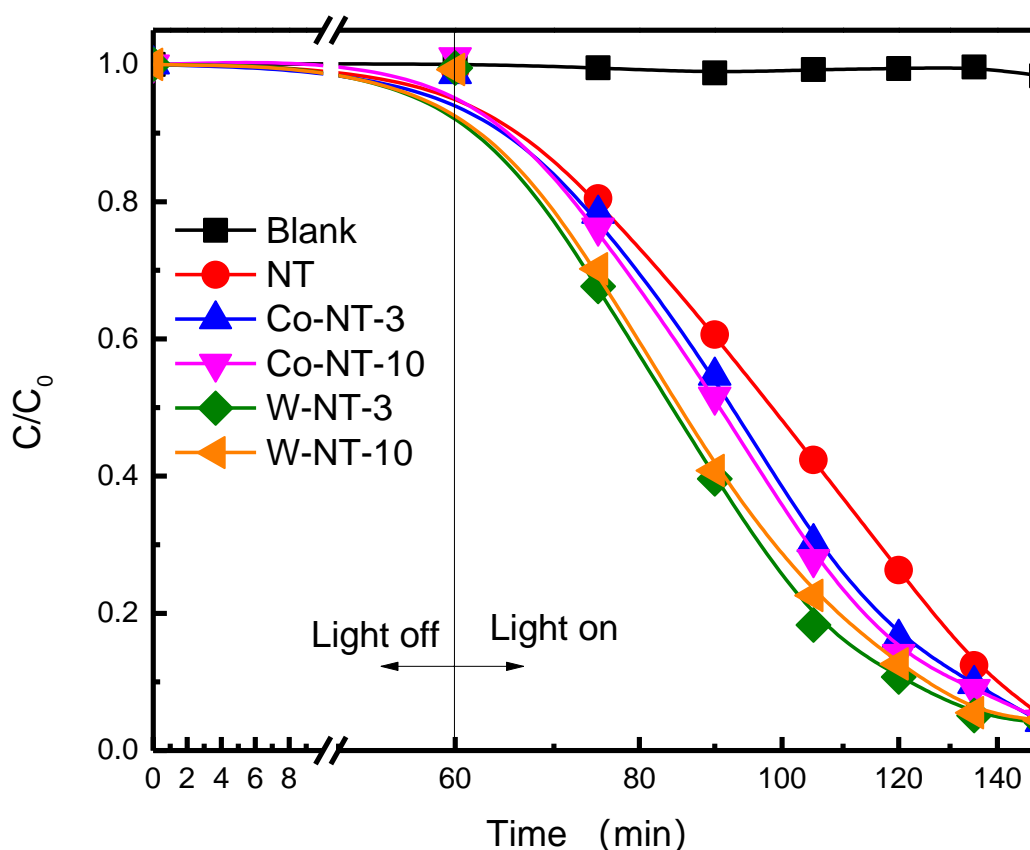


Figure 3.12 MB photocatalytic degradation of pure NiTiO₃, Co-NT-3, Co-NT-10, W-NT-3, W-NT-10.

Table 3.3 Photocatalytic reaction rate constants (k_{app}) of pure NiTiO₃, Co-NT-3, Co-NT-10, W-NT-3, W-NT-10.

Sample	$K_a (\times 10^{-2} \text{ min}^{-1})$
NT	2.76
Co-NT-3	3.15
Co-NT-10	3.22
W-NT-3	3.69
W-NT-10	3.52

3.4 Conclusion

In this study, Co-doped NiTiO₃ materials were prepared by a modified Pechini method and characterized by spectroscopic measurements. On the basis of the XRD, Raman, and FTIR analyses, it was found that for the Co-NT-x materials, the Co²⁺ ions were selectively doped into Ni²⁺ sites in the NiTiO₃ ilmenite lattice structure, forming a solid solution of triple transition metal oxides, Co_xNi_{1-x}TiO₃. The PL measurements revealed a gradual decrease of the PL emission intensity with increasing Co doping content, indicating that the recombination process was suppressed in the NiTiO₃ materials by the selective Co doping. Meanwhile, the W doping induced a change of the microstructure of the materials, resulting in the formation of highly dispersed WO_x phases at high W contents. W doping into the NiTiO₃ photocatalyst enhanced the photocatalytic activity.

References

- [1] Y.-J. Lin, Y.-H. Chang, G.-J. Chen, Y.-S. Chang, Y.-C. Chang, Effects of Ag-doped NiTiO₃ on photoreduction of methylene blue under UV and visible light irradiation, *J. Alloy. Compd.* 479 (2009) 785-790.
- [2] T.-D. Nguyen-Phan, C. Nguyen-Huy, C.-K. Kim, E.W. Shin, Facile microwave-assisted synthesis and controllable architecture of three-dimensional nickel titanate, *CrystEngComm* 17 (2015) 4562-4574.
- [3] B. Inceesungvorn, T. Teeranunpong, J. Nunkaew, S. Suntalelat, D. Tantraviwat, Novel NiTiO₃/Ag₃VO₄ composite with enhanced photocatalytic performance under visible light, *Catal. Commun.* 54 (2014) 35-38.
- [4] H. Wang, X. Yuan, H. Wang, X. Chen, Z. Wu, L. Jiang, W. Xiong, Y. Zhang, G. Zeng, One-step calcination method for synthesis of mesoporous g-C₃N₄/NiTiO₃ hetero structure photocatalyst with improved visible light photoactivity, *RSC Adv.* 5 (2015) 9 5643-95648.
- [5] T.-T. Pham, C. Nguyen-Huy, E.W. Shin, NiTiO₃/reduced graphene oxide materials synthesized by a two-step microwave-assisted method, *Mater. Lett.* 184 (2016) 38-42.
- [6] T.-T. Pham, C. Nguyen-Huy, E.W. Shin, Facile one-pot synthesis of nickel-incorporated titaniumdioxide/graphene oxide composites: Enhancement of photodegradation under visible- irradiation, *Appl. Surf. Sci.* 377 (2016) 301-310.
- [7] T.-T. Pham, S. G. Kang, E.W. Shin, Optical and structural properties of Mo-doped NiTiO₃ materials synthesized via modified Pechini methods, *Appl. Surf. Sci.* 411 (2017) 18-26.
- [8] N. Lenin, A. Karthik, M. Sridharpanday, M. Selvam, S.R. Srither, S. Arunmetha, P. Paramasivam, V. Rajendran, Electrical and magnetic behavior of iron doped nickel titanate (Fe³⁺/NiTiO₃) magnetic nanoparticles, *J. Magn. Mater.* 397 (2016) 281-286.
- [9] R.C. da Costa, A.D. Rodrigues, P.S. Pizani, Phase mixture, solid solution or composite: Raman scattering analyses of Ni_xPb_{1-x}TiO₃ and (NiTiO₃)_x + (PbTiO₃)_{1-x}, *J. Alloy. Compd.* 697 (2017) 68-71.

- [10] R. C. da Costa,^{1,2} T. A. de Toledo,¹ J. W. M. Espinosa,³ and P. S. Pizani, Atomic substitution effects on the structural and vibrational properties of $\text{Ni}_x\text{Pb}_{1-x}\text{TiO}_3$: X-ray diffraction and Raman scattering investigations, *AIP Adv.* 5 (2015) 077113-1-7.
- [11] Y. Fujioka, J. Frantti, A. Puretzky, G. King, Raman Study of the Structural Distortion in the $\text{Ni}_{1-x}\text{Co}_x\text{TiO}_3$ Solid Solution, *Inorg. Chem.* 55 (2016) 9436-9444.
- [12] J.B. Bellan, M.A. Ruiz-Preciado, M. Edely, J. Szade, A. Jouanneaux A.H. Kassiba, Visible-light photocatalytic activity of nitrogen-doped NiTiO_3 thin film prepared by co-sputtering process, *RSC Advances*, 5 (2015) 10551-10559.
- [13] R. Vijayalakshmi, V. Rajendran, Effect of Co-doping on structural and optical properties of NiTiO_3 nanoparticles, *Nanoscience and Nanotechnology: An International Journal*, 19 (2011) 1-5.
- [14] H. Zhu, D.C. Rosenfeld, M. Harb, D.H. Anjum, M.N. Hedhili, S. Ould-Chikh, Ni-M-O (M = Sn, Ti, W) Catalysts Prepared by a Dry Mixing Method for Oxidative Dehydrogenation of Ethane, *ACS Catal*, 6 (2016) 2852-2866.
- [15] H. Zhu, H. Dong, P. Laveille, Y. Saih, V. Caps, J.-M. Basset, Metal oxides modified NiO catalysts for oxidative dehydrogenation of ethane to ethylene, *Catal. Today* 228 (2014) 58-64.
- [16] S.N.R. Inturi, T. Boningari, M. Suidan, P.G. Smirniotis, Visible-light-induced photodegradation of gas phase acetonitrile using aerosol-made transition metal (V, Cr, Fe, Co, Mn, Mo, Ni, Cu, Y, Ce and Zr) doped TiO_2 , *Appl. Catal. B: Environmental* 144 (2014) 333-342.
- [17] B.S. Kwak, N.-K.Park, S.O. Ryu, J.-I. Baek, H.-J. Ryu, M. Kang, Improved reversible redox cycles on MTiO_x (M = Fe, Co, Ni, and Cu) particles afforded by rapid and stable oxygen carrier capacity for use in chemical looping combustion of methane, *Chem. Eng. J.* 309 (2017) 617-627.
- [18] S. Yuvaraj, V. D. Nithya, K. S. Fathima, Investigations on the temperature dependent electrical and magnetic properties of NiTiO_3 by molten salt synthesis, *Mater. Res. Bulletin* 48(3) (2013) 1110-1116.
- [19] G. Lakshminarayana, K.M. Kaky, S.O. Baki, S. Ye, A. Lira, I.V. Kityk, M.A. Mahdi, Concentration dependent structural, thermal, and optical features of Pr^{3+} -doped multicomponent tellurite glasses, *J. Alloy. Compd.* 686 (2016) 769-784.

[20] M. I. Baraton, G. Busca, M. C. Prieto, G. Ricchiardi, V. Sanchez Escribano, On the vibrational spectra and structure of FeCrO_3 and of the ilmenite-type compounds CoTiO_3 and NiTiO_3 , *J. Solid State Chem.* 112(1) (1994) 9-14.

[21] B. Anitha, M. Abdul Khadar, A. Banerjee, Paramagnetic behavior of Co doped TiO_2 nanocrystals controlled by self-purification mechanism, *J. Sol-Gel Sci. Technol.* 239 (2016) 237-245.

4 Modification of NiTiO₃ visible light-driven photocatalysts by Nb doping and NbO_x heterojunction

4.1 Introduction

Owing to global energy crisis and environmental pollution, many efforts have been made to develop an alternative way for energy production and pollution control [1-3]. Recently, photochemical processes using visible light-driven photocatalysts have attracted considerable attention owing to their potential applications in environmental remediation and solar energy harvesting systems [4-5]. In general, single metal oxides (e.g., TiO₂, ZnO, and Fe₂O₃) have been widely used as photocatalysts where electrons can be excited by UV light irradiation [6-8]. However, because the necessity to use photocatalysts under visible light irradiation has increased, many researchers have paid great attention to multimetal oxide materials, which can be employed as visible light-driven photocatalysts.

Nickel titanate (NiTiO₃) is a double-metal semiconductor with an ilmenite structure; it is known as a potential visible light-driven photocatalyst owing to its modest cost, nontoxicity for humans, high stability under light illumination, and great durability in an oxidizing environment [9-10]. NiTiO₃ has a narrow band gap of ca. 2.18 eV where electrons in the valence band can be excited to conduction band under visible light irradiation. However, its photocatalytic utilization has been limited by poor quantum efficiency caused by the fast recombination rate of photogenerated electron–hole pairs.

Among many ways to modify the properties of NiTiO₃ materials, the addition of metals or metal oxides into the NiTiO₃ ilmenite structure has been widely used to enhance the comprehensive photocatalytic performance of the catalysts [11-21]. Ag [12], [13], Mo [14], Fe [15], and W [16] have been employed as metal doping components in the NiTiO₃ lattice structure. The metals doped into the NiTiO₃ lattice served as an electron trap to inhibit the recombination process, which resulted in an increase in the photocatalytic activity [12-14]. Metal doping into the NiTiO₃ lattice allowed to replace metals and generated an oxygen vacancy in the lattice structure. Niobium has not been employed as a doping metal component in the NiTiO₃ structure, even though Nb has been doped into other inorganic metal oxide structures to improve their structural and

catalytic properties [22-24]. Nb doping influenced the crystalline properties of SnO₂ [22]. Doping of a small amount of Nb into WO₃/ZrO₂ catalysts increased the catalyst stability [23]. Meanwhile, NiTiO₃ heterojunctions using metal oxides have been introduced as another promising and potential way to reinforce the photocatalytic performance of NiTiO₃ materials. The formation of heterojunction semiconductors has been proven to be an effective way to expand the photoabsorption range and facilitate the separation of photoinduced charges [19-21]. Nb oxide is an n-type transition metal oxide semiconductor that is widely used in many fields. Nb oxide has been also applied to photocatalysis to remove environmental pollutants [20-21]. Nb₂O₅/TiO₂ heterojunction photocatalyst showed good photocatalytic performance owing to the high separation efficiency of photogenerated electron–hole pairs [19]. In addition, the photocatalytic activity of Nb₂O₅-containing heterojunctions (e.g., Nb₂O₅/SrNb₂O₆, N-doped Nb₂O₅/reduced graphene oxide, and Nb₂O₅/Ag₃PO₄) were examined through various photocatalytic reactions [25-27]. However, there has been no report on Nb₂O₅/NiTiO₃ heterojunction photocatalysts.

In this study, we prepared two types of Nb-containing NiTiO₃ photocatalysts via the simple modification methods of Nb doping and NbO_x heterojunction. The photocatalytic activity of Nb-containing NiTiO₃ photocatalysts was examined by the photodegradation of methylene blue under simulated solar irradiation. Their physicochemical and optical properties were thoroughly investigated by the N₂ adsorption/desorption technique, Fourier transform infrared (FT-IR) spectroscopy, Raman spectroscopy, X-ray diffraction (XRD), UV–visible spectroscopy, and X-ray photoelectron spectroscopy (XPS). The photocatalytic performance of two types of Nb-containing NiTiO₃ photocatalysts was compared and discussed in detail on the basis of the properties analyzed by diverse characterization tools.

4.2 Experimental

4.2.1 Materials preparation

Nickel nitrate hexahydrate (Ni(NO₃)₂·6H₂O, Cas No.:13478-00-7,99.999%), Nb chloride (NbCl₅, Cas No.: 10026-12-7, 99.9%), and titanium n-butoxide [Ti(OC₄H₉)₄, Cas No.: 546-68-9, 97%] were purchased from Sigma-Aldrich Korea (Gyeonggi, South Korea). Anhydrous ethyl alcohol (C₂H₅OH, Cas No.:64-17-5, 99.9%) and hy-

drochloric acid (HCl, Cas No.: 7647-01-0, 35–37%) were purchased from Samchun Pure Chemical Company Ltd. (PyeongTaek, South Korea). Citric acid monohydrate ($C_6H_8O_7 \cdot H_2O$, Cas No.: 5949-29-1, 99.5%) was obtained from OCI Company Ltd (Seoul, South Korea). All chemical reagents were used as received without further purification.

In this work, pure and Nb-doped $NiTiO_3$ materials were synthesized via the modified Pechini method according to our previous report [14]. A total of 0.75 g of citric acid and 100 ml of ethyl alcohol were mixed and stirred for 15 min. Subsequently, $NbCl_5$ was dissolved in this solution to form a clear solution; this method was used only for Nb-doped $NiTiO_3$ materials. Then, $Ni(NO_3)_2 \cdot 6H_2O$ and $Ti(OC_4H_9)_4$ were added to the mixture. The solution was very thoroughly stirred to ensure that the mixture was uniform and stable. After stirring for 60 min, the resultant mixture was transferred to a Teflon-lined stainless-steel autoclave, sealed, and heated at 160 °C for 6 h (ramping rate = 2 °C/min). Upon the solvothermal treatment, the precipitate was collected via centrifugation and washed several times with C_2H_5OH . Finally, the materials were dried in air overnight, ground, and calcined at 600 °C for 5 h (ramping rate = 2 °C/min). The prepared materials were designated as NT-Nb-x, where x represents the mass ratio of Nb to Ti.

$NbOX/NiTiO_3$ heterojunction materials were synthesized by the hydrolysis loading method. Pure $NiTiO_3$ was dispersed in 30 ml of a 0.5 M hydrochloric acid solution. The mixture was sonicated for 30 min to fully disperse solid particles. Then, a defined quantity of $NbCl_5$ was added to the mixture under stirring. The homogeneously mixed solution was heated at 100 °C, and the powders were dried at 80 °C for 24 h. Finally, the materials were dried in air overnight, ground, and calcined at 600 °C for 5 h (ramping rate = 2 °C/min). The prepared materials were denoted as NT-NbOx-y, where y represents the mass ratio of Nb to Ti. For comparison, pure NbOX was also prepared using the same process without $NiTiO_3$.

4.2.2 Characterization

The catalyst structure was analyzed by a Rigaku D/MAZX 2500V/PC high-power X-ray diffractometer (Tokyo, Japan) with a $Cu K\alpha$ X-ray source with the wavelength of 1.5415 Å and the scanning rate of 2° (2 θ)/min. The FT-IR spectra of the materials were recorded on a Nicolet 380 spectrometer (Thermo Fisher Scientific, Waltham, MA,

USA). Raman analysis was carried out on a DXR Raman microscope (Thermo Fisher Scientific, Waltham, MA, USA) under 533 nm laser excitation. UV–visible absorption spectroscopy (UV-Vis-DRS) was performed using a SPECORD 210 Plus spectroscope (Analytik Jena, Jena, Germany). The Brunauer–Emmett–Teller (BET) surface area of the catalysts was determined by nitrogen adsorption/desorption on an ASAP 2020 apparatus (Micromeritics, Norcross, GA, USA). Field-emission scanning electron microscopy (FE-SEM, JSM-600F, JEOL, Tokyo, Japan) was used to evaluate morphologies. The chemical state of components was determined by an XPS (Thermo Fisher Scientific Co., Waltham, MA, USA) instrument equipped with an aluminum $K\alpha$ X-ray source. All XPS data were corrected with C 1s peak (284.6 eV). XPS data of Ti 2p, Nb 3d and O 1s were deconvoluted using the XPSPEAK version 4.1. Zeta potential of photocatalysts were measured at room temperature using a zeta potential analyzer (Zetasizer Nano ZS, Malvern Panalytical, Malvern, United Kingdom). Five milligrams of photocatalyst powder were dispersed into 100 ml of aqueous solution, and then the solution was sonicated for 30 min. The zeta potential of each sample suspension was measured three times at a specific pH value. The isoelectric point (IEP) of each sample was obtained from the plot of zeta potential vs. pH. The pH of the sample suspension was adjusted from 2 to 9 by adding 0.5 M HCl or NaOH solution. The IEP value was defined as the pH value where a zeta potential of the sample was zero.

Photoluminescence (PL) spectra were recorded on a Cary Eclipse fluorescence spectrophotometer (Agilent Technologies, Australia), and the sample was illuminated with a 375 nm laser as an excitation source at ambient temperature. Electrochemical impedance spectroscopy (EIS) was conducted on an impedance analyzer (VSP, Bio-Logic Science Instruments, Seyssinet-Pariset, France) over the frequency range from 100 kHz to 0.01 Hz, at an amplitude of 10 mV, and at a DC potential of + 0.5 VSCE after a 10-min delay. Samples were prepared by dispersing 20 mg of catalyst and 2 g of activated carbon into a mixture of 100 μ L isopropanol 99.7% (Sigma-Aldrich Korea, Gyeonggi, South Korea) and 30 μ L of Nafion 5 wt% (Sigma-Aldrich Korea, Gyeonggi, South Korea). Ten milliliters of 1 M sodium hydroxide (NaOH) solution were used as the electrolyte for the three-electrode system. A 6-mm standard-type glassy carbon electrode onto which 10 μ L of the sample was dropped was used as the working electrode, a RE-1BP (Ag/AgCl) electrode was used as the reference electrode, and

platinum wire was used as the counter electrode. The electrodes and SVC-3 voltammetry cell were purchased from ALS Co., Ltd. (Tokyo, Japan).

4.2.3 Photocatalysis and analyses

The photocatalytic activity of the prepared materials was measured via the photocatalytic degradation of methylene blue (MB, Sigma-Aldrich Korea, Gyeonggi, South Korea) and methyl orange (MO, Sigma-Aldrich Korea, Gyeonggi, South Korea) aqueous solutions. Furthermore, 10 mg of as-prepared water-dispersible catalysts were immersed in a 50 ml MB (or MO) solution that was continuously stirred by a magnetic bar in the dark for 60 min. After achieving equilibrium adsorption, the solution was irradiated for 180 min using an Oriel's Sol1A™ Class ABB system with a 140 W xenon lamp and UV cut-off/correction filter. For each analysis, 1 ml of MB (or MO) solution was collected by syringe from the beaker and filtered by a polytetrafluoroethylene membrane filter (Whatman GmbH, Dassel, Germany). The MB (or MO) concentrations in the liquid samples were analyzed by absorbance at $\lambda_{\text{max}} = 664$ nm (or $\lambda_{\text{max}} = 465$ nm) as a function of irradiated time (using a SPECORD 210 Plus spectroscope).

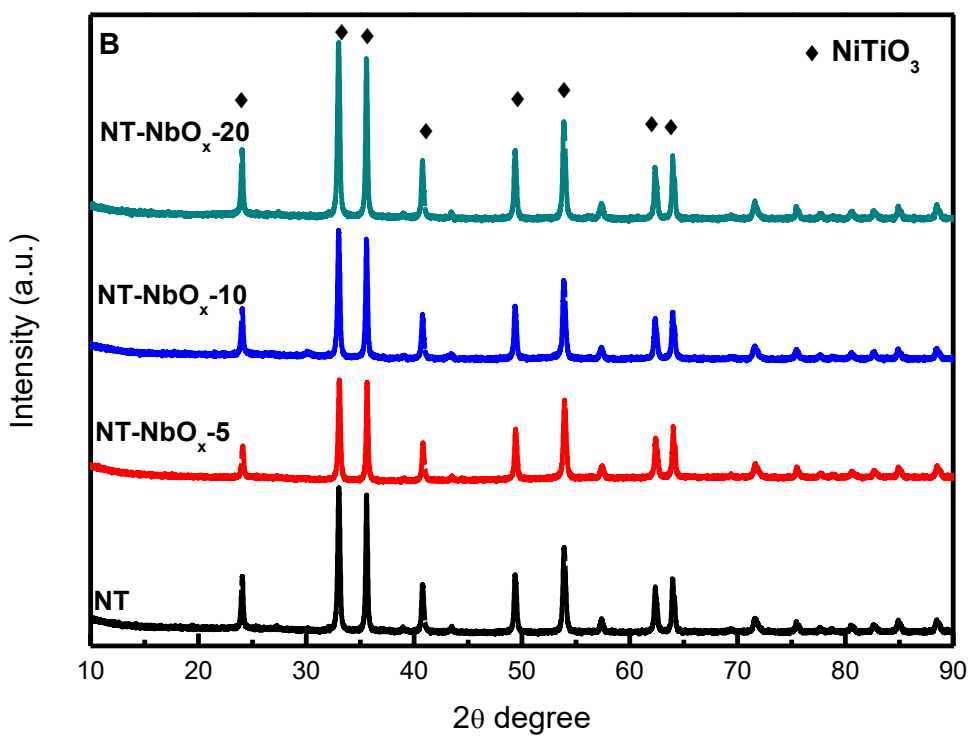
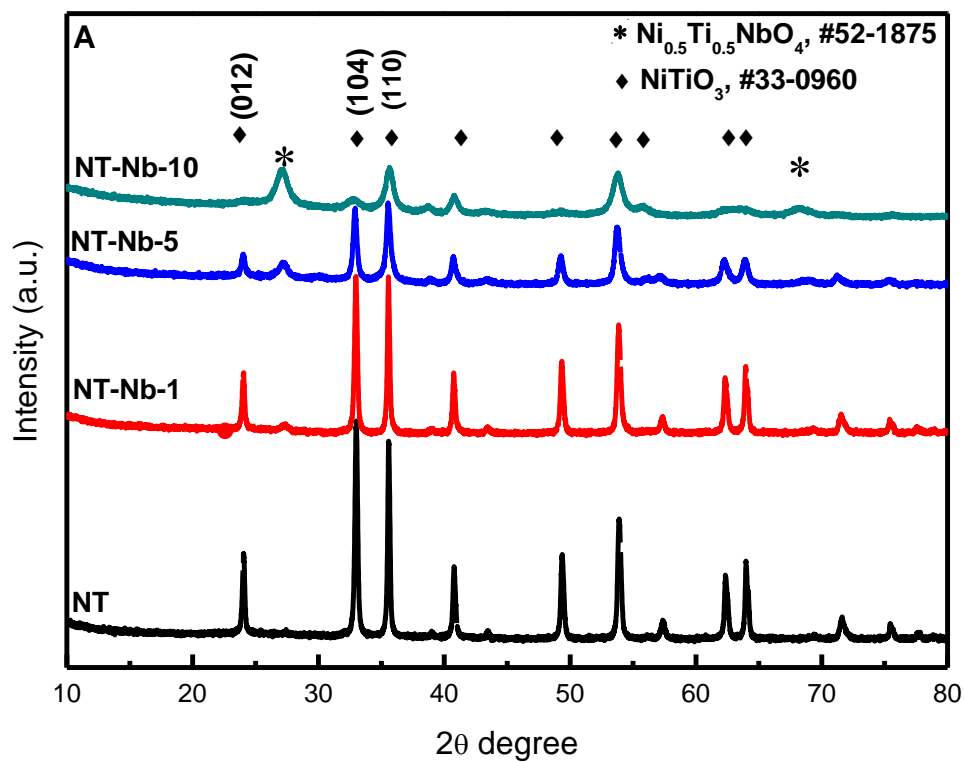
Radical trapping experiments were additionally conducted with different radical scavengers: EDTA-Na₂ for h^+ , isopropyl alcohol (IPA) for $\bullet\text{OH}$, p-benzoquinone (BQ) for $\text{O}_2\bullet^-$, and AgNO_3 for e^- . In the MB photodegradation, 1 mM of each radical scavenger was added into the MB solution before starting the test [28-29].

4.3 Results and discussion

4.3.1 Structural properties of photocatalysts

The crystal structures of pure and Nb-containing NiTiO_3 photocatalysts were investigated by the XRD measurement. As shown in Figure 4.1, the XRD patterns confirm the presence of pure ilmenite NiTiO_3 with an R3 space group (JCPDS No. 33-0960). The diffraction peak positions at $2\theta = 24.05$, 33.01 , 35.58 , and 53.90° are attributed to (012), (104), (110), and (116) planes of the ilmenite phase, respectively [30]. The XRD peak intensities for Nb-doped photocatalysts (NT-Nb-x) decrease according to the Nb content, and a new XRD peak appears at $2\theta = 27.04^\circ$ for NT-Nb-5 and NT-Nb-10

(Figure 4.1 A), which illustrates a phase transformation with a decrease in NiTiO₃ ilmenite crystallinity [31]. Specifically, the new peak at $2\theta = 27.04^\circ$ considerably increases at the highest Nb content, which clearly indicates the transformation of NiTiO₃ ilmenite structure into a new phase. This peak is assigned as the (110) plane of rutile Ni_{0.5}Ti_{0.5}NbO₄ (JCPDS No. 52-1875) with a space group P42/mnm [32], [33], [34]. However, the peak intensities for NT-NbO_x-y photocatalysts remain unchanged along with an increase in the NbO_x, which implies the retention of the ilmenite structure (Figure 4.1 B). Additional diffraction peaks corresponding to Nb species are not observed in the XRD patterns of the NT-NbO_x-y samples, which implies the high dispersion of Nb species or existence in an amorphous phase. Interestingly, a shift in the characteristic XRD peaks for the NiTiO₃ phase is clearly observed in Nb-doped NiTiO₃ photocatalysts, as shown in Figure 4.1C. This shift in the diffraction peaks to lower 2θ angles is indicative of the expansion of the lattice of the NiTiO₃ crystal structure owing to the Nb doping into NT-Nb-x. Lattice expansion by Nb doping can generate more oxygen vacancies and more free space in the lattice structure [35]. In this study, the generation of oxygen vacancy by Nb doping is evidenced by the XPS data of O 1 s, which will be shown later. The crystallite sizes (L) of these samples were estimated using the Scherrer equation, and the results are listed in Table 1. The crystallite sizes calculated for NT-Nb-x decrease with an increase in the Nb doping content from 92.6 nm for NT to 34.6 nm for NT-Nb-10, which is consistent with the results of Mo-doped NiTiO₃ [14]. Here, doped Nb is substituted for Ni or Ti ion sites in the NiTiO₃ lattice structure, which results in the generation of oxygen-vacant sites in the lattice and in a decrease in the crystallite size. The tetragonality factor (c/a in Table 1) was also calculated, as cited in literature [36]. The c/a value for NT-Nb-10 clearly decreases to 2.74, which illustrates the transformation of NiTiO₃ into the triple metal oxide solid solution at high Nb doping.



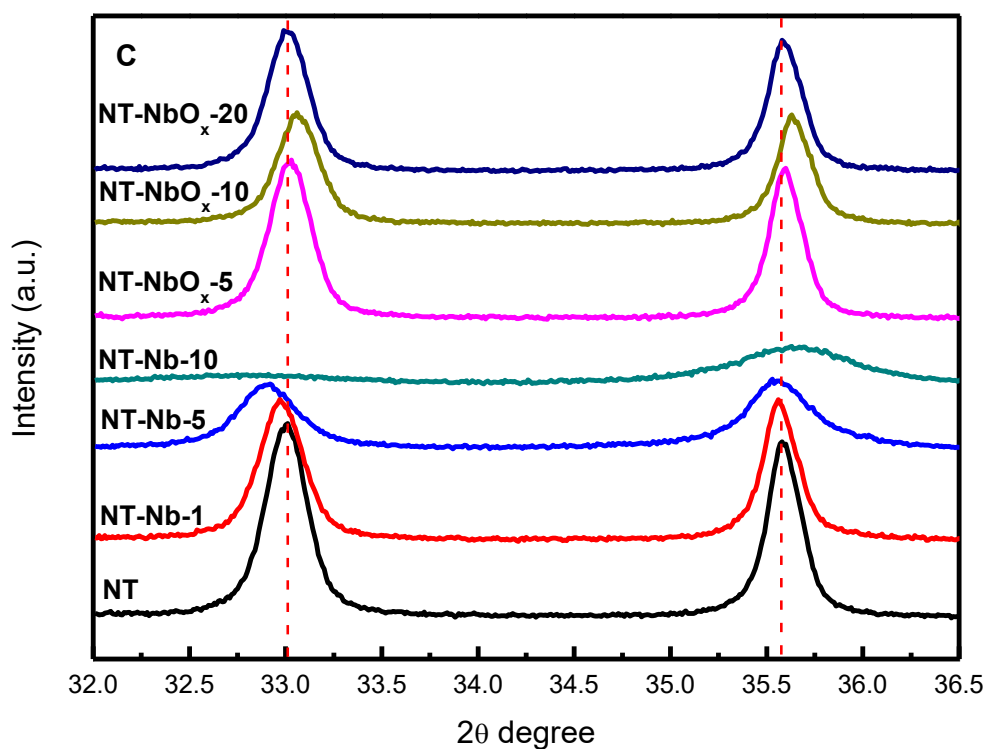


Figure 4.1 XRD patterns of Nb-doped NiTiO₃ (A), and NbO_x/NiTiO₃ heterojunction (B), and the magnified view of Nb-doped NiTiO₃ and Nb₂O₅/NiTiO₃ (C).

Table 4.1 Physicochemical properties of the prepared photocatalysts

Samples	L ^a (nm)	c/a ^b	S _{BET} ^c (m ² /g)	O _{Ads} /O _{La} ratio ^d	Ni/Ti ^e
NT	92.6	2.80	11.76	0.39	0.95
NT-Nb-1	87.0	2.79	12.73	0.73	0.71
NT-Nb-5	66.7	2.78	34.72	2.21	0.65
NT-Nb-10	34.6	2.74	32.91	4.19	0.46
NT-NbO _x -5	91.5	2.79	12.09	n.m.	n.a.
NT-NbO _x -10	93.9	2.79	18.59	0.65	0.96
NT-NbO _x -20	93.8	2.79	12.66	n.m.	n.a.

^a Average crystalline sizes were obtained from the (104) diffraction of the ilmenite phase *via* the Scherrer equation.

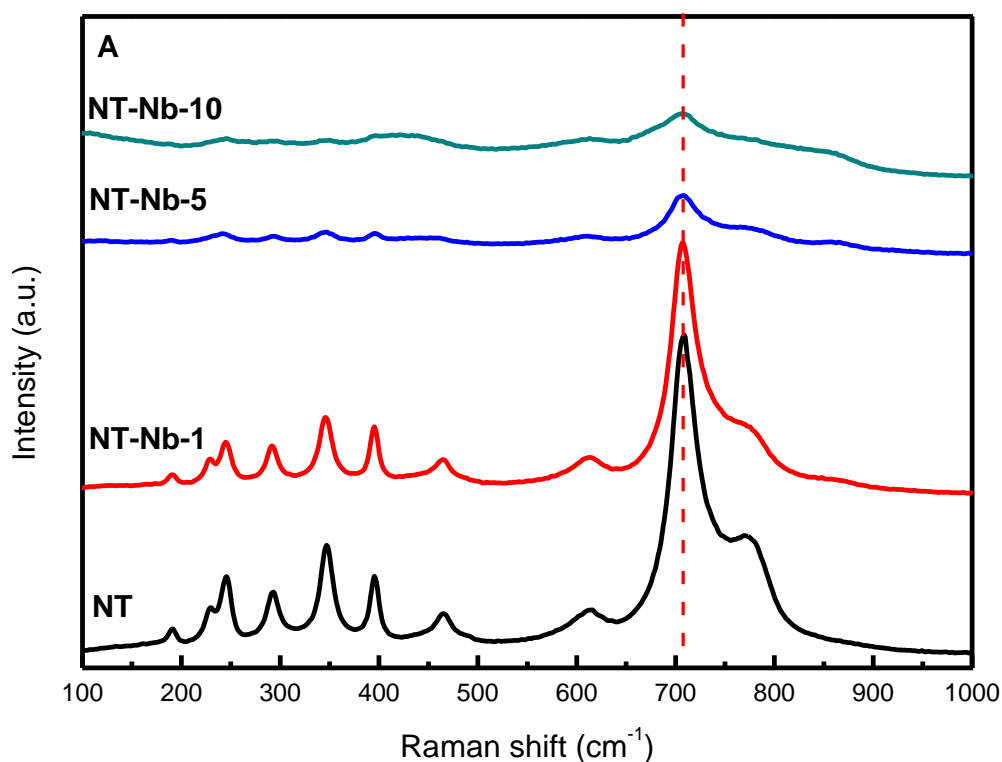
^b The values were calculated from the XRD patterns.

^c Specific surface areas were calculated from the fit of the Brunauer–Emmett–Teller (BET) equation for N₂ adsorption–desorption isotherms.

^d The values were acquired from the XPS data for O 1s.

^e The values were obtained from the XPS data for Ni 2p and Ti 2p. The Ni/Ti ratios reflect the surface compositions.

Nine peaks for ten characteristic Raman modes for rhombohedral NiTiO₃ were observed in Figure 4.2 A. Four A_{1g} and five E_g Raman active modes confirm the symmetric R $\bar{3}$ structure [37-38]. For Nb-doped NiTiO₃ photocatalysts, Raman signals sharply decrease with an increase in the Nb doping content, and there is no shift in the Raman peak position. A similar trend was observed in the Ni_xPb_{1-x}TiO₃ solid solution system. With a change in the x-values in the Ni_xPb_{1-x}TiO₃ lattice structure, the peak intensity at 710 cm⁻¹ reduced, which implied the formation of the Ni_xPb_{1-x}TiO₃ solid solution [36]. Similarly, a rapid decrease in the Raman peak intensity for Nb-doped NiTiO₃ photocatalysts is due to the formation of a triple metal oxide solid solution, Ni_{0.5}Ti_{0.5}NbTiO₄, by Nb doping. However, Figure 4.2 B shows the Raman spectra of NT-NbO_x-y samples. There was no shift in peak positions and no change in the peak intensity in the Raman spectra of the NbO_x/ NiTiO₃ heterojunction, which implies the high dispersion of NbO_x over NiTiO₃. This is in good agreement with the XRD results.



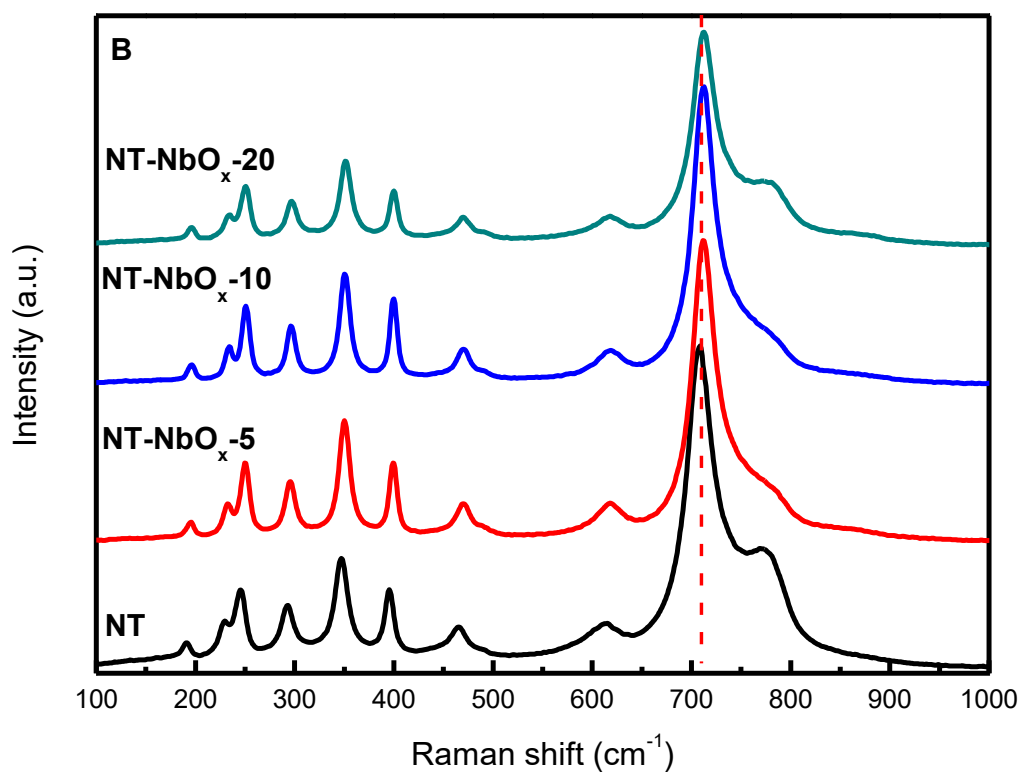


Figure 4.2 Raman spectra of Nb-doped NiTiO₃ (A) and NbO_x/NiTiO₃ heterojunction (B).

The FT-IR spectra of photocatalysts were additionally collected (Figure 4.3). The bands at 645, 555, and 455 cm⁻¹ correspond to the vibrational modes of Ti-O, Ni-O, and Ni-O-Ti bonds, respectively [14]. Whereas there is no change in the FT-IR spectra for NbO_x/NiTiO₃ heterojunction photocatalysts; for Nb-doped NiTiO₃ photocatalysts, the characteristic bands at 430–750 cm⁻¹ are overlapped, which results in a broad band when 10% Nb is loaded into the photocatalyst. In previous studies related to the doping of Mo, Co, and W into the NiTiO₃ phase, the FT-IR characteristic bands for metal oxide were not changed by metal doping, even though Mo or Co was doped into the NiTiO₃ lattice structure [14, 16]. A change in the FT-IR pattern for NT-Nb-10 indirectly indicates the formation of triple metal oxide phase by the Nb doping.

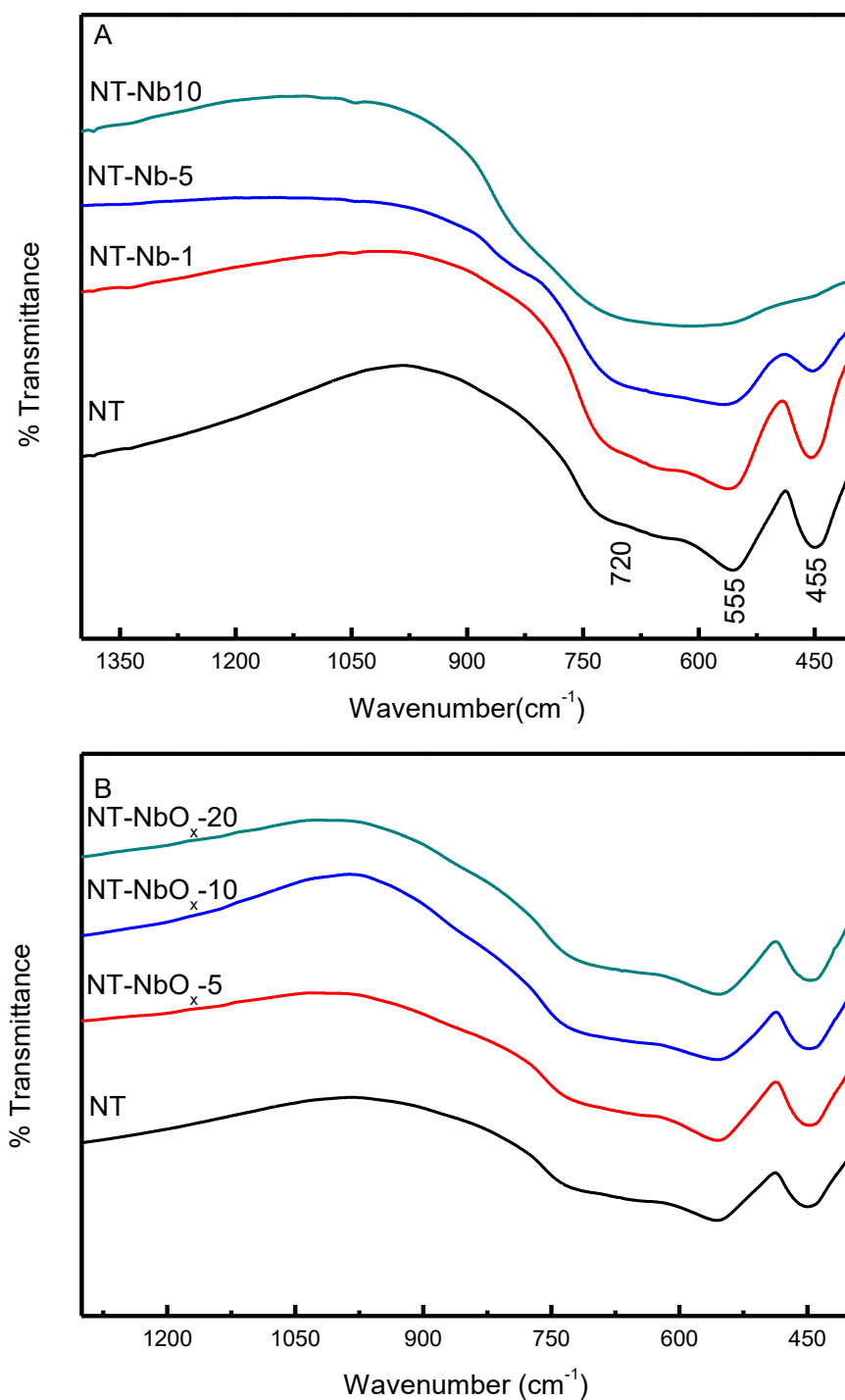


Figure 4.3 FT-IR spectra of Nb-doped NiTiO₃ (A) and NbO_x/NiTiO₃ heterojunction (B).

Figure 4.4 shows the FE-SEM images of pure and Nb-doped NiTiO₃ photocatalysts. All Nb-doped NiTiO₃ materials have the same morphology of nanoparticle aggregates, which exhibits a typical shape of NiTiO₃. In Figure 4.4, the grain sizes of nanocrystal aggregates decrease when Nb species is doped into the NiTiO₃ lattice structure, which is in good agreement with the previously reported results [14, 16]. However, in Figure

4.5, the grain size does not change even after the addition of NbO_x species, which is also consistent with the XRD results in this study. The BET surface areas for all photocatalysts are listed in Table 1. NT-Nb-5 and NT-Nb-10 have much high surface areas at 32.9 m²/g and 34.7 m²/g, respectively, whereas the surface areas of other photocatalysts are in the range of 11.7–18.5 m²/g, which is caused by the breakage of nanoparticles and the formation of triple metal oxide solid solution by doping Nb species into the NiTiO₃ lattice structure.

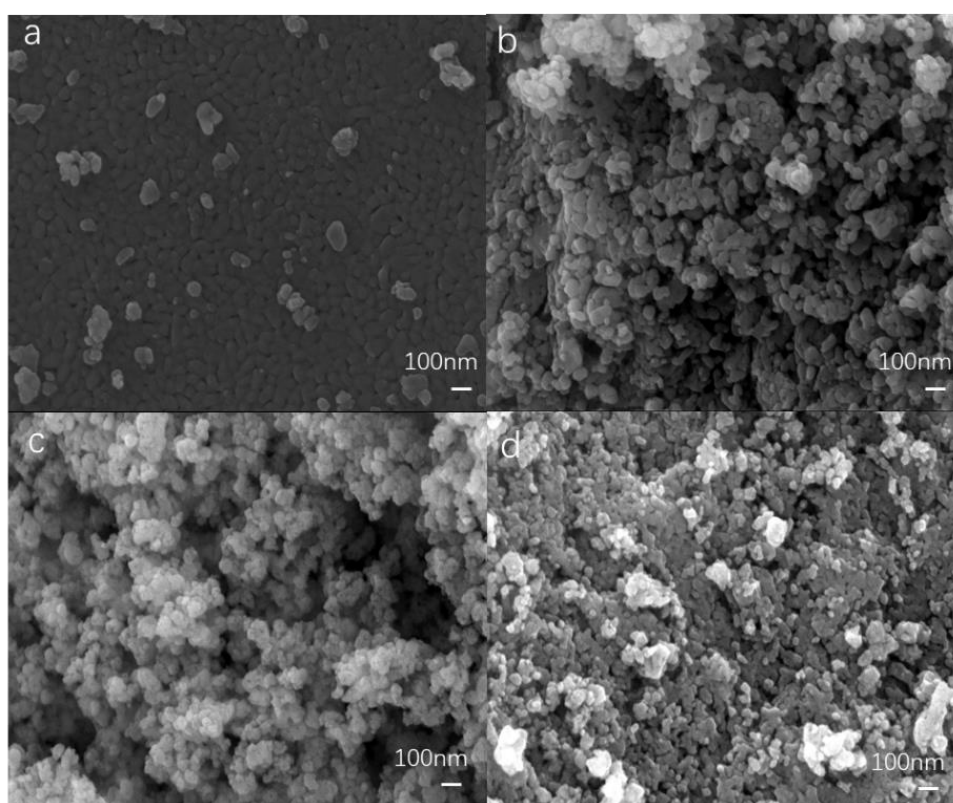


Figure 4.4 FE-SEM images of NT (a), NT-Nb-1 (b), NT-Nb-5 (c), and NT-Nb-10 (d).

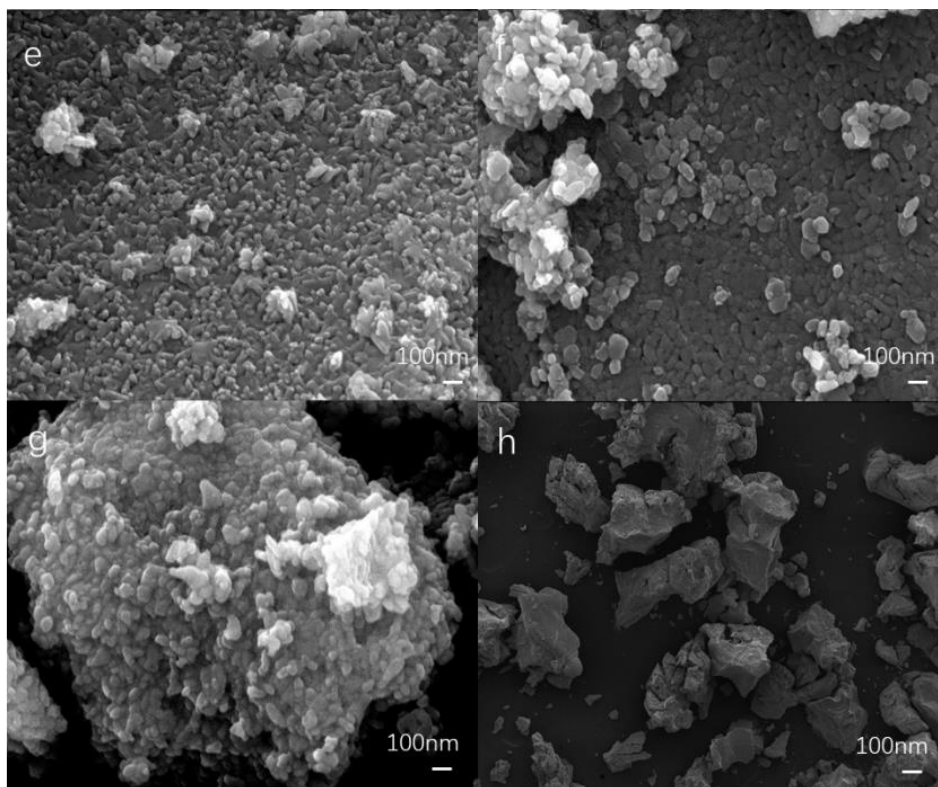


Figure 4.5 FE-SEM images of NT-NbOx-5 (a), NT-NbOx-10 (b), NT-NbOx-20 (c), and NbOx (d).

4.3.2 Electronic properties of photocatalysts

The XPS data of Ni 2p and Ti 2p for Nb-doped NiTiO₃ photocatalysts are shown in Figure 4.6. The XPS data of Ni 2p and Ti 2p for NT-NbOX-10 and NbO_x are also plotted for comparison. In Figure 4.6A, the peaks at 854.6 eV and 872.3 eV correspond to Ni 2p_{3/2} and Ni 2p_{1/2}, respectively. The spin-energy separation of 17.7 eV in the binding energies of Ni 2p is due to the Ni²⁺ species in NiTiO₃ [39]. The Ti 2p XPS data exhibit two main peaks at 463.1 eV and 457.3 eV, which correspond to the Ti 2p_{1/2} and Ti 2p_{3/2} binding energies, respectively (Figure 4.6B). The spin-energy separation in the binding energies of Ti 2p is 5.8 eV, which is a feature of the Ti⁴⁺ species [31], [40]. Overall, the pattern change in Ti 2p XPS along with the Nb doping content is similar to that in Ni 2p XPS. We tracked the change in electronic states of Ni 2p and Ti 2p by Nb doping via the peak deconvolution of Ti 2p XPS data.

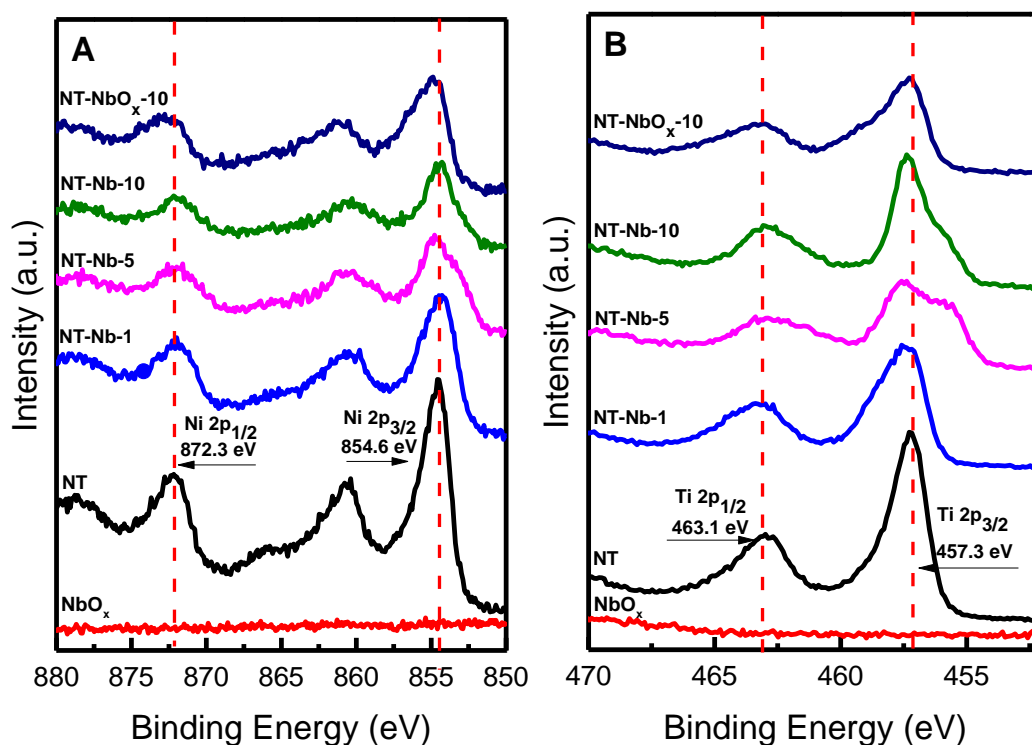


Figure 4.6 XPS data of Ni 2p (A), and Ti 2p (B) for NbO_x , pristine NiTiO_3 , NT-Nb-1, NT-Nb-5, NT-Nb-10, and NT-NbO_x-10

Figure 4.7A shows two deconvoluted peaks of the Ti 2p XPS data for Ti^{4+} (blue lines) and Ti^{3+} (green lines). For NT, NT-Nb-1, and NT-NbO_x-10, one dominant peak for Ti^{4+} is observed, which indicates that Ti^{3+} is negligible in these photocatalysts. In contrast, NT-Nb-5 and NT-Nb-10 exhibit a strong shoulder peak of Ti^{3+} with a main peak of Ti^{4+} , which implies that Nb doping into the NiTiO_3 lattice structure partially reduces the oxidation state of Ti from Ti^{4+} to Ti^{3+} . This phenomenon is also supported by the XPS data of Nb 3d. In Figure 4.7B, the XPS peaks of Nb 3d are deconvoluted into two peaks: Nb^{5+} at 206.2 eV and Nb^{3+} at 204.7 eV. Herein, for NbO_x , NT-Nb-1, and NT-NbO_x-10, only the Nb^{5+} oxidation state is detected, whereas another Nb^{3+} oxidation state is additionally observed for NT-Nb-5 and NT-Nb-10, which clearly demonstrates that the high Nb doping amount in NiTiO_3 photocatalysts results in the additional Nb^{3+} oxidation state with the main state of Nb^{5+} . Therefore, for the high Nb content (NT-Nb-5 and NT-Nb-10), less oxidized metal states (e.g., Ti^{3+} and Nb^{3+}) are formed by Nb doping, which implies the formation of neighboring oxygen vacancies in the NiTiO_3 lattice structure [41-42]. In the literature, an oxygen deficient surface was caused by the formation of Ti^{3+} [43]. The detection of Ti^{3+} was normally accom-

panied by the formation of oxygen vacancy. However, the XPS data for Ti 2p and Nb 3d for NT-NbO_x-10 are similar to those for NT and NbO_x, which indicates that the chemical states of Ti and Nb are barely modified by the heterojunction in this study.

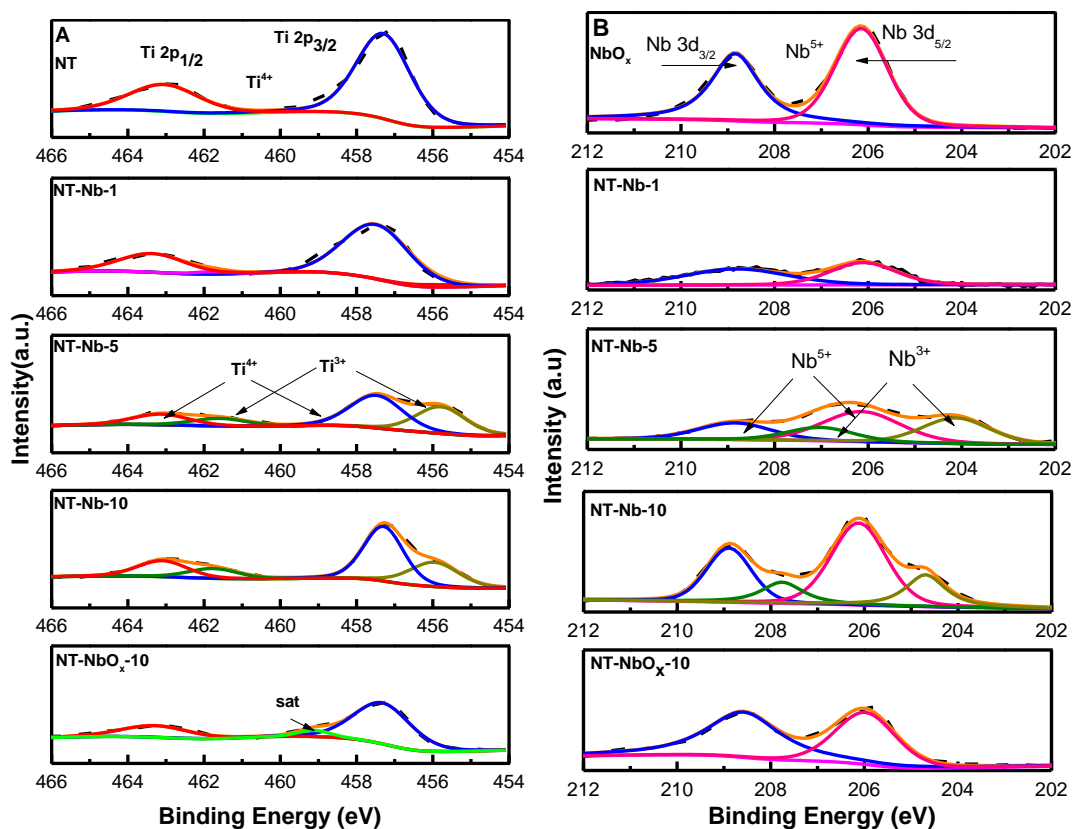


Figure 4.7 Deconvoluted XPS data of Ti 2p (A) and Nb 3d (B) for pristine and modified NiTiO₃ materials. Black dashed line is the experimental data and yellow/blue/red/green lines are the fitted data.

Figure 4.8 shows the XPS of O1s for NT, NT-Nb-x, and NT-NbO_x-10, which provides the information on the origin and the number of oxygen vacancies. Two major peaks at the binding energies of 529.0 eV and 530.5 eV are generally assigned to the characteristic lattice oxygen (O_{La}) and surface chemisorbed oxygen (O_{Ads}) species, respectively [44-47]. A new lattice oxygen phase related to oxygen vacancy is observed for NT-Nb-x photocatalysts because Nb doping generate Ti³⁺ and Nb³⁺ oxidation states in Nb-doped NiTiO₃ photocatalysts. Unfortunately, the binding energy of the new oxygen phase related to oxygen vacancy overlaps with that of O_{Ads}. However, previous studies indicated that the concentration of oxygen vacancies was proportional to the relative peak intensity of surface-adsorbed oxygen to lattice oxygen [44-48]. Clearly, an increase in the peak intensity of O_{Ads} in Figure 4.8 indicates the increasing number

of oxygen vacancies on the surface of NT-Nb-5 and NT-Nb-10. The calculated values of the peak intensity ratio ($O_{\text{Ads}}/O_{\text{La}}$) are listed in Table 1. The $O_{\text{Abs}}/O_{\text{La}}$ ratios for NT-Nb-x gradually increase from pure NT to NT-Nb-10. This implies that the doped Nb species are gradually substituted for metal cation sites in the NiTiO_3 lattice structure, which results in the generation of an oxygen vacancy in the structure. Furthermore, the $O_{\text{Abs}}/O_{\text{La}}$ ratios for NT-Nb-5 (2.21) and NT-Nb-10 (4.19) are significantly higher than those for NT, NT-NbO_x-10, and NT-Nb-1 (0.39–0.73), which indicates a significant increase in the oxygen vacancy in NT-Nb-5 and NT-Nb-10. This is consistent with the appearance of Ti^{3+} and Nb^{3+} in Nb-doped NiTiO_3 photocatalysts. A considerable increase in the oxygen vacancy and the appearance of less oxidized Ti^{3+} and Nb^{3+} in Nb-doped NiTiO_3 photocatalysts is strongly correlated with the formation of a triple metal oxide solid solution in NT-Nb-5 and NT-Nb-10.

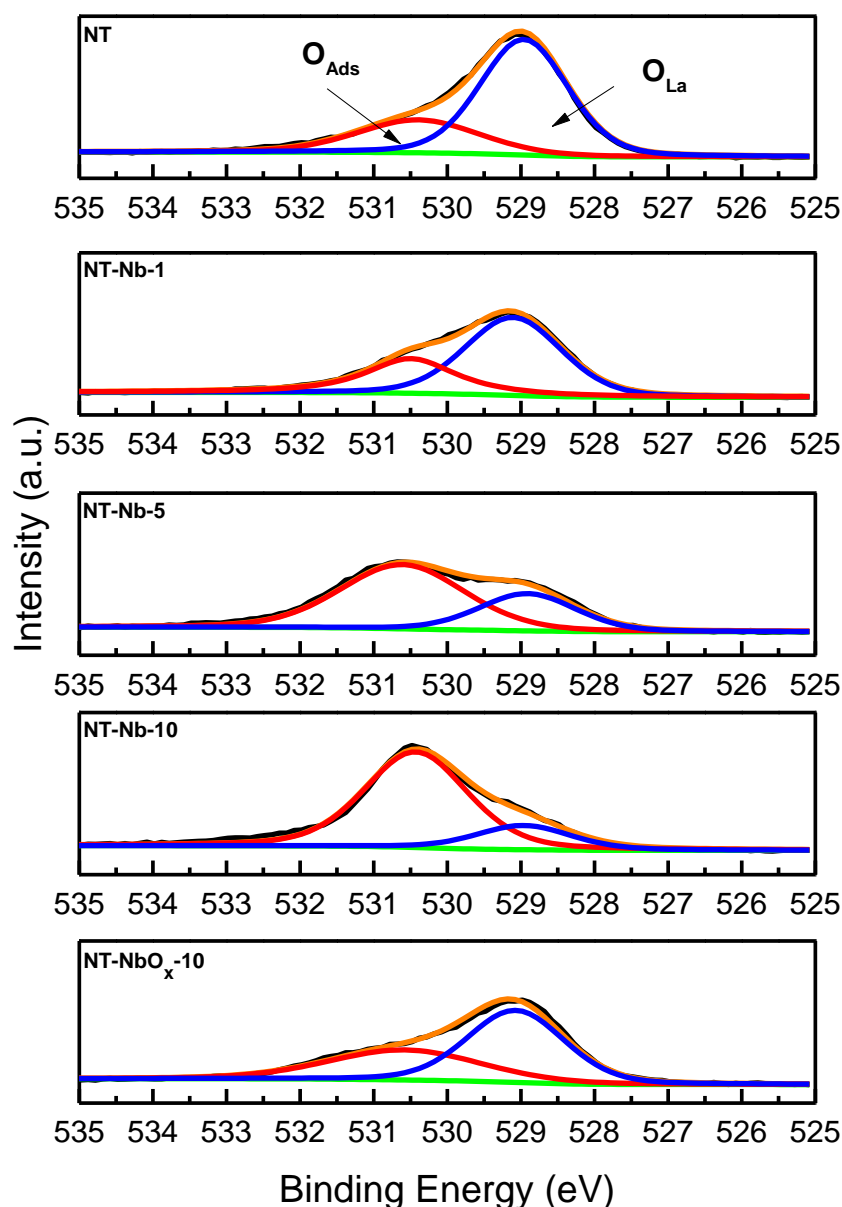


Figure 4.8 XPS data of O 1s for pristine NiTiO₃, NT-Nb-1, NT-Nb-5, NT-Nb-10, and NT-NbO_x-10. Black dashed line is the experimental data, and yellow/blue/red lines are the fitted data.

Figure 4.9 shows the generation of an oxygen vacancy and a change in the Ti oxidation state in the NiTiO₃ lattice structure by Nb doping. According to the surface chemical composition of Nb-doped NiTiO₃ photocatalysts, Ni/Ti ratios decrease with an increase in the Nb, which indicates that the doped Nb species is mainly substituted for Ni²⁺ sites in the NiTiO₃ lattice structure (Table 1). The replacement of Nb⁵⁺ (or Nb³⁺) cations in Ni²⁺ sites generates oxygen-vacant sites in the lattice structure owing to charge unbalance, which decreases the Ti oxidation state from Ti⁴⁺ to Ti³⁺. However,

at high Nb doping condition ($x \geq 5$), the further generation of oxygen vacancy in the NiTiO_3 lattice structure induces the transformation to the triple metal oxide solid solution (e.g., $\text{Ni}_{0.5}\text{Ti}_{0.5}\text{NbO}_4$ phase).

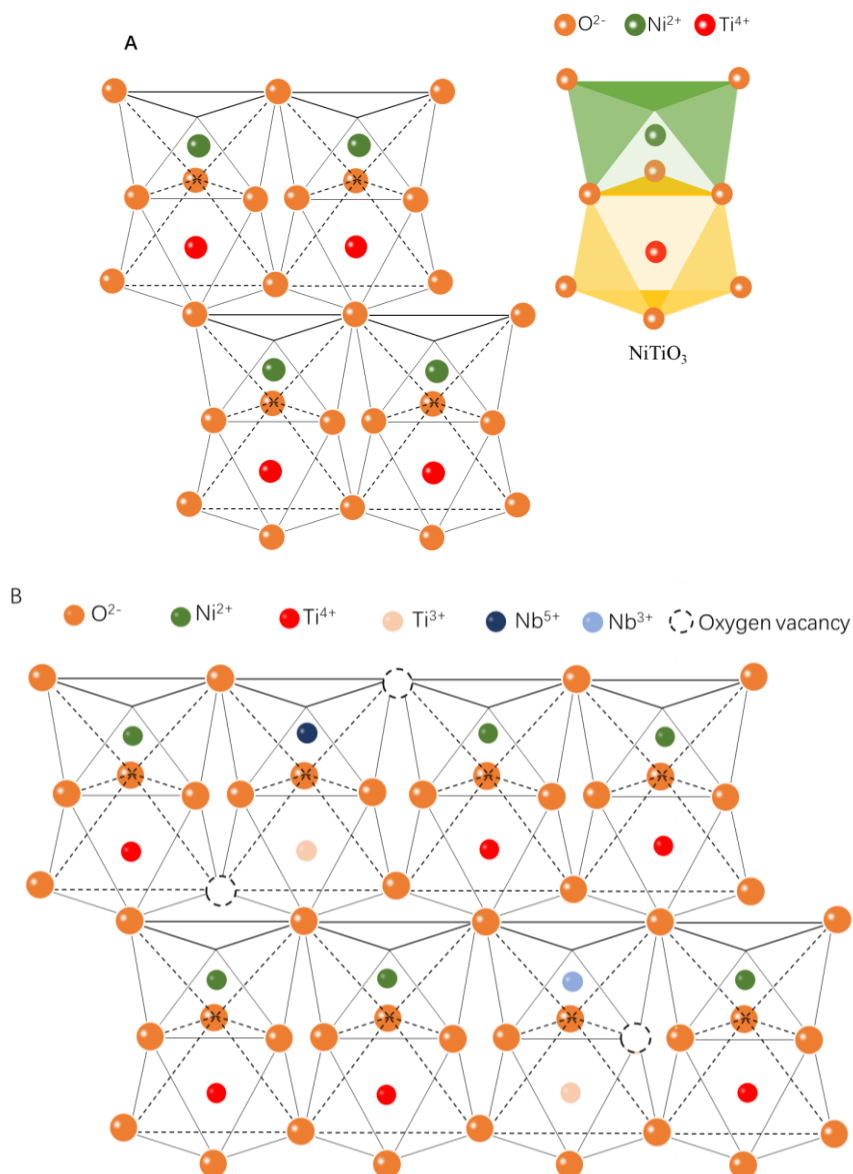


Figure 4.9 Schematic illustration of oxygen vacancy generation in the NiTiO_3 lattice structure by Nb doping. NiTiO_3 lattice structure (A) and Nb-doped NiTiO_3 lattice structure (B).

4.3.3 Optical properties of the photocatalysts

The UV-Vis absorption spectra of the photocatalysts were monitored in Figure 4.10 and the band gaps were calculated from Tauc plots (Table 2 and Figure 4.11). From the band gaps shown in Table 2, it is difficult to identify tendencies in the addition effect

of Nb species into the NiTiO_3 structure. The band gap for NT is 2.52 eV. When the Nb species is added, the band gaps for Nb-containing NiTiO_3 photocatalysts are in the range from 2.43 eV to 2.97 eV without any correlation with the Nb content. Therefore, in this study, it is not clear how the Nb species can modify the band gap of the NiTiO_3 phase.

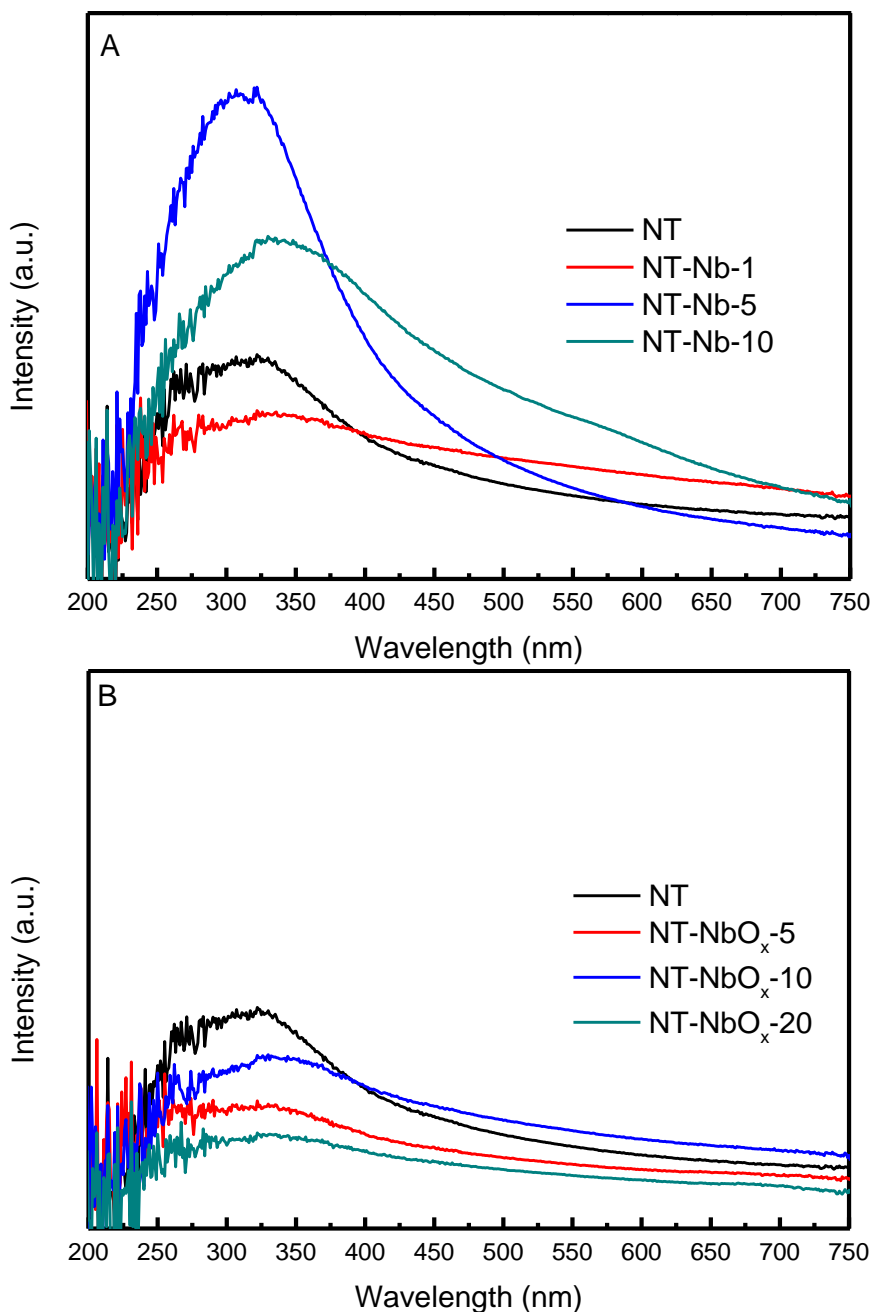


Figure 4.10 UV-VIS absorption spectra of Nb-doped NiTiO_3 (A) and $\text{NbO}_x/\text{NiTiO}_3$ hetero-junction (B).

Table 4.2 Optical properties and photocatalytic reaction rate constants (k_{app}) of the prepared photocatalysts

Samples	Band gap ^a (eV)	k_{app} ^b ($\times 10^3 \text{ min}^{-1}$)
NT	2.52	8.08
NT-Nb-1	2.43	9.67
NT-Nb-5	2.97	12.6
NT-Nb-10	2.61	14.1
NT-NbO _x -5	2.61	3.43
NT-NbO _x -10	2.59	3.28
NT-NbO _x -20	2.59	1.44

^a The values were obtained from the Tauc plot of UV-Vis spectra.

^b The values were obtained from the fit of $-\ln(C/C_0)$ vs. t .

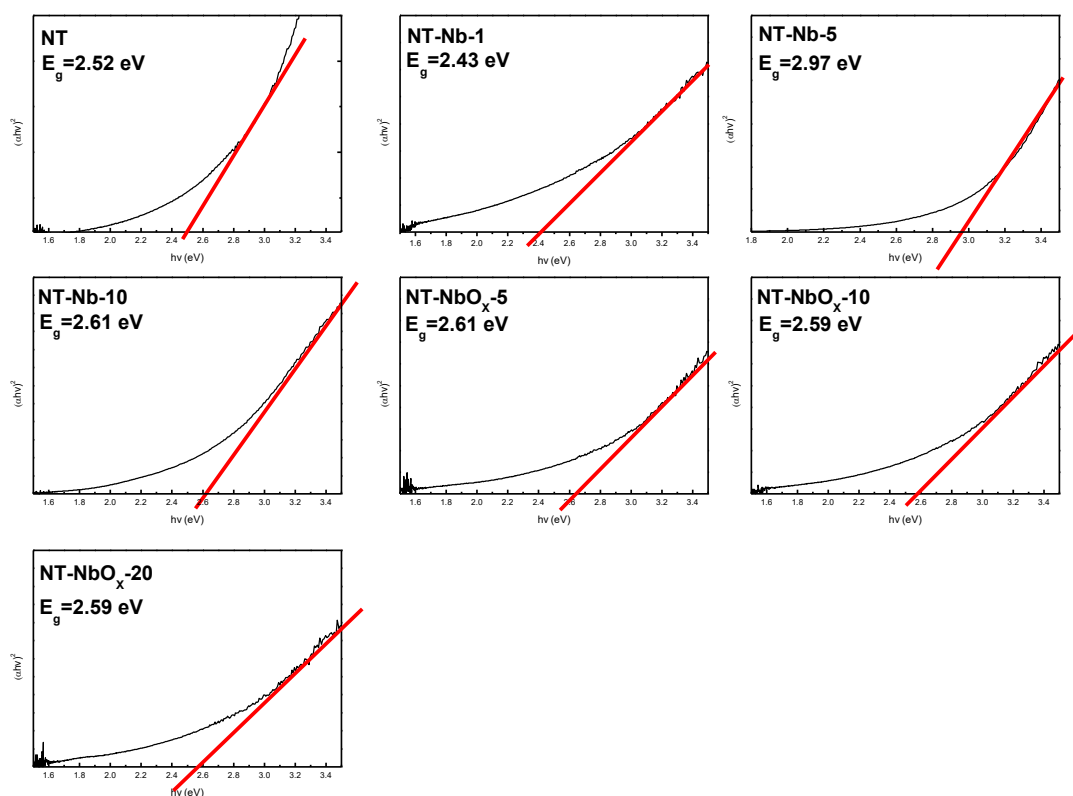
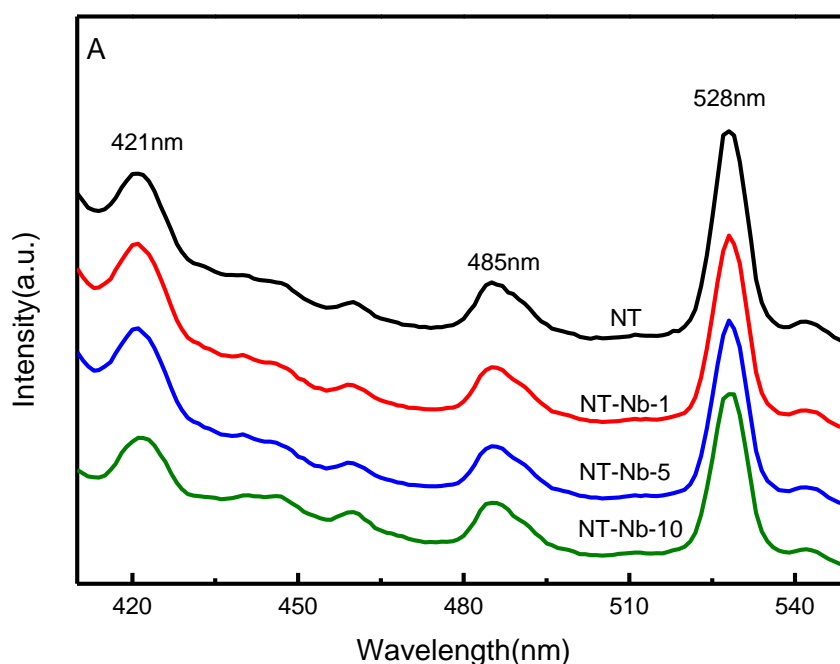


Figure 4.11 Tauc plots for the photocatalysts to calculate E_g .

The modification of the NiTiO₃ lattice structure by the added Nb species affects the PL emission spectra. Figure 4.12 shows the PL emission spectra of the photocatalysts. In Figure 4.12, major PL emission peaks appear at 421, 485, and 528 nm, which are associated with the Ni²⁺/Ti⁴⁺ transitions owing to the crystal field splitting of the NiTiO₃ lattice [46]. The Nb-doped photocatalysts (NT-Nb-x) show a gradual decrease in the PL emission intensity along with the Nb doping amount, whereas the PL emission intensities for the NbO_x/NiTiO₃ heterojunction (NT-NbO_{x-y}) maintain the same intensities or increase at a certain Nb content. For quantitative comparison, we calculated the relative intensities of the PL emission peak at 528 nm on the basis of that for NT, and the results are shown in Figure 4.12C. With an increase in the Nb concentrations in the NiTiO₃ photocatalysts, the relative PL emission intensities of NT-NbO_{x-y} slightly increase but those of NT-Nb-x gradually decrease. The trend in the PL emission intensity for NT-Nb-x is inversely proportional to that of the O_{Ads}/O_{La} ratios. Therefore, abundant oxygen vacancies in Nb-doped NiTiO₃ photocatalysts are essential as a trap center to scavenge the photogenerated electrons (or holes), which results in the lowest PL emission intensity for NT-Nb-10. This is also supported by the EIS data of the photocatalysts. The EIS Nyquist plot is shown in Figure 4.13. A smaller radius in the EIS Nyquist plot implies a more effective separation of the photogenerated electron-hole pairs [47].



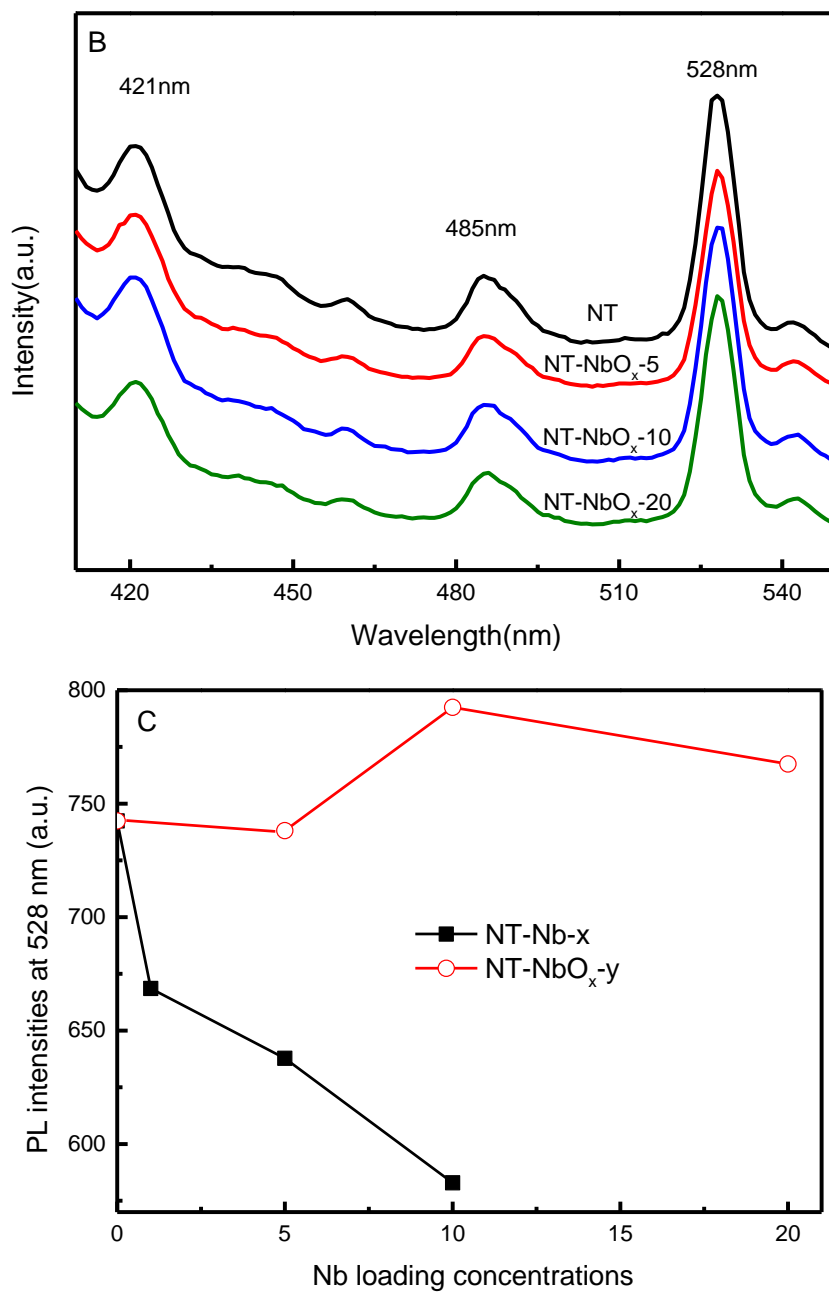


Figure 4.12 PL emission spectra of Nb-doped NiTiO₃ photocatalysts (A), NbO_x/NiTiO₃ heterojunction photocatalysts (B), and PL emission peak intensities at 528 nm vs. Nb loading concentrations (C).

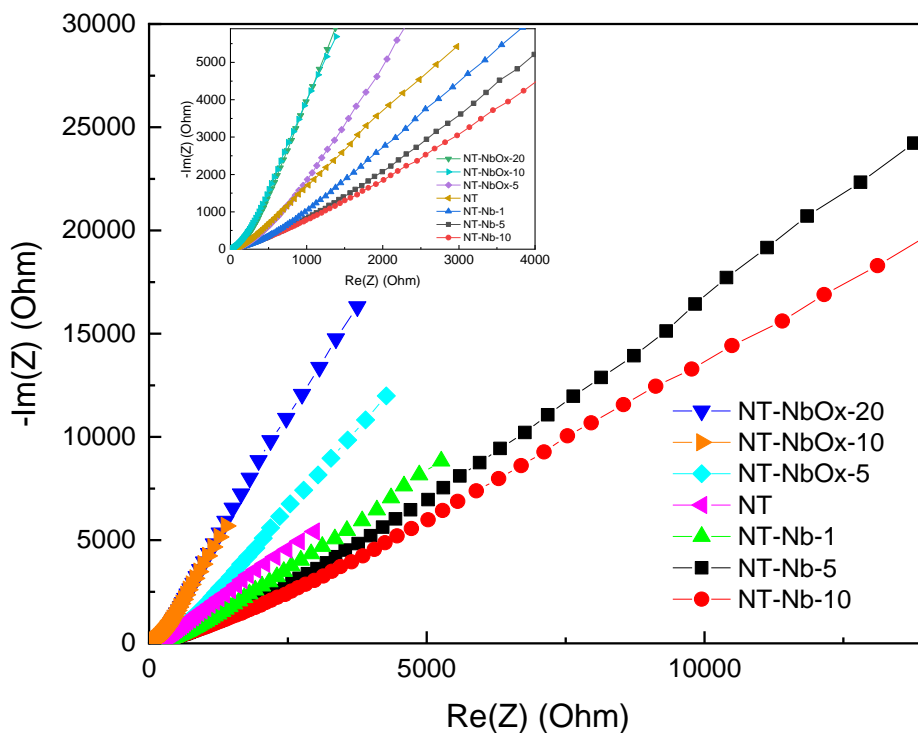


Figure 4.13 EIS Nyquist plots of the photocatalysts.

4.3.4 Photocatalytic behavior of the photocatalysts

The photocatalytic activity of the photocatalysts was investigated through the MB photodegradation in an aqueous solution. Figure 4.14 shows the MB photocatalytic degradation rates of the photocatalysts. The MB photodegradation rates for all NT-Nb-x photocatalysts are clearly higher than that of NT, which indicates that Nb doping improves the photocatalytic activity of the NiTiO_3 photocatalyst. Moreover, it has been determined that the photocatalytic activities of NT-Nb-x photocatalysts are positively proportional to the Nb content in Nb-doped NiTiO_3 photocatalysts. However, NT-NbO_x-y photocatalysts exhibit poor photocatalytic activity, which indicates that the addition of NbO_x to NiTiO_3 inhibits the MB photocatalytic degradation. This behavior differs from that of Nb-doped NiTiO_3 photocatalysts. To quantitatively measure the photocatalytic reaction rates, the apparent photocatalytic rate constant, k_{app} , is obtained from the fit of $\ln(C/C_0)$ vs. t where C and C_0 are the MB concentrations at time t and initial time, respectively. The resultant k_{app} values are listed in Table 4.2. Compared to the k_{app} value for NT of $8.08 \times 10^{-3} \text{ min}^{-1}$, the k_{app} values for NT-Nb-x photocatalysts proportionally increase along with the Nb content. Specifically, the highest k_{app} value

is $14.1 \times 10^{-3} \text{ min}^{-1}$ for NT-Nb-10. However, as previously mentioned, the k_{app} values of NT-NbO_x-y photocatalysts are lower than that of NT in the range of $1.44\text{--}3.43 \times 10^{-3} \text{ min}^{-1}$. The lowest k_{app} value is $1.44 \times 10^{-3} \text{ min}^{-1}$ for NT-NbO_x-20. Consequently, the Nb doping into the NiTiO₃ photocatalyst enhances the photocatalytic activity during the MB photocatalytic degradation, whereas the added NbO_x suppresses the photocatalytic process of the NiTiO₃ photocatalyst during the MB photodegradation.

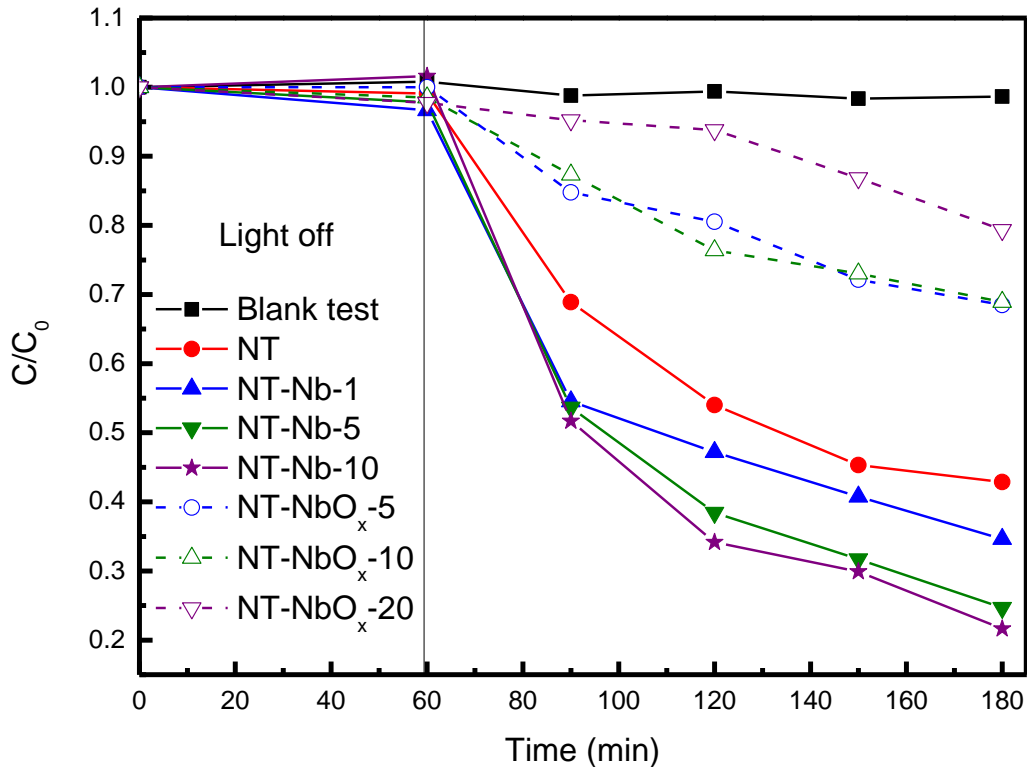


Figure 4.14 MB photocatalytic degradation of pure NiTiO₃, Nb-doped NiTiO₃, and NbO_x/NiTiO₃ heterojunction photocatalysts.

On the basis of the surface characteristics of the photocatalysts and the MB photodegradation results, it is clear that the high photocatalytic activity of Nb-doped NiTiO₃ is caused by the oxygen vacancy in the NiTiO₃ lattice structure and the subsequent low PL emission intensity. For example, NT-Nb-10 with the highest k_{app} value contains the most abundant oxygen vacancy and the lowest combination rate. When Nb species is doped into the NiTiO₃ lattice structure, Nb⁵⁺ (or Nb³⁺) cations are exchanged into Ni²⁺ sites. The charge unbalance between Nb⁵⁺ (or Nb³⁺) and Ni²⁺ produces oxygen vacancies in the NiTiO₃ lattice. The more Nb dopants are pre-

sent, the more oxygen-vacant sites exist in the lattice. Oxygen vacancy naturally reduces the oxidation state of metal cations in the lattice. The XPS data for Nb 3d and Ti 2p clearly confirm the appearance of the less oxidized state of Ti^{3+} and Nb^{3+} at high Nb doping content (NT-Nb-5 and NT-Nb-10). Because oxygen vacancy in the photocatalysts serves as a scavenger to trap the photogenerated electrons (or holes) in the photocatalytic mechanism, NT-Nb-10 has the highest photocatalytic activity with the lowest recombination rate.

In the photodegradation, reactive species such as h^+ , $\bullet OH$, $O_2^{\bullet -}$, and e^- are generated to oxidize the pollutants. The radical trapping experiments for NT-Nb-10 were conducted to confirm the dominant reactive species during the MB photodegradation over NT-Nb-10. The results with different radical scavengers are shown in Figure 4.15. EDTA- Na_2 , IPA, and BQ have almost no effect on the photodegradation efficiency whereas $AgNO_3$ induces a decrease in the MB photodegradation rate, proving that the photogenerated electrons are dominant reactive species in the MB photodegradation.

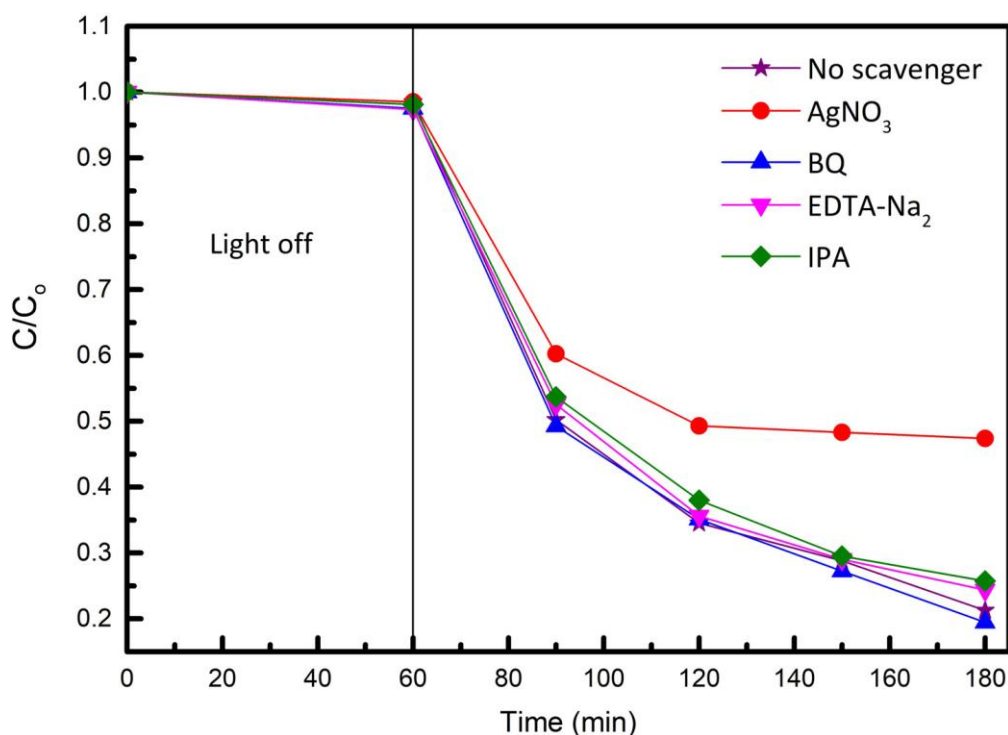


Figure 4.15 Radical trapping experiment results of the MB photocatalytic degradation for NT-Nb-10.

Meanwhile, the photocatalytic activity of the $NbO_x/NiTiO_3$ heterojunction is considerably lower than that of NT, which indicates that the addition of NbO_x inhibits the photocatalytic process of the $NiTiO_3$ photocatalyst. This result can be explained by the

band diagrams of NiTiO₃ and NbO_x. The valence band edge potential (E_{VB}) and the conduction band edge potential (E_{CB}) of semiconductor materials are estimated by the following equations:

$$E_{VB} = X - E_C + 0.5E_g$$

$$E_{CB} = E_{VB} - E_g$$

where E_{VB}, E_{CB}, X, E_C, and E_g are the edge potentials of the valence band (VB) and conduction band, Mulliken's absolute electronegativity (the X-values for NiTiO₃ and NbO_x are 5.79 eV and 5.55 eV, respectively), the energy of the free-electron on the hydrogen scale (approximately 4.5 eV), and the band gap of semiconductors, respectively. The E_g value for NiTiO₃ (2.52 eV) was calculated by the Tauc plot from the UV-Vis absorption spectrum, while the E_g value for NbO_x (3.35 eV) was cited from literature because we could not obtain the UV-Vis absorption spectrum for NbO_x in this study [19]. The calculated values of E_{VB} and E_{CB} for NiTiO₃ are 2.55 eV and 0.02 eV, respectively, whereas the values for NbO_x are 2.725 eV and -0.625 eV, respectively. Figure 4.16 shows the illustration of band diagrams of NT and NbO_x for the NbO_x/NiTiO₃ heterojunction (NT-NbO_x-y). In an ideal match of the band structures in semiconductor heterojunctions, one semiconductor material has a lower conduction band and the other one has a higher VB. The migration between photon-generated holes in the VB and photon-generated electrons in the conduction band enhances the charge separation by forming a loop under sunlight irradiation. However, the band diagrams of NiTiO₃ and NbO_x inappropriately match each other in this study because NbO_x has higher E_{VB} and lower E_{CB} than NiTiO₃, which causes the low separation efficiency of photogenerated electron-hole pairs in NbO_x/NiTiO₃ heterojunction photocatalysts under sunlight irradiation. Consequently, the heterojunction between NbO_x and NiTiO₃ results in an increase in the PL emission intensity and in a decrease in the photocatalytic activity for MB photodegradation.

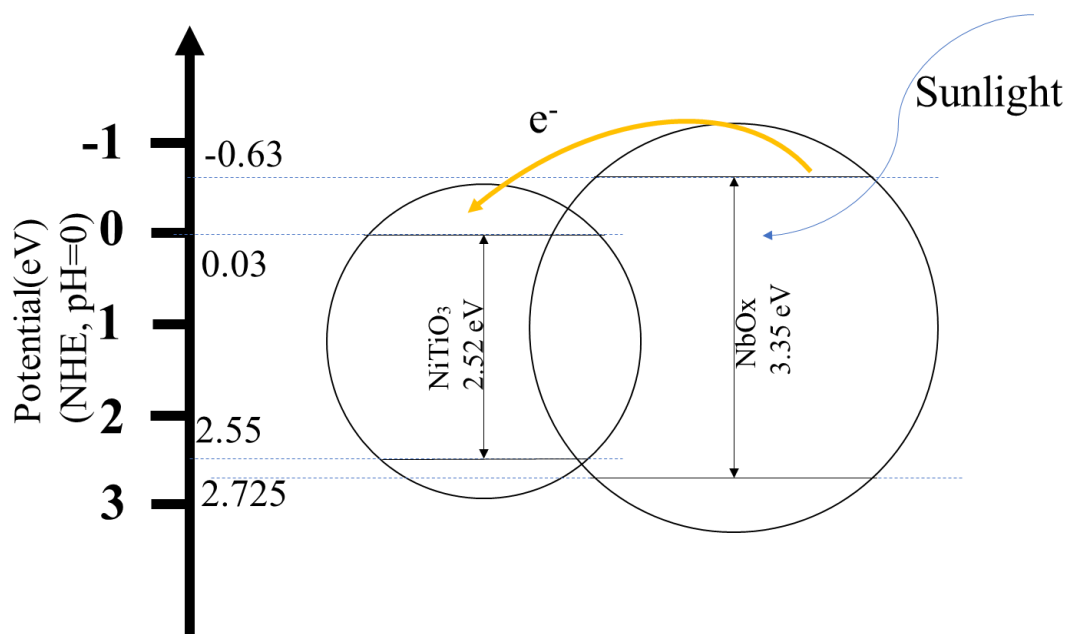


Figure 4.16 Band diagrams for NiTiO₃ and NbO_x in the NbO_x/NiTiO₃ heterojunction

The MO photodegradation for the photocatalysts were additionally conducted. Surprisingly, there is no photodegradation of MO for all the photocatalysts (Figure 4.17). The MO concentrations in the aqueous solution remain unchanged during the photodegradation. The different photocatalytic behavior on the MB and MO photodegradations is ascribed to the IEP values of the photocatalysts. The IEP values for NT, NT-Nb-10 and NT-NbO_x-10 are between 3 and 4 (Figure 4.18), indicating that the surface of the photocatalysts are negatively charged in the aqueous solution during the photodegradation. Since MO has 3.47 of pK_a in aqueous solution at room temperature, it is negatively charged during the photodegradation. That is, MO barely adsorbs on the photocatalysts, resulting in no photocatalytic activity.

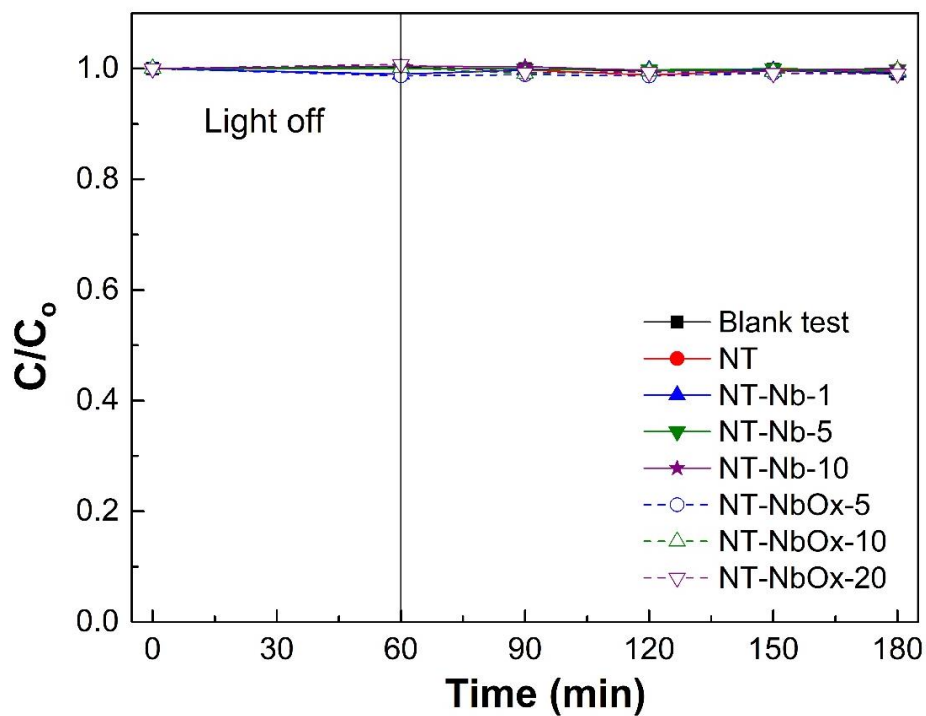


Figure 4.17 MO photocatalytic degradation of all the photocatalysts.

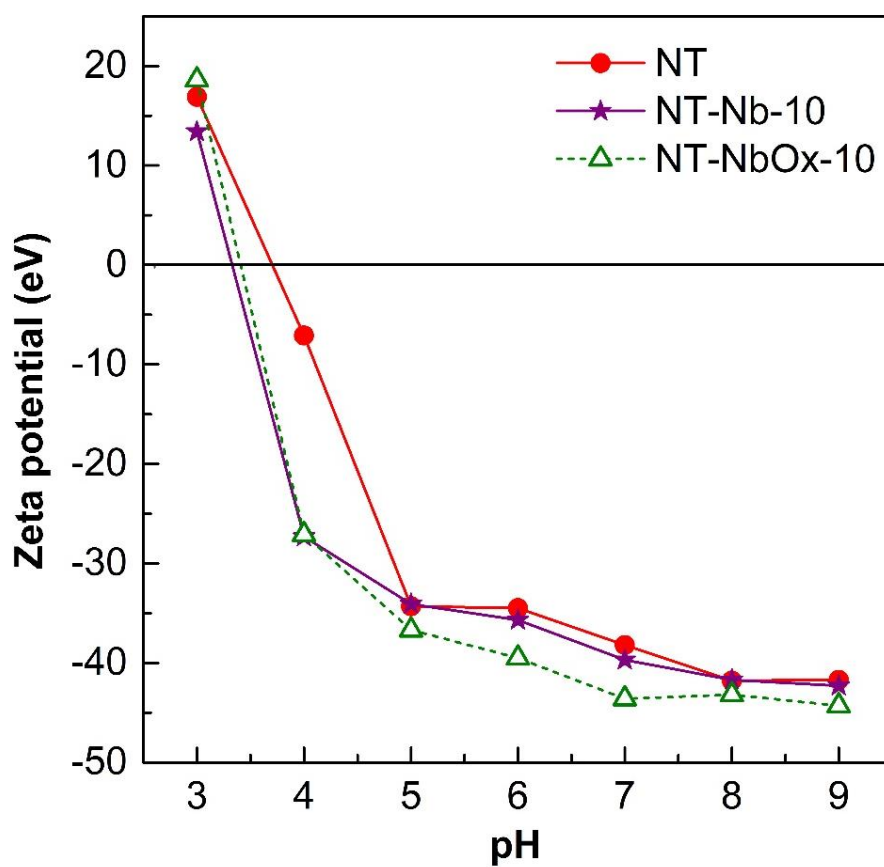


Figure 4.18 Zeta potential of NT, NT-Nb-10 and NT-NbOx-10.

4.4 Conclusion

In this study, we prepare two types of niobium-containing NiTiO_3 photocatalysts (Nb-doped NiTiO_3 and $\text{NbO}_x/\text{NiTiO}_3$ heterojunction) to enhance photocatalytic activity for dye photodegradation under sunlight irradiation. The Nb-doped NiTiO_3 photocatalysts improve the photocatalytic activity of pure NiTiO_3 , whereas the $\text{NbO}_x/\text{NiTiO}_3$ heterojunction decrease the photocatalytic activity. The XPS and XRD results show that Nb doping generates an oxygen vacancy in the lattice, reduces Ti and Nb cations, and transforms the NiTiO_3 phase into a triple metal oxide phase at the high Nb doping content. The high number of oxygen vacancies in Nb-doped NiTiO_3 photocatalysts induce the low recombination rate of photogenerated electron-hole pairs, which results in high reaction rate constant; this result is confirmed by the PL data. However, a decrease in the photocatalytic activity of the $\text{NbO}_x/\text{NiTiO}_3$ heterojunction is caused by the inappropriate band structures of NbO_x and NiTiO_3 in the $\text{NbO}_x/\text{NiTiO}_3$ heterojunction. The higher E_{VB} and lower E_{CB} of NbO_x , compared to those of NiTiO_3 , suppress the charge separation in the $\text{NbO}_x/\text{NiTiO}_3$ heterojunction.

References

- [1] M. Akatsuka, Y. Kawaguchi, R. Itoh, A. Ozawa, M. Yamamoto, T. Tanabe, T. Yoshida, Preparation of Ga_2O_3 photocatalyst highly active for CO_2 reduction with water without cocatalyst, *Appl. Catal., B*, 262 (2020) 118247.
- [2] X. Zhou, H. Yu, D. Zhao, X. Wang, S. Zheng, Combination of polyoxotantalate and metal sulfide: A new-type noble-metal-free binary photocatalyst $\text{Na}_8\text{Ta}_6\text{O}_{19}/\text{Cd}_{0.7}\text{Zn}_{0.3}\text{S}$ for highly efficient visible light-driven H_2 evolution, *Appl. Catal., B*, 248 (2019) 423-429.
- [3] H.Y. Hafeez, S.K. Lakhera, N. Narayanan, S. Harish, Y. Hayakawa, B.-K. Lee, B. Neppolian, Environmentally sustainable synthesis of a CoFe_2O_4 - TiO_2 /rGO ternary photocatalyst: a highly efficient and stable photocatalyst for high production of hydrogen (solar fuel), *ACS Omega*, 4 (2019) 880-891.
- [4] S.N. Paleocrassas, Photocatalytic hydrogen production: A solar energy conversion alternative, *Sol. Ener.*, 16 (1974) 45-51.
- [5] K. Zamaraev, V. Parmon, Potential methods and perspectives of solar energy conversion via photocatalytic processes, *Cat. Rev. - Sci. Eng.*, 22 (1980) 261-324.
- [6] D.P. Macwan, P.N. Dave, S. Chaturvedi, A review on nano- TiO_2 sol-gel type syntheses and its applications, *J. Mater. Sci.*, 46 (2011) 3669-3686.
- [7] C.B. Ong, L.Y. Ng, A.W. Mohammad, A review of ZnO nanoparticles as solar photocatalysts: Synthesis, mechanisms and applications, *Renew. Sust. Energ. Rev.*, 81 (2018) 536-551.
- [8] M. Mishra, D.-M. Chun, α - Fe_2O_3 as a photocatalytic material: A review, *Appl. Catal., A*, 498 (2015) 126-141.
- [9] C. Nguyen-Huy, T.-D. Nguyen-Phan, C.-K. Kim, E.W. Shin, Facile microwave-assisted synthesis and controllable architecture of three-dimensional nickel titanate, *CrystEngComm*, 17 (2015) 4562-4574.
- [10] T.-T. Pham, C. Nguyen-Huy, E.W. Shin, NiTiO_3 /reduced graphene oxide materials synthesized by a two-step microwave-assisted method, *Mater. Lett.*, 184 (2016) 38-42.

- [11] B. Inceesungvorn, T. Teeranunpong, J. Nunkaew, S. Suntalelat, D. Tantraviwat, Novel NiTiO₃/Ag₃VO₄ composite with enhanced photocatalytic performance under visible light, *Catal. Commun.*, 54 (2014) 35-38.
- [12] Y.-J. Lin, Y.-H. Chang, G.-J. Chen, Y.-S. Chang, Y.-C. Chang, Effects of Ag-doped NiTiO₃ on photoreduction of methylene blue under UV and visible light irradiation, *J. Alloys Compd.*, 479 (2009) 785-790.
- [13] S.M. Hosseinpour-Mashkani, M. Maddahfar, A. Sobhani-Nasab, Novel silver-doped NiTiO₃: auto-combustion synthesis, characterization and photovoltaic measurements, *S. Afr. J. Chem.*, (2017).
- [14] T.-T. Pham, S.G. Kang, E.W. Shin, Optical and structural properties of Mo-doped NiTiO₃ materials synthesized via modified Pechini methods, *Appl. Surf. Sci.*, 411 (2017) 18-26.
- [15] N. Lenin, A. Karthik, M. Sridharpanday, M. Selvam, S.R. Srither, S. Arunmetha, P. Paramasivam, V. Rajendran, Electrical and magnetic behavior of iron doped nickel titanate (Fe³⁺/NiTiO₃) magnetic nanoparticles, *J. Magn. Magn. Mater.*, 397 (2016) 281-286.
- [16] K. Jiang, T.-T. Pham, S.G. Kang, Y. Men, E.W. Shin, Modification of the structural properties of NiTiO₃ materials by transition metal dopants: The dopant size effect, *J. Alloys Compd.*, 739 (2018) 393-400.
- [17] Y. Zhang, J. Gu, M. Muruganathan, Y. Zhang, Development of novel α -Fe₂O₃/NiTiO₃ heterojunction nanofibers material with enhanced visible-light photocatalytic performance, *J. Alloys Compd.*, 630 (2015) 110-116.
- [18] J. Huang, Y. Jiang, G. Li, C. Xue, W. Guo, Hetero-structural NiTiO₃/TiO₂ nanotubes for efficient photocatalytic hydrogen generation, *Renew. Ener.*, 111 (2017) 410-415.
- [19] J. Yan, G. Wu, N. Guan, L. Li, Nb₂O₅/TiO₂ heterojunctions: Synthesis strategy and photocatalytic activity, *Appl. Catal., B*, 152-153 (2014) 280-288.
- [20] G. Huang, J. Chen, D. Wang, Y. Sun, L. Jiang, Y. Yu, J. Zhou, S. Ma, Y. Kang, Nb₂O₅/ZnAl-LDH composites and its calcined products for photocatalytic degradation of congo red under visible light irradiation, *Mater. Lett.*, 173 (2016) 227-230.

- [21] R.P. Souza, T.K.F.S. Freitas, F.S. Domingues, O. Pezoti, E. Ambrosio, A.M. Ferrari-Lima, J.C. Garcia, Photocatalytic activity of TiO₂, ZnO and Nb₂O₅ applied to degradation of textile wastewater, *J. Photochem. Photobiol., A*, 329 (2016) 9-17.
- [22] G. Turgut, E.F. Keskenler, S. Aydın, E. Sönmez, S. Doğan, B. Düzgün, M. Ertuğrul, Effect of Nb doping on structural, electrical and optical properties of spray deposited SnO₂ thin films, *Superlattices Microstruct.*, 56 (2013) 107-116.
- [23] K.-H. Sung, S. Cheng, Effect of Nb doping in WO₃/ZrO₂ catalysts on gas phase dehydration of glycerol to form acrolein, *RSC Adv.*, 7 (2017) 41880-41888.
- [24] J.S. Kim, C.W. Ahn, H.J. Lee, S.Y. Lee, S.H. Kang, I.W. Kim, K.S. Lee, Effects of Nb doping on Bi₄Ti₃O₁₂ and Bi_{3.25}La_{0.75}Ti₃O₁₂ ceramics and thin films: different ferroelectric and electrical properties, *J. Korean Phys. Soc.*, 46 (2005) 147-150.
- [25] J. Xing, Z. Shan, K. Li, J. Bian, X. Lin, W. Wang, F. Huang, Photocatalytic activity of Nb₂O₅/SrNb₂O₆ heterojunction on the degradation of methyl orange, *J. Phys. Chem. Solids*, 69 (2008) 23-28.
- [26] M. Qamar, M. Abdalwadoud, M.I. Ahmed, A.M. Azad, B. Merzougui, S. Bukola, Z.H. Yamani, M.N. Siddiqui, Single-pot synthesis of <001>-Faceted N-doped Nb₂O₅/Reduced graphene oxide nanocomposite for efficient photoelectrochemical water splitting, *ACS Appl. Mater. Inter.*, 7 (2015) 17954-17962.
- [27] R. Shao, X. Zeng, Z. Cao, H. Dong, L. Wang, F. Wang, J. Liu, Z. Li, Q. Liang, A novel Ag₃PO₄/Nb₂O₅ fiber composite with enhanced photocatalytic performance and stability, *RSC Adv.*, 5 (2015) 102101-102107.
- [28] F. Peng, H. Gao, G. Zhang, Z. Zhu, J. Zhang, Q. Liu, Synergistic effects of Sm and C co-doped mixed phase crystalline TiO₂ for visible light photocatalytic activity, *Materials*. 10 (2017) 209.
- [29] A. Malathi, P. Arunachalam, J. Madhavan, A.M. Al-Mayouf, M.A. Ghanem, Rod-on-flake α-FeOOH/BiOI nanocomposite: Facile synthesis, characterization and enhanced photocatalytic performance, *Colloids Surfaces A Physicochem. Eng. Asp.* 537 (2018) 435–445.
- [30] S.R. Kim, W.K. Jo, Application of a photostable silver-assisted Z-scheme NiTiO₃ nanorod/g-C₃N₄ nanocomposite for efficient hydrogen generation, *Int. J. Hydrog. Energy*, 44 (2019) 801-808.

- [31] X. Niu, W. Yan, H. Zhao, J. Yang, Synthesis of Nb doped TiO₂ nanotube/reduced graphene oxide heterostructure photocatalyst with high visible light photocatalytic activity, *Appl. Surf. Sci.*, 440 (2018) 804-813.
- [32] X. Huang, H. Zhang, Y. Lai, G. Wang, J. Li, Microwave dielectric properties of the novel low temperature fired Ni_{0.5}Ti_{0.5}NbO₄ + xwt%BiVO₄ (2.5 ≤ x ≤ 10) ceramics, *Mater. Lett.*, 214 (2018) 228-231.
- [33] Q. Liao, L. Li, X. Ren, X. Yu, Q. Meng, W. Xia, A new microwave dielectric material Ni_{0.5}Ti_{0.5}NbO₄, *Mater. Lett.*, 89 (2012) 351-353.
- [34] X. Huang, H. Zhang, Y. Lai, G. Wang, M. Li, C. Hong, J. Li, Relationship of crystal structure and microwave dielectric properties in Ni_{0.5}Ti_{0.5}NbO₄ ceramics with Ta substitution, *Eur. J. Inor. Chem.*, 17 (2018) 1800-1804.
- [35] L. Wang, Y. Wang, Y. Cheng, Z. Liu, Q. Guo, M.N. Ha, Z. Zhao, Hydrogen-treated mesoporous WO₃ as a reducing agent of CO₂ to fuels (CH₄ and CH₃OH) with enhanced photothermal catalytic performance, *J. Mater. Chem.A*, 4 (2016) 5314-5322.
- [36] R. da Costa, A. Rodrigues, P. Pizani, Phase mixture, solid solution or composite: Raman scattering analyses of Ni_xPb_{1-x}TiO₃ and (NiTiO₃)_x+(PbTiO₃)_{1-x}, *J. Alloys Compd.*, 697 (2017) 68-71.
- [37] S.K. Lakhera, H.Y. Hafeez, P. Veluswamy, V. Ganesh, A. Khan, H. Ikeda, B. Neppolian, Enhanced photocatalytic degradation and hydrogen production activity of in situ grown TiO₂ coupled NiTiO₃ nanocomposites, *Appl. Surf. Sci.*, 449 (2018) 790-798.
- [38] Y. Fujioka, J. Frantti, A. Puretzky, G. King, Raman study of the structural distortion in the Ni_{1-x}Co_xTiO₃ solid solution, *Inorg. Chem.*, 55 (2016) 9436-9444.
- [39] G. Yang, W. Chang, W. Yan, Fabrication and characterization of NiTiO₃ nanofibers by sol-gel assisted electrospinning, *J. Sol-Gel Sci. Technol.*, 69 (2014) 473-479.
- [40] Z. Huang, X. Zeng, K. Li, S. Gao, Q. Wang, J. Lu, Z-Scheme NiTiO₃/g-C₃N₄ heterojunctions with enhanced photoelectrochemical and photocatalytic performances under visible LED light irradiation, *ACS Appl. Mater. Inter.*, 9 (2017) 41120-41125.
- [41] Y. Yang, P. Gao, X. Ren, L. Sha, P. Yang, J. Zhang, Y. Chen, L. Yang, Massive Ti³⁺ self-doped by the injected electrons from external Pt and the efficient photocatalytic hydrogen production under visible-Light, *Appl. Catal., B*, 218 (2017) 751-757.

- [42] M. Kwoka, V. Galstyan, E. Comini, J. Szuber, Pure and highly Nb-doped titanium dioxide nanotubular arrays: characterization of local surface properties, *Nanomaterials*, 7 (2017) 456.
- [43] H. Yaghoubi, Z. Li, Y. Chen, H.T. Ngo, V.R. Bhethanabotla, B. Joseph, S. Ma, R. Schlaf, A. Takshi, Toward a visible light-driven photocatalyst: the effect of midgap-states-induced energy gap of undoped TiO₂ nanoparticles, *ACS Catal.*, 5 (2014) 327-335.
- [44] J. Wang, H. Liang, C. Zhang, B. Jin, Y. Men, Bi₂WO_{6-x} nanosheets with tunable Bi quantum dots and oxygen vacancies for photocatalytic selective oxidation of alcohols, *Appl. Catal., B*, (2019) 117874.
- [45] M. Sun, X. Wang, Z. Chen, M. Murugananthan, Y. Chen, Y. Zhang, Stabilized oxygen vacancies over heterojunction for highly efficient and exceptionally durable VOCs photocatalytic degradation, *Appl. Catal. B Environ.*, 273 (2020) 119061.
- [46] J. Wang, H. Liang, C. Zhang, B. Jin, Y. Men, Bi₂WO_{6-x} nanosheets with tunable Bi quantum dots and oxygen vacancies for photocatalytic selective oxidation of alcohols, *Appl. Catal. B Environ.*, 256 (2019) 117874.
- [47] T.-T. Pham, E.W. Shin, Inhibition of charge recombination of NiTiO₃ photocatalyst by the combination of Mo-doped impurity state and Z-scheme charge transfer, *Appl. Surf. Sci.*, 501 (2020) 143992.
- [48] M. Enhessari, M. Sakhaei, A. Salehabadi, L. Etemad, CeO₂/NiTiO₃ nanocomposites; synthesis, photoluminescence and magnetic behavior, *Materials Science-Poland*, 35 (2017) 275-282

5 Highly stable and selective $\text{Co}_x\text{Ni}_y\text{TiO}_3$ for CO_2 methanation

5.1 Introduction

Energy plays the most vital role in the economic growth, industry progress, and nation development. After entering the 21st century, with the rapid social and economic development, global energy consumption has maintained a sustained growth pattern. Although the use of energy promoted the process of human modernization, extensive use of fossil fuels also caused global climate change which will have various effects: melting of glaciers, accelerated sea level rise and threaten of extreme weather. Carbon dioxide is the dominant contributor to climate change, accounts for about three-quarters of the total greenhouse gas emissions. The development of renewable energy and natural gas industries, as well as CO_2 emission reduction are the main trends in the current development of energy and environment [1, 2].

CO_2 hydrogenation can produce various kinds of useful chemicals such as methane, ethanol, formate, methanol, aromatics, dimethyl ether and high-carbon hydrocarbons, with the methods such as catalysis, electrochemical or photo-catalysis reduction [3-9]. Among them, methane is a promising one which has been continuously updated in academic and industrial research. CO_2 methanation, also called the Sabatier reaction, is a promising solution to capturing and transforming CO_2 to energy, which has significant meaning for decrease the CO_2 release as well as develop carbon industry. Methanation of CO_2 could store renewable H_2 by forming the synthetic natural gas (SNG) [10-12]:



Thermodynamically, low reaction temperature is favored. However, in order to enhance the reaction kinetics and activate reaction molecule, high temperatures over 350°C is also frequently selected in reaction [13-15]. High temperature will waste more energy and easily causes the deactivation of catalysts by sintering and carbon deposition. The noble metal catalysts usually show high activity, especially Ru, Rh and Pd [16-19]. However, the unignorable cost and limited reserves restricts their implementation at an industrial scale driven the search of alternative catalyst made of earth-abundant elements [20].

Ni-based catalysts are paid with high attention and widely used in methanation process due to their low-cost and comparable catalytic activity. However, the deactivation due to carbon deposition, nickel sintering, CO poisoning, thermal degradation also appears on nickel catalysts [17, 21-24]. In order to overcome the drawbacks, extensive oxides Al_2O_3 , SiO_2 , TiO_2 , CeO_2 were introduced into Ni-based catalysts as support [2, 13, 25-27]. Bian et al. investigated a high oxygen vacancies and high surface Ce^{3+} concentration Ni/ CeO_2 -NR catalyst which show high CO_2 methanation performance [28]. Jia et al. achieved low temperature activity for CO_2 methanation by Ni/ ZrO_2 catalyst with more Ni (111) phase and high Ni dispersion [29]. Daroughegi et al. studied the effect of adding promoters on Ni- Al_2O_3 catalyst and found that stronger interaction between metal species and alumina support, resulting in the formation of smaller crystallite size, which positively affect the catalytic performance of in CO_2 methanation [30]. Although kinds of support can improve reaction activity, the catalyst deactivation problem of carbon deposition caused by the formation of other substances (such as NiAl_2O_4) at high temperature is still exists [31].

Herein, synthesis a Ni-based perovskite structure catalyst by adding a basic support might be a potential method. Nickel titanate (NiTiO_3), as a Ti-based perovskite material, which has low cost, narrow band gap (2.18 eV), good ionic conductivity, electronic transport and hydrogenation reaction, now has been applied in the photocatalytic and electrocatalytic field [32-34]. Perovskite material could be a high activity and stable catalysts because of the flexibility of the chemical diversity and electronic structure. It was reported that transition metal oxide supports could change the chemistry of metal particles via migration and spillover, and hence improve the catalytic performance and stability [35].

Thus, in order to further improve the catalytic effect, we attempt to enhance the activity and stability of the catalyst by adding Co ions. Pure NiTiO_3 and Co doped NiTiO_3 are investigated in this study. Combining structure characterization of the catalysts and the reaction result, possible influencing factors include oxygen vacancies, surface defects, metal reduction degree and electron transfer were explored and confirmed.

5.2 Experimental

5.2.1 Materials preparation

Nickel nitrate hexahydrate ($\text{Ni}(\text{NO}_3)_2 \cdot 6\text{H}_2\text{O}$, Sinopharm Group Co. Ltd.), cobalt nitrate hexahydrate ($\text{Co}(\text{NO}_3)_2 \cdot 6\text{H}_2\text{O}$, Sinopharm Group Co. Ltd.), titanium n-butoxide [$\text{Ti}(\text{OC}_4\text{H}_9)_4$, 98%, Sigma-Aldrich], Anhydrous ethyl alcohol ($\text{C}_2\text{H}_5\text{OH}$, 99.9%, Sinopharm Group Co. Ltd). Citric acid monohydrate ($\text{C}_6\text{H}_8\text{O}_7 \cdot \text{H}_2\text{O}$, Sigma-Aldrich). All chemical reagents were used as received without further purification.

The Co doped NiTiO_3 catalyst was synthesized as follows. First, 1.5g citric acid monohydrate was placed into 100 mL of ethanol. The required amount of nickel nitrate hexahydrate and cobalt nitrate hexahydrate as metal precursors were dissolved in this solution with well stirring. After that titanium n-butoxide was added dropwise to the mixed solution and the final solution was continuously stirred for 1 h at room temperature. The resulting homogeneous solution was evaporated at 80 °C to give a dark green (for NiTiO_3) or purple (Co doped NiTiO_3) precipitate. Finally, the dried powder was calcinated at 500 °C for 6 h (ramping rate = 2 °C/min).

5.2.2 Characterization

The crystal structure and phase purity of all catalysts were examined by powder X-ray diffraction (XRD) on Rigaku Ultimate IV powder X-ray Cu K α radiation diffractometer in the 2θ range of 20–80° (40.0 kV, 40.0 mA).

The Brunauer-Emmett-Teller (BET) measurements were examined on a micromeritics ASAP 2460 analyzer.

The Fourier transform infrared spectroscopy (FTIR) were recorded using an Nicolet380 infrared spectrometer (USA) equipped with attenuated total reflectance (ATR) at room temperature in the range of 4000–400 cm^{-1} and the average value for 32 scans was recorded.

The X-ray Photoelectron Spectroscopy (XPS) spectrum of the samples was recorded by the VG system (MiltiLab 2000). C1 s was adjusted to 284.8 eV as a reference signal.

H_2 -temperature programmed reduction with hydrogen (H_2 -TPR) was detected with Auto Chem 2920II (Micromeritics) equipped with a thermal TCD detector. Typically, 50 mg catalyst was placed in the tube pretreated in argon at 200 °C for 1.0 h to

remove adsorbed water, and then cooled to 50 °C. A cold trap was prepared to prevent water from entering the TCD. The sample was heated in H₂ at a ramp of 10 °C·min⁻¹ in the temperature range of 50 °C to 800 °C with a H₂ at a flow rate of 30 mL/min.

CO₂-temperature programmed desorption (TPD) experiments were performed using Auto Chem 2920II (Micromeritics). First, catalyst (0.05 g) was placed in the tube pretreated in argon (30 ml/min) for 200 °C for 1.0 h to remove physically adsorbed water and impurities. The sample was heated in H₂ at a ramp of 10 °C·min⁻¹ from 50 °C to 500 °C for 1 h and then cooled to room temperature with Ar. Succinctly, CO₂ was passed over the reduced catalyst at 50°C for 1 h to achieve absorption/desorption balance. Then the sample was then purged with 20 mL/min Ar for 40 min to remove the physisorbed CO₂. Finally, the temperature was ramped from 50 °C to 500 °C at a rate of 10 °C /min, while the TCD signal was recorded continuously.

5.2.3 Catalytic performance

The CO₂ methanation reactions were carried out using a fixed-bed quartz tube reactor. 0.1g catalyst was pelletized to 40-60 mesh and packed into a fixed-bed quartz reactor vertically. PID temperature controller system was put on top of the catalyst bed to control the temperate. The catalysts were reduced in 30 ml/min H₂/N₂ gas flow (H₂/N₂=2:1) at 500 °C for 1 hour. The catalytic activity was measured by temperature range from 150 °C to 450 °C at 50 °C intervals with the feeding gas consisted of 10% CO₂, 40% H₂, and 50% N₂ at a flow rate of 20 ml/min control by the mass flow controller. The reaction products were analyzed by online gas chromatography (GC-2014C, Shimazu) equipped with Packed PQ column and C13X molecular sieve column by thermal conductivity detector (TCD). The CO₂ conversion and product selectivity like CH₄ and CO can be calculated as shown

$$X_{(CO_2)} = \frac{CO_2(in) - CO_2(out)}{CO_2(in)}$$

$$S_{(CH_4)} = \frac{CH_4(out)}{CH_4(out) + CO(out)}$$

$$S_{(CO)} = \frac{CO(out)}{CH_4(out) + CO(out)}$$

Where X_{CO_2} is the conversion of carbon dioxide; S_{CH_4} and S_{CO} are the respective selectivity of CH_4 and CO ; Where CO_2 (in) and CO_2 (out) represent the molar flows of CO_2 at the inlet or outlet, CH_4 (out) and CO (out) are the molar flows of the outlet CH_4 and CO .

To compare the effects of the reaction parameters on the conversion, additional reactions were performed with different reaction temperatures and gas hourly space velocities (GHSV). N_2 gas was used as the balance gas for flow control.

5.3 Results and discussion

5.3.1 Catalysts characterization

Fig. 5.1 show the XRD diffractograms of the prepared catalysts obtained before hydrogen reduction and after reaction. The characteristic peaks of $NiTiO_3$ rhombohedral perovskite structure were observed for both pure and Co modified $NiTiO_3$ samples with symmetric and sharp reflections of the basal (012), (104), (113), (202), (024), (116), (214) planes at 2θ of 24.1° , 33.1° , 40.8° , 43.5° , 49.4° , 54.0° , 62.4° , respectively (JCPDS 33-0960)[36]. No impure peaks such as CoO , TiO_2 or NiO were detected, confirming the phase purity and crystallinity. A slight peak shift could be observed on high Co doping materials, while there is no change in low content doping samples. After reduction, prepared samples still keep the $NiTiO_3$ structure and the main phase was transferred into Ni metal at 2θ of 44.3° (JCPDS 04-0850), while traces of TiO_2 (rutile) and TiO_2 (anatase) were observed in the reduction catalyst (JCPDS 21-1276 and JCPDS 21-1272) [36]. In general, the presence of nickel oxide should be detected on nickel-containing catalysts. However, here is no nickel oxide peak could be observed, which may indicate that the perovskite structure inhibits the formation of nickel oxide[34, 37]. In other words, the perovskite structure may help control the formation of smaller oxide particle size or make the dispersion uniform. In addition, the Co ions were well incorporated into the $NiTiO_3$ lattice structure and no peaks of Co reflections were observed. However, the insertion of high Co ion lead to a slight peak shift in both

before and after reaction samples. The average crystallite size of reduction catalyst calculated from the Scherrer equation of the (111) main planes for all of the catalysts yielded values of 19.5 nm and 16.4 nm for samples NiTiO₃ and CoNT-1 respectively. The particle size change with the doping of cobalt, suggesting that the addition of doping metal may alter the particle size of NiTiO₃ support.

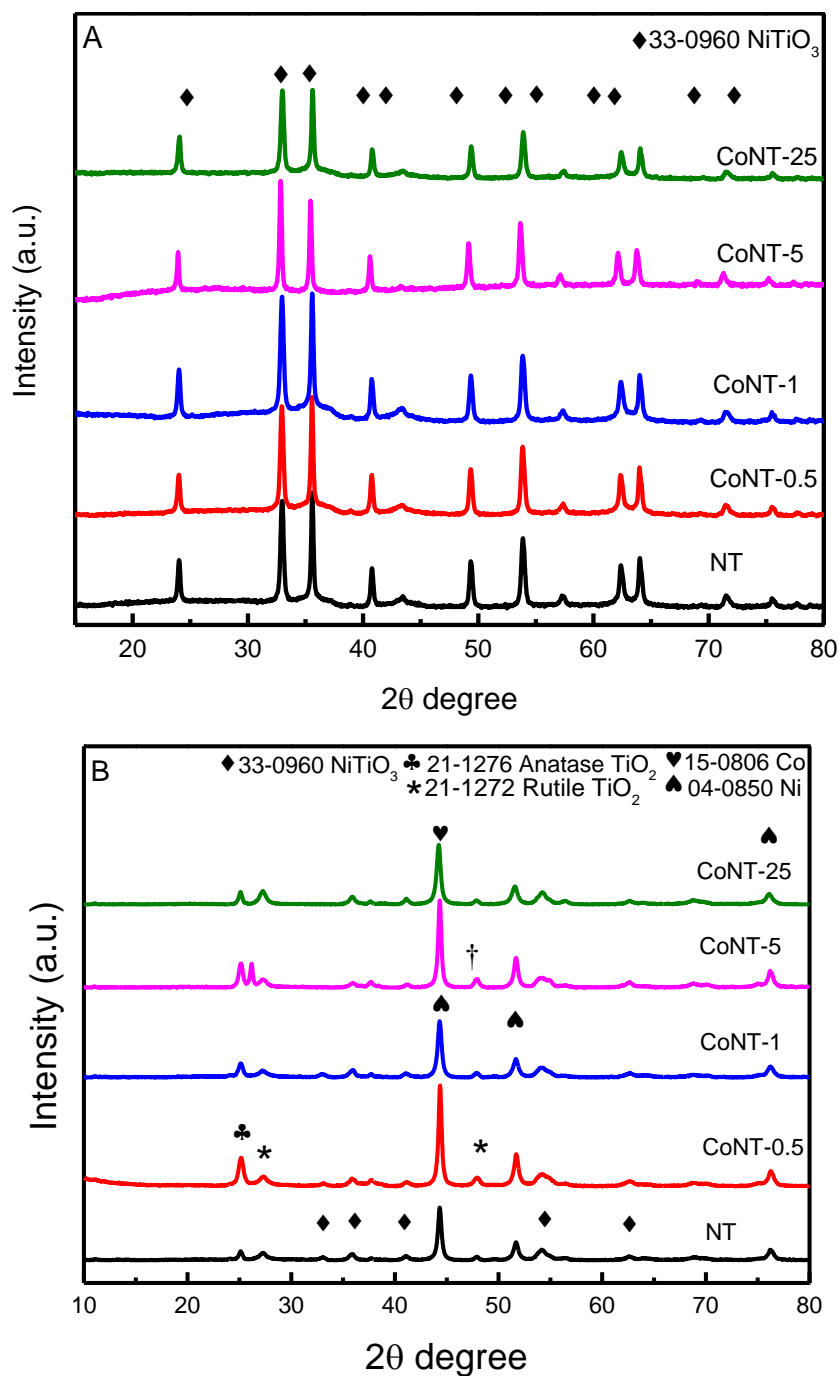


Figure 5.1 XRD result of (A) before hydrogen reduction and (B) after reaction CoNT-X catalysts.

The N₂ adsorption-desorption measurements were carried out to obtain more information on prepared catalysts structural property, as summarized in Table 1. A change of specific surface area and pore volume is observed due to doping with cobalt. It was seen from Fig. 5.2 that the curve shape of the catalysts displays classic IV type curve (IUPAC) with H3 hysteresis loop confirming the mesoporous and macroporous properties. Fig. 5.3 shown the FE-SEM images of pure and modified CoNT-x samples. All materials have the same morphology of nanoparticle aggregates, which exhibits a typical shape of NiTiO₃.

Table 5.1 Physico-chemical properties of the prepared materials

Samples	2 θ at 44.2° ^a (111)	S _{BET} ^b (m ² /g)	Pore volume ^c (cm ³ /g)	Pore size ^d (Å)	O _{Ad} /O _{La} ratio ^e	Ni ⁰ /Ni ²⁺ ratio ^f
NT	19.5	66.43	0.093	49.00	0.37	0.225
CoNT-0.5	20.6	87.05	0.091	37.90	0.41	0.246
CoNT-1	16.4	59.33	0.085	49.16	0.62	0.258
CoNT-5	21.0	76.11	0.088	41.08	0.51	0.231
CoNT-25	17.1	52.39	0.092	62.26	0.50	0.216

^a Average crystalline sizes were obtained based on (111) diffraction of the reacted catalysts *via* the Debye-Scherrer equation.

^{b,c,d} Specific surface area were calculated from the fit of the Brunauer-Emmett-Teller (BET) equation to N₂ adsorption-desorption isotherms.

^e The values were acquired from the XPS data for O 1s.

^f The values were obtained from the XPS data for Ni 2p. The Ni⁰/Ni²⁺ ratios reflect the surface reduction.

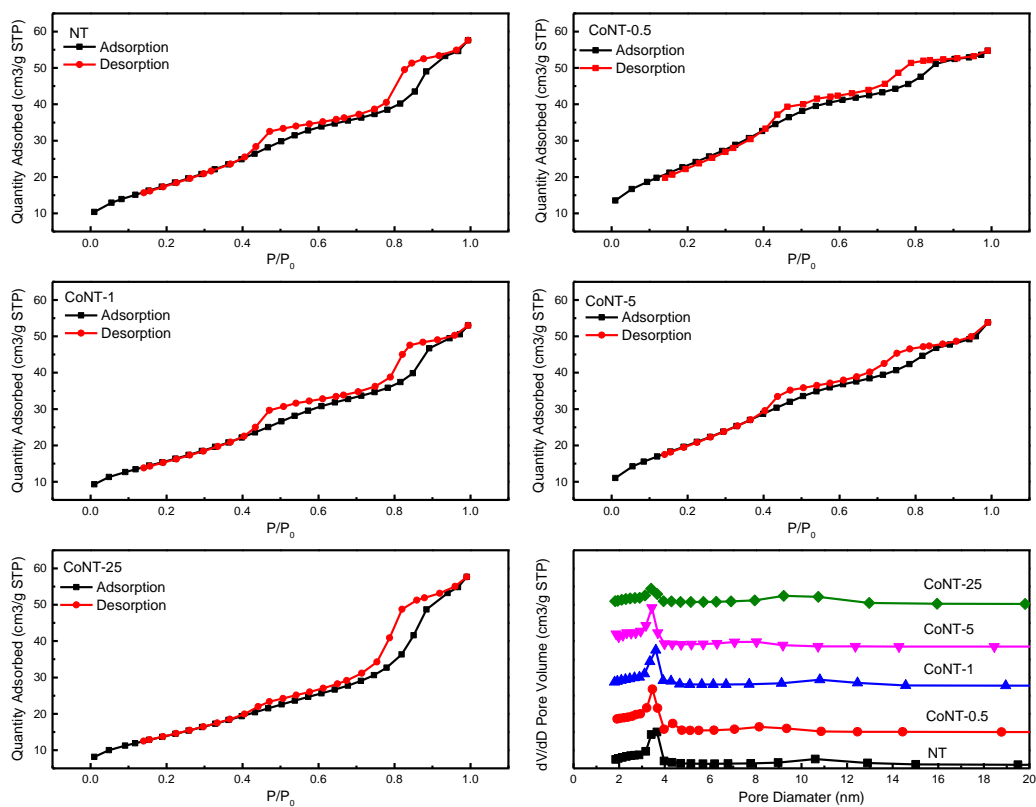


Figure 5.2 N_2 sorption isotherms for fresh CoNT-X catalysts

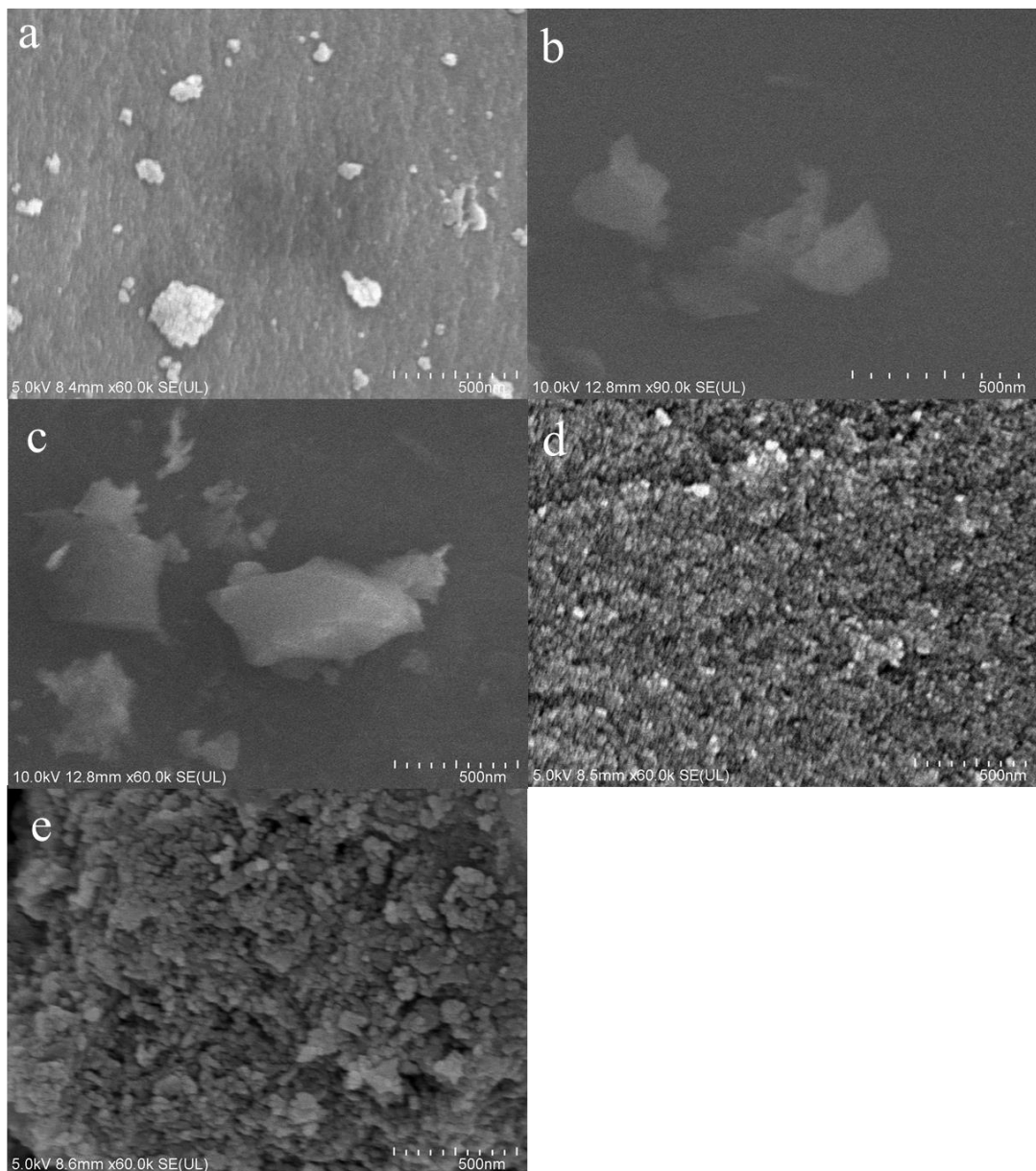


Figure 5.3 SEM images for a)NT b)CoNT-0.5 c)CoNT-1 d)CoNT-5 and e)CoNT-25

XPS measurements were also performed to investigate the oxidation state of prepared material. Fig. 5.4 shows the Ti 2p spectra, peak of the Ti 2p_{3/2} and Ti 2p_{1/2} could be observed at the 458.6 and 464.3 eV, with a gap about 5.7 eV, meaning a typical characteristic of the Ti⁴⁺ in the NiTiO₃ structure. Two components representing the Ni 2p_{3/2} at 855.7 eV and Ni 2p_{1/2} at 873.1 eV spin-orbit levels were observed in the Ni 2p spectra for both pure NiTiO₃ and Co doped samples. Satellite peaks were observed, but all assigned peaks indicated the presence of metallic Ni in NiTiO₃.

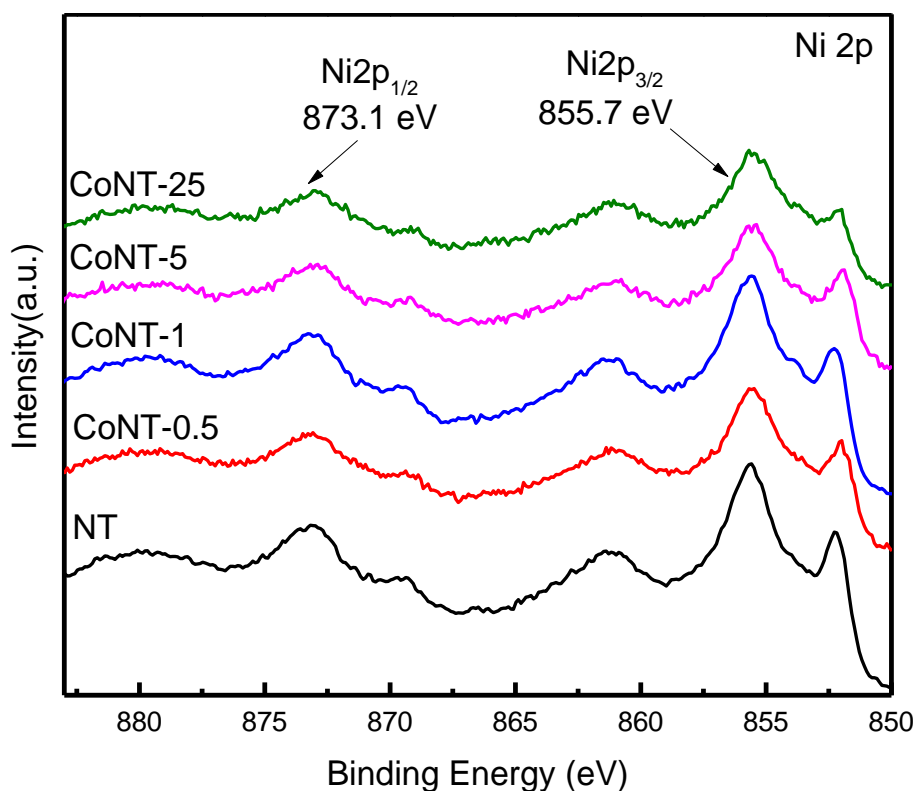
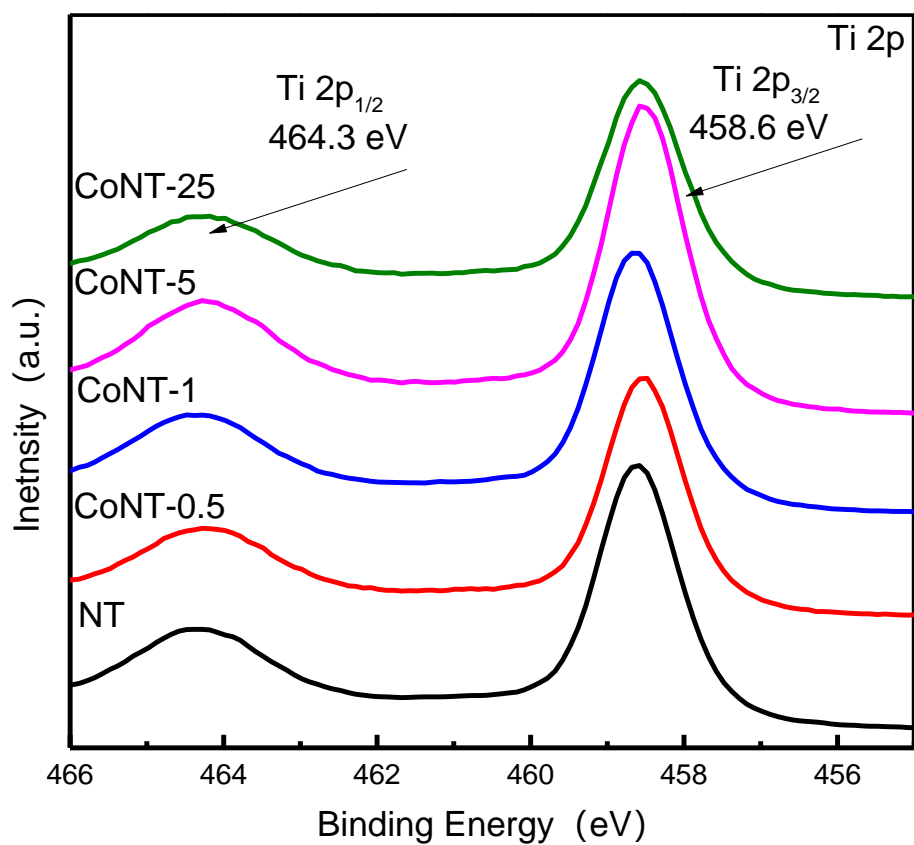


Figure 5.4 XPS result of Ti 2p and Ni 2p of CoNT-X.

The assigned peak at low binding energy indicated the presence of Ni metal (Ni^0) in NiTiO_3 in Fig 5.5. It was consistent with the literature that metallic Ni nanoparticles

were the catalytically active phase for the reaction [38]. Satellite peaks were observed and Ni(OH)₂ peak was observed at 855.7 eV for all reduced catalyst [34]. A slight shoulder peak apparent between the 853.0 eV and 855.8 eV peaks in these spectra, which corresponds to NiO (853.8 eV) [39]. The formation of oxide state on the Ni nanoparticles is once again most likely to occur during aerobic transfer to the XPS instrument. The results of Ni⁰/Ni²⁺ peak area ratio was given in Table 1. It can be seen that there is a stronger Ni intensity for the CoNT-1 compared to the other catalysts, suggesting increased reduced surfaces. This may imply that cobalt doping affects the electronic distribution of the material and strengthens the reduction ability of nickel.

In Fig. 5.5, the O 1s spectra indicate the presence of surface lattice oxygen (O_{la}) in the catalyst and surface adsorbed oxygen (O_{ad}) [40]. The peak at 529.9 eV can be assigned to the lattice oxygen associated with the metal-oxide bond (M = Ni, Ti or Co), and the peak at 531.2 eV is attributed to non-lattice oxygen or the OH group[34]. On the basis of the integral area of O_{ad} and O_{la} species, the ratios of O_{ad} / O_{la} were calculated and listed in Table 1. Compared with CoNT-x, CoNT-1 contained a higher ratio of non-lattice oxygen, indicating the formation of oxygen defects in the lattice due to Co addition. According to Xie et al. report, since O_{ad} is related to chemically adsorbed oxygen on the surface, it can also be used to reflect the adsorption capacity of CO₂ in this reaction, which means the ratio of O_{ad}/O_{la} could be supposed to evaluate the CO₂ capture ability of the corresponding catalysts.[41] Besides, the bridging oxygen atom located in the two interfaces, between metal and oxide or between types of oxide, has an unignorable influence on the activity. According to previous research, the electron cloud density of bridging O atoms affects the surface basicity. The study by Li et al. established the Ni dispersion and size-dependent reactivity on the CO₂ methanation over Ni/Y₂O₃ with citric acid and concluded the increases of electron cloud density on Ni and bridged providing abundant basic on 12CA-Ni/Y₂O₃ catalyst [42]. Wang et al. prepared Zn_xZr_yO_z catalysts and their characterization results show Zn provide part of its electrons to bonded bridged oxygen and resulting in the increase of electron cloud density of O [43]. Therefore, the ratios of O_{ad}/O_{la} and Ni⁰/Ni²⁺ with cobalt modification indicate that the change of electron cloud density on Ni and bridged O, $\overset{\text{(Ti-O)-Ni}}{\text{O}} \curvearrowright$, which means the basic sites was enhanced on CoNT-1 catalyst. The basic sites will be further discussed in CO₂-TPD.

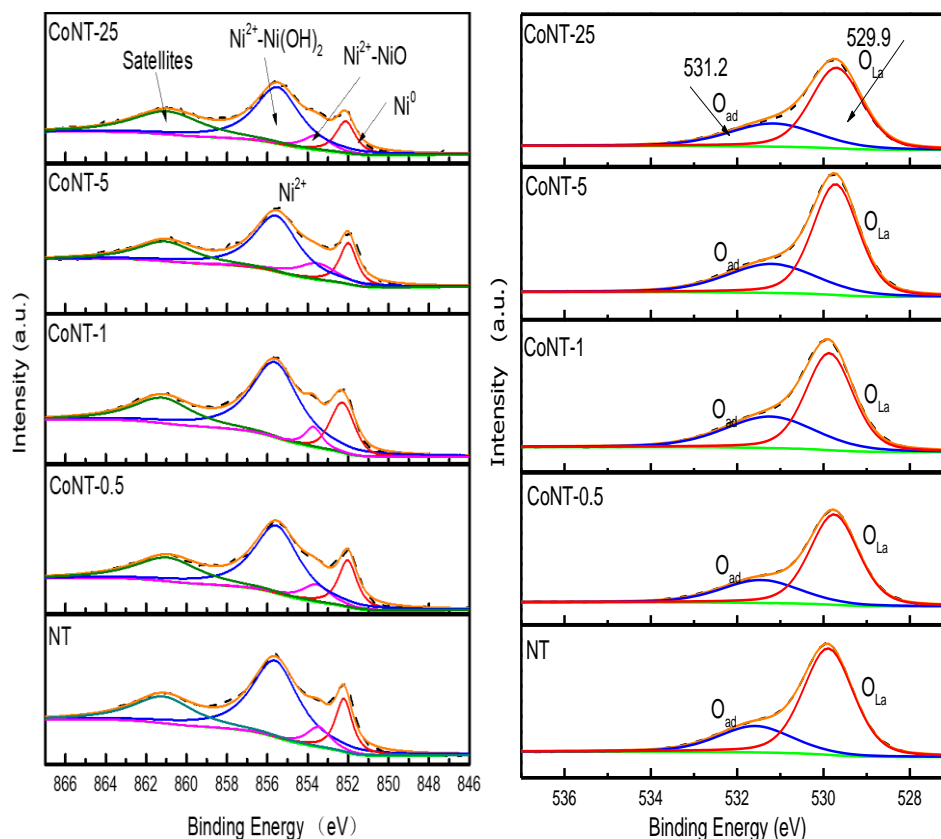


Figure 5.5 Deconvoluted XPS data of Ni 2p and O1s for CoNT-X catalyst. Black line is the experimental data and yellow/blue/red/green lines are the fitted data.

The XPS Co 2p peak is shown in Fig. 5.6 The core level Co 2p exhibits the Co $2p_{3/2}$ at the binding energies of 780.8 eV with the strong shake-up satellite peaks at 785.9 eV. The values match the features of the high-spin Co^{2+} , which demonstrates an oxidation state of Co^{2+} element in the CoTiO_3 . Co^0 also could be found at 777.8 eV. No obvious peaks can be observed until high Cobalt concentration in CoNT-25. This is consistent with the XRD results, which indicated the absence of CoO or other impurity metal oxide in low doping content samples and solid solution incorporation of Co into the NiTiO_3 structure [44]. The peak at 780 eV shifted toward higher value as cobalt concentration increasing, suggesting decreasing the density of charge on the surface of the cobalt because of the electron transformation. These electrons may move to oxygen and nickel, proved by the XPS results above.

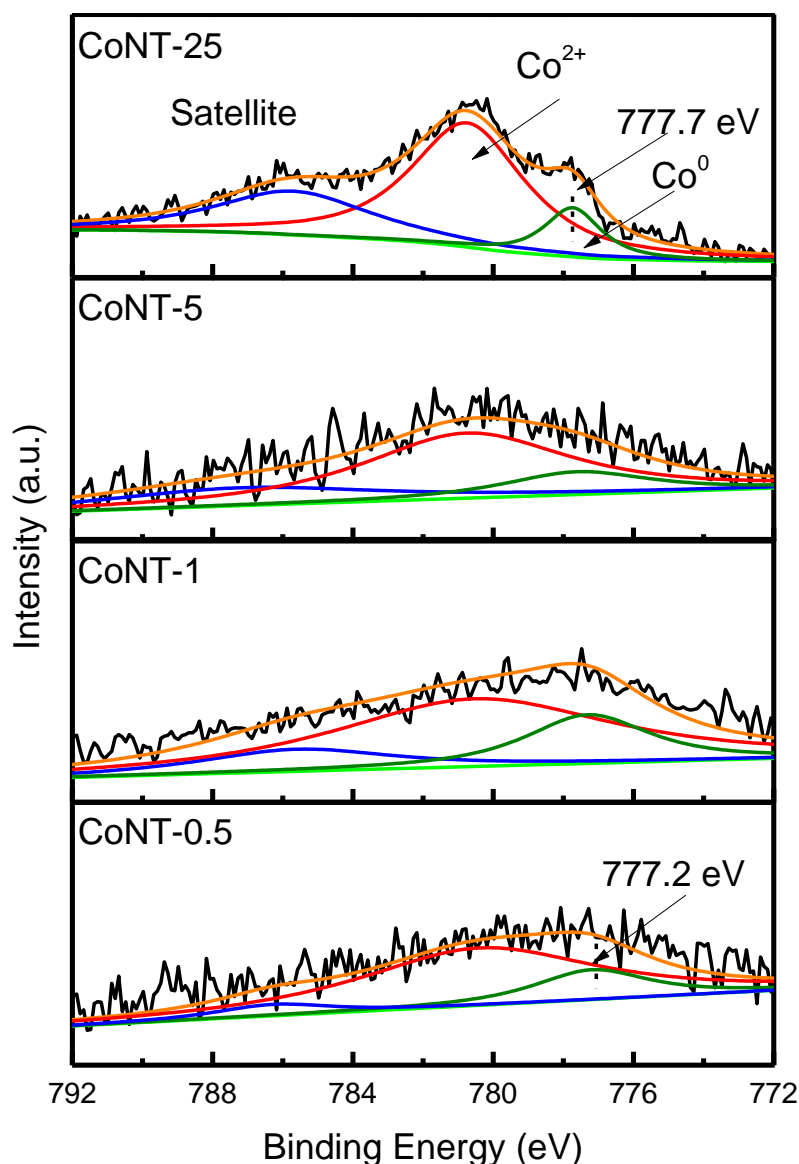


Figure 5.6 Deconvoluted XPS data of Co 2p for CoNT-X catalyst. Black line is the experimental data and yellow/blue/red/green lines are the fitted data, the peak value of CoNT-0.5,1,5 was magnified twice.

The adsorption capacity of the catalyst for the reactant gas play an important role in catalyst performance. The hydrogen temperature-programmed reduction (H_2 -TPR) illustrated the reducibility and the interactions of the prepared catalysts in Fig. 5.7 and Table 2. Different reduction peak types indicate the exist of kinds of metal oxide species with different degrees of aggregation on the catalyst [45]. There were several overlapped hydrogen-consuming peaks at the varied reduction temperatures. The first reduction peak located around 400 °C, which could be attributed to the no interacting or weak interaction of the nickel oxide and cobalt oxide with perovskite support.[46, 47] In all samples, the small peaks between 300 and 400 °C were assigned to the re-

duction of free NiO and CoO which was not interacting with the support. The higher temperature peaks above 500°C were assigned to the reduction of oxide having strongly interacted with the metal oxide support. With the insertion of Co, the curve of CoNT-1 moved about 20 °C to left side compared to pure NT, indicating that the nickel species over CoNT-1 were more easily reducible. Highest H₂ consumption of CoNT-1 also indicated the reduction degree was enhanced after cobalt doping., as shown in **Table 2**. A possible hypothesis is that Co ions are inserted into the NiTiO₃ lattice, leading to structural defects, such as oxygen vacancies. Due to the appropriate amounts of Co doping, nickel species were exposed and relatively easily reduced.

Table 5.2 Chemical adsorption of H₂-TPR and CO₂-TPD

	Reduction temperature ^a	H ₂ consumption ^a mmol·g ⁻¹	Basicity (mmol/g·cat) ^b				
			Weak	Medium	Strong	Med/Tol ^c	
NT	409.5	3.15	4.22	6.31	6.52	1.34	0.35
CoNT-0.5	401.1	3.27	3.89	4.9	4.26	1.54	0.29
CoNT-1	390.2	3.62	4.09	4.36	8.68	1.73	0.46
CoNT-5	409.3	3.47	3.1	3.32	4.05	1.45	0.34
CoNT-25	421.6	3.36	2.98	3.47	2.59	1.57	0.24

^a H₂-TPR result

^b CO₂-TPD result

^c the ratio of medium basic sites to total basic sites

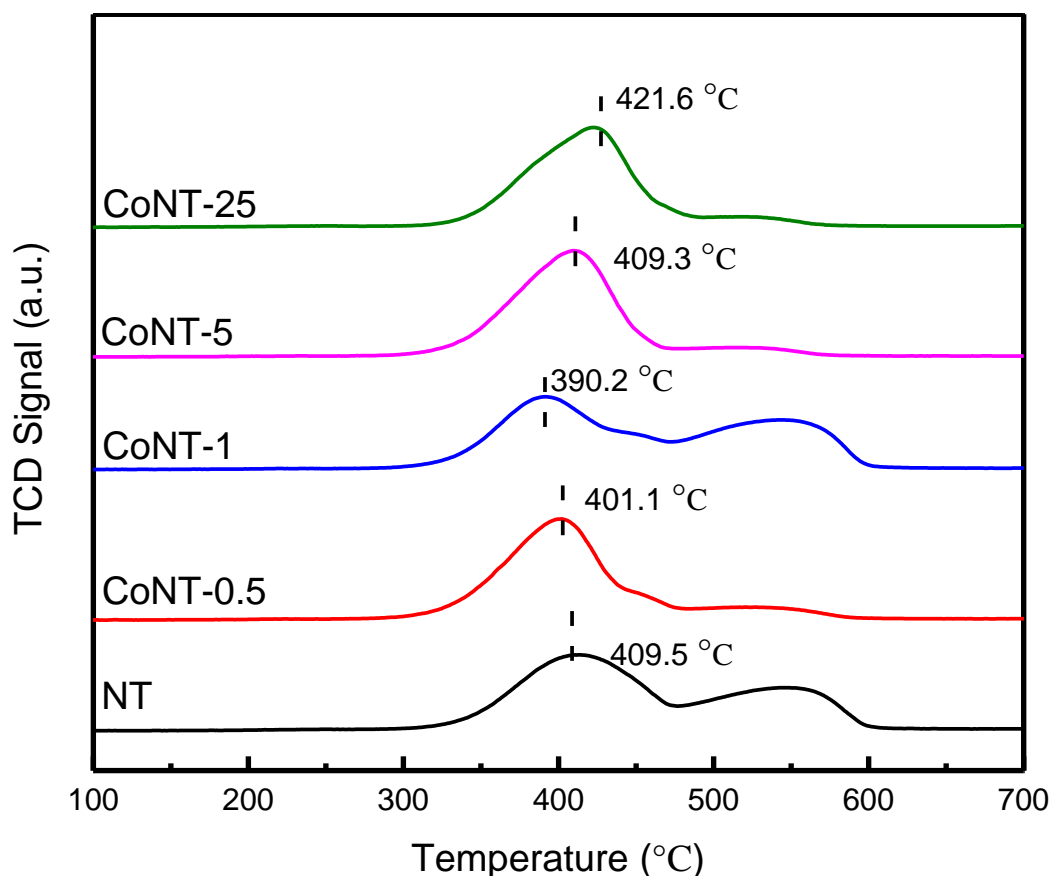


Figure 5.7 H₂-TPR result for CoNT-X catalyst.

CO₂-TPD with CO₂ as a probe molecule was used to quantify the surface basicity of the catalysts. In general, the ability of CO₂ adsorption/desorption is most highly correlated with the number of basic sites on the catalytic surface. As can be observed from Fig. 5.8, the desorption peaks for all catalysts can be divided into three kinds of basic sites, weak basic sites (<200 °C), medium basic sites (200–450 °C) and strength basic sites (>450 °C)[26]. In the previous study, the medium basic sites play the important role for CO₂ methanation, since the weak basic sites too weak to break the bonds while the strong sites provide too strong adsorption[48, 49]. The reason why CoNT-1 has the best performance can be associated with multiply medium basic sites on its surface. CoNT-1 has more metallic nickel exposed on the surface than other catalysts, which can be proved by the results of Ni⁰/Ni²⁺ of XPS, and the smaller particle size, which consistent with the grain size data in XRD. Generally speaking, small particle size has a positive effect on the methanation reaction [50, 51].

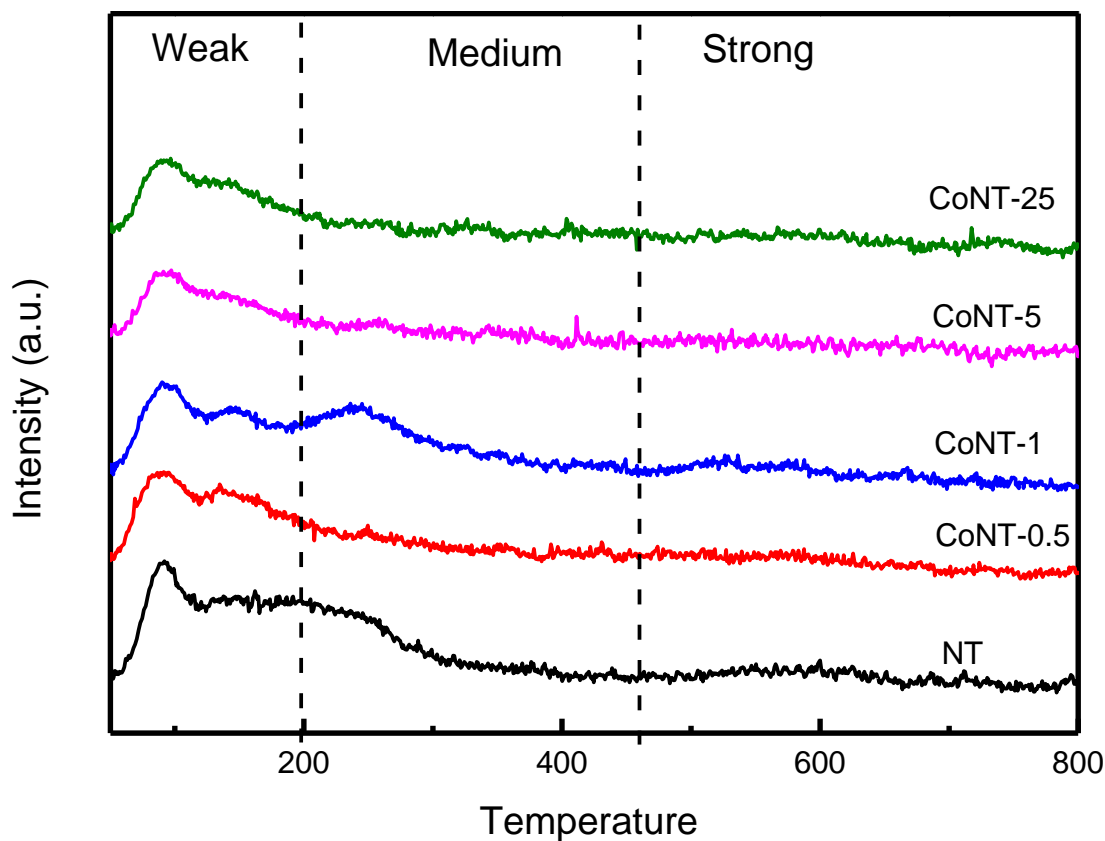
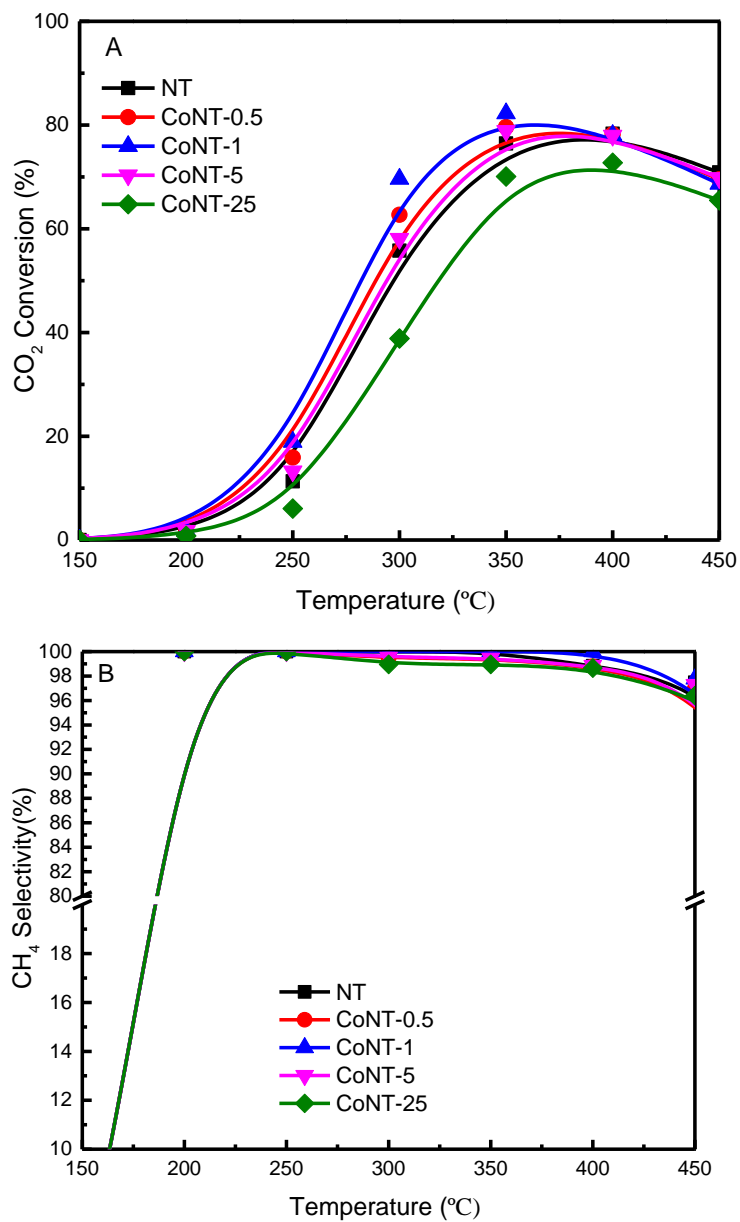


Figure 5.8 CO₂-TPD result for CoNT-X catalyst.

5.3.2 CO₂ methanation performance

Fig. 5.9 and Table 3 illustrates the catalytic performance in terms of CO₂ conversion and CH₄ yield in the range of 150 to 450 °C. The CO₂ methanation activities were evaluated in a fixed-bed plug flow reactor and detected by GC at a gas hourly space velocity (GHSV) of 12000 h⁻¹. The reaction of CO₂ conversion to methane started at 150 °C, then increase approximately exponentially up to 300 °C, where the conversion of the best catalyst was around 70 %. With further increasing temperature the increase in CO₂ conversion was slower because of the equilibrium situation of CO₂ methanation. Small amount of carbon monoxide can be detected in this temperature range. But a further increase beyond 400 °C lowered the activity of the catalyst due to the attainment of thermodynamic equilibrium. At high temperature, the CH₄ selectivity show a decreased trend because of the formation of byproduct CO. In general, the conversion of CO₂ kept on increasing at elevated temperatures with excellent selectivity CH₄ (>99%) until it was thermodynamically limited by the equilibrium over 350 °C.

Among all catalysts, CoNT-1 exhibited the best performance with the highest yield of CH₄ (86%). CO selective increased with increasing cobalt concentration.



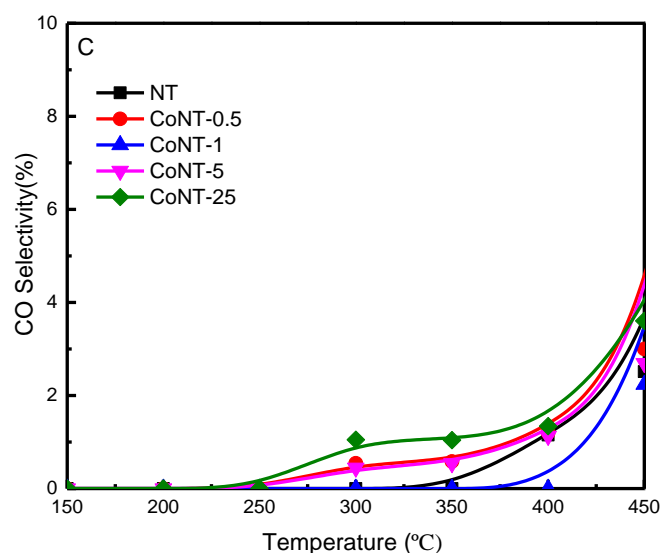


Figure 5.9 A) CO₂ conversion, B) CH₄ selectivity and C) CO selectivity of CoNT-x catalyst at 12000h⁻¹, m_{cat}= 0.1 g, H₂/CO₂= 4

Table 5.3 Selectivity of CH₄, CO₂ conversion, CH₄ yield and selectivity of CO.

T=350°C	C(CO ₂) ^a %	Y(CH ₄) ^b %	S(CH ₄) ^c %	S(CO) ^d %
NT	80.94	80.94	100.00	0.00
CoNT-0.5	83.48	83.00	99.42	0.58
CoNT-1	85.92	85.75	99.81	0.11
CoNT-5	83.18	82.73	99.46	0.54
CoNT-25	68.72	68.00	98.96	1.04

0.1g catalyst at space velocity under 12000 h⁻¹

^a Conversion of CO₂

^b Yield of CH₄

^c Selective of CH₄

^d Selective of CO

Since diffusion limitation would become more severe at higher conversions, the reaction became thermodynamically limited at the temperatures at 350 °C. Therefore, we choose to compare the activation energies around 200 °C to minimize the diffusion and thermodynamic limitations. The Arrhenius plots and activation energy values were also calculated and shown in Fig. 5.10. It can be seen that the activation energy of CoNT-1 (64.8 kJ/mol) was lower than NiTiO₃ (77.4 kJ/mol), which confirmed that

CoNT-1 showed highly enhanced performance on the CO₂ methanation compared to un-doped sample.

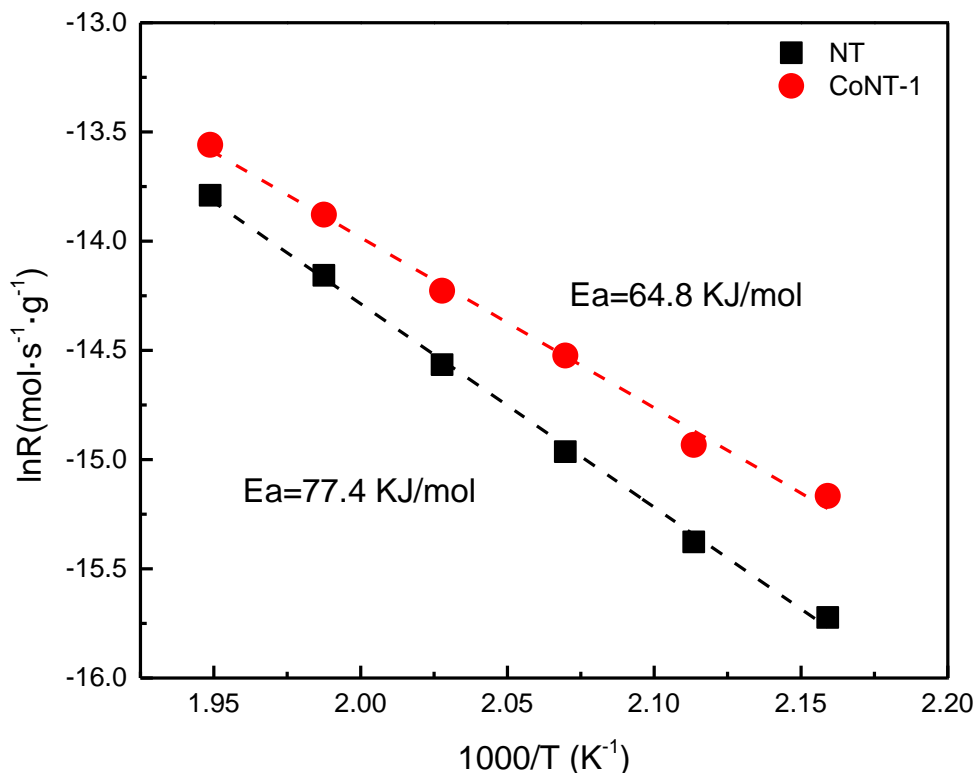


Figure 5.10 Arrhenius plot for NT and CoNT-1 catalyst at 12000 h⁻¹ around 200 °C.

The effect of space velocity on CO₂ methanation was investigated on the best catalyst (CoNT-1) at 350 °C and the results were shown in Fig. 5.11 and Table 4. The trend was obvious that the catalyst provided better performance of CO₂ conversion and main product selectivity (CH₄) at lower space velocity, while high space velocity benefited for CO production. Higher space velocity influenced the residence time and lower degree in reaction.

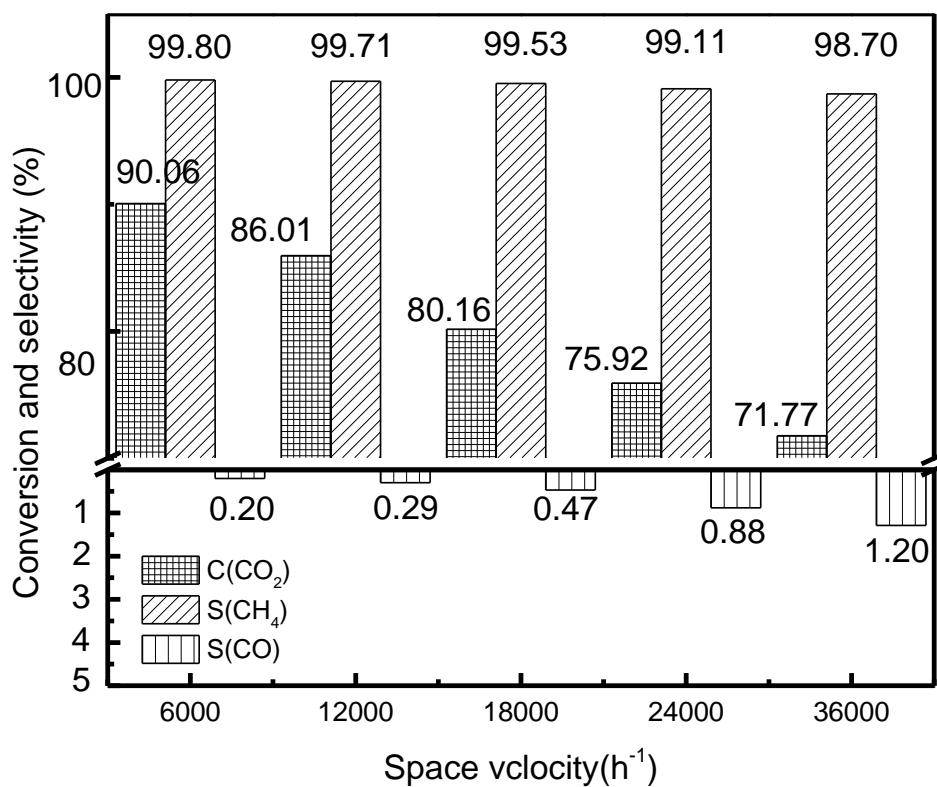


Figure 5.11 Activity test of CoNT-1 catalyst at different space velocities, 350 °C, $m_{cat} = 0.1$ g, $H_2/CO_2 = 4$

The stability test of CoNT-1 for CO₂ methanation was shown in Fig. 5.12. The best performing CoNT-1 catalyst was tested at 350 °C, H₂/CO₂ molar ratio 4 and 1200⁻¹ under atmospheric pressure for 16h. A slight decline in CO₂ conversion was observed and the CH₄ selectivity always remains at almost 100%. This catalyst exhibited high stability and low deactivation rate in the CO₂ methanation reaction.

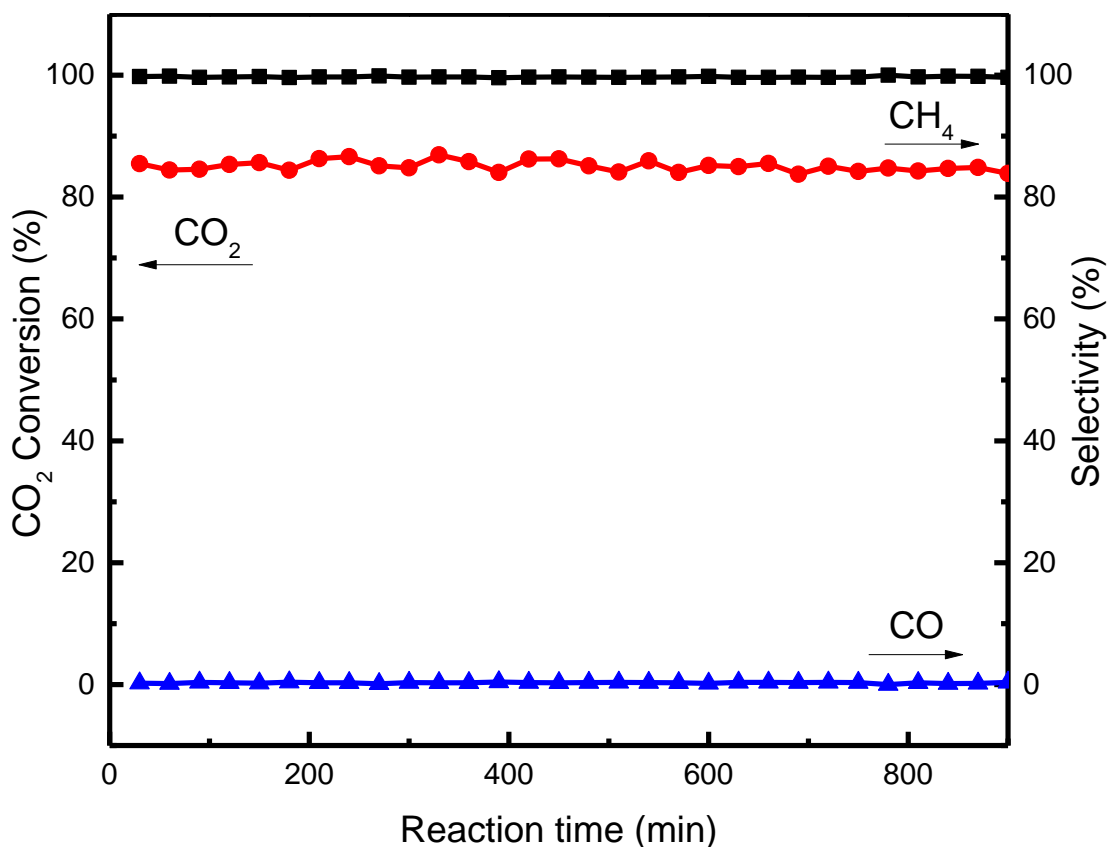


Figure 5.12 Stability test on the CoNT-1 catalyst at 350 °C, $m_{\text{cat}} = 0.1 \text{ g}$, 12000 h^{-1} , $\text{H}_2/\text{CO}_2 = 4$.

5.3.3 Catalytic mechanism analysis

The strong metal–support interaction (SMSI) appears due to an electron transfer between the support and the metals after partially reduced metal oxides modification metal surface. This effect plays a key role in catalysis by decreasing the catalytic activity (resulting in H_2 chemisorption suppression) or providing a positive effect. The activity of the catalyst may enhance because of reconstruction of the electronic structure by electron transfer between metal and a support. Jomjaree et al. reported the prominent SMSI effect between Ni and CeO_2 maintains the high stability of their Ni/ CeO_2 catalyst under low temperature operation.[11] Abdel-Mageed et al. give a research about Ru/ TiO_2 catalysts and suggested that the alternation of the electronic interactions between metal and support mainly affect CO_2 and CO methanation reaction.[16] Xu et al. studied CO_2 methanation via in-situ FTIR and DFT calculations on the Ni- ZrO_2 catalyst.[52] And they suggested that the ZrO_2 support increased the re-

ducibility and electron mobility of Ni, and induces H-spillover effect to enhanced catalyst performance.

For a comprehensive discussion, here is the summarize the main findings obtained from these characterization results.

The increase in surface metallic nickel and the change in the binding energy of cobalt reflect the electron transfer. The best performance catalyst CoNT-1 show the highest value of the ratio of $\text{Ni}^0/\text{Ni}^{2+}$ and the ratio of $\text{O}_{\text{ad}}/\text{O}_{\text{la}}$, as provided by XPS result, which implying that it has relatively largest electron cloud density on Ni and bridged $\text{O} \left(\overset{\text{(Ti-O)-Ni}}{\curvearrowright} \right)$. The results of XPS also imply the influence of oxygen vacancies on the activity, and a relatively higher concentration of oxygen vacancies is conducive to the progress of the reaction. The cobalt atom modified the electron structure between Ni and perovskite support, sufficient basic sites were provided and improved carbon dioxide capture capacity, which evidenced by XPS and CO_2 -TPD. Metal is an indispensable part of the methanation reaction, which can actively dissociate adsorbed H_2 into H atoms. XPS and H_2 -TPR demonstrate that CoNT-1 has the most abundant reduced metallic Ni particles. The effect of metal particle size is also worth considering. CoNT-1 may have the suitable particle size which also enhanced the CO_2 methanation performance, as confirmed by XRD. Scheme 1 illustrated a proposed mechanism of CO_2 methanation on the CoNT catalyst.

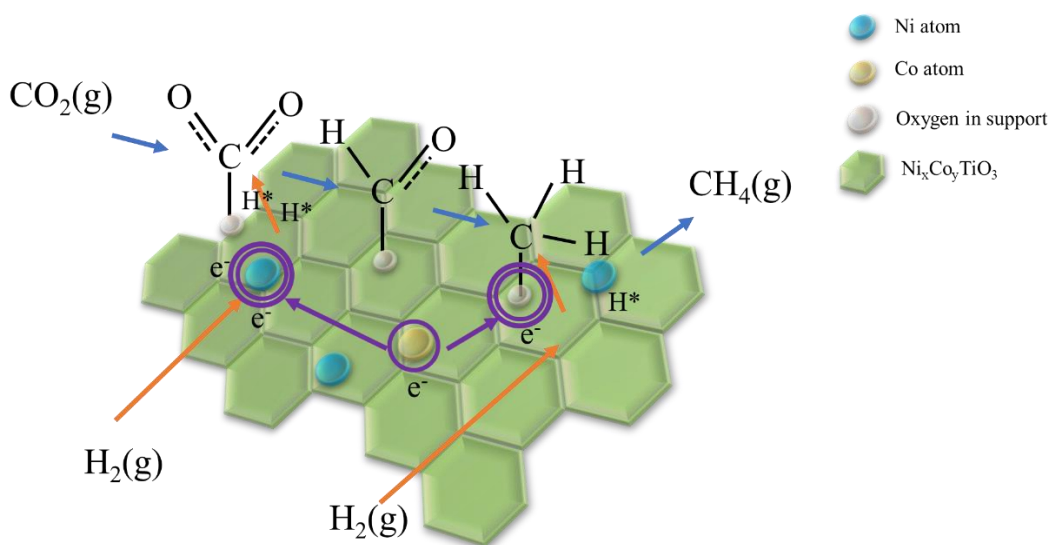


Figure 5.13 Proposed mechanism of CO_2 methanation on the CoNT catalyst.

5.4 Conclusion

In the present work, efficient and stable CoNT-x catalysts with different amounts of cobalt dopant were prepared and investigated. The best catalyst exhibited great conversion (86%) in CO₂ methanation reaction and also showed the high CH₄ selectivity at 350°C. Follow the measurements results, it was concluded that cobalt doped Co_xNi_yTiO₃ alter the reducibility of metal oxide species and strengthened metal support interaction, as well as enhancing the capacity for CO₂ and H₂ adsorption and activation. The formation of oxygen vacancies because of the Co insertion was confirmed, where those defects work as active sites for the reactants. The electronic structure changes caused by cobalt substitution further affect the number of basic sites on the surface, and these basic sites are important reactive sites. Smaller Ni and Co particle also provides more active sites for H₂ dissociation, the amount of activated hydrogen affects the subsequent hydrogenation of the reaction intermediates. This work may provide ideas for the design and development of multi-metal modified catalysts.

References

- [1] W. Zhen, F. Gao, B. Tian, P. Ding, Y. Deng, Z. Li, H. Gao, G. Lu, Enhancing activity for carbon dioxide methanation by encapsulating (111) facet Ni particle in metal-organic frameworks at low temperature, *J. Catal.*, 348 (2017) 200-211.
- [2] R.-P. Ye, L. Liao, T.R. Reina, J. Liu, D. Chevella, Y. Jin, M. Fan, J. Liu, Engineering Ni/SiO₂ catalysts for enhanced CO₂ methanation, *Fuel*, 285 (2021) 119151.
- [3] M. Aresta, A. Dibenedetto, A. Angelini, Catalysis for the Valorization of Exhaust Carbon: from CO₂ to Chemicals, Materials, and Fuels. Technological Use of CO₂, *Chem. Rev.*, 114 (2014) 1709-1742.
- [4] S.X. Bai, Q. Shao, P.T. Wang, Q.G. Dai, X.Y. Wang, X.Q. Huang, Highly Active and Selective Hydrogenation of CO₂ to Ethanol by Ordered Pd-Cu Nanoparticles (vol 139, pg 6827, 2017), *J. Am. Chem. Soc.*, 140 (2018) 524-524.
- [5] W.H. Wang, Y. Himeda, J.T. Muckerman, G.F. Manbeck, E. Fujita, CO₂ Hydrogenation to Formate and Methanol as an Alternative to Photo- and Electrochemical CO₂ Reduction, *Chem. Rev.*, 115 (2015) 12936-12973.

- [6] K. Saravanan, H. Ham, N. Tsubaki, J.W. Bae, Recent progress for direct synthesis of dimethyl ether from syngas on the heterogeneous bifunctional hybrid catalysts, *Appl. Catal. B Environ.*, 217 (2017) 494-522.
- [7] Q.X. Yang, A. Skrypnik, A. Matvienko, H. Lund, M. Holena, E.V. Kondratenko, Revealing property-performance relationships for efficient CO₂ hydrogenation to higher hydrocarbons over Fe-based catalysts: Statistical analysis of literature data and its experimental validation, *Appl. Catal. B Environ.*, 282 (2021) 11.
- [8] S. Ren, X. Fan, Z. Shang, W.R. Shoemaker, L. Ma, T. Wu, S. Li, N.B. Klinghoffer, M. Yu, X. Liang, Enhanced catalytic performance of Zr modified CuO/ZnO/Al₂O₃ catalyst for methanol and DME synthesis via CO₂ hydrogenation, *J. CO₂ Util.*, 36 (2020) 82-95.
- [9] S. Chai, Y. Men, J. Wang, S. Liu, Q. Song, W. An, G. Kolb, Boosting CO₂ methanation activity on Ru/TiO₂ catalysts by exposing (001) facets of anatase TiO₂, *J. CO₂ Util.*, 33 (2019) 242-252.
- [10] M. Saric, J.W. Dijkstra, W.G. Haije, Economic perspectives of Power-to-Gas technologies in bio-methane production, *J. CO₂ Util.*, 20 (2017) 81-90.
- [11] T. Jomjaree, P. Sintuya, A. Srifa, W. Koo-amornpattana, S. Kiatphuengporn, S. Assabumrungrat, M. Sudoh, R. Watanabe, C. Fukuhara, S. Ratchahat, Catalytic performance of Ni catalysts supported on CeO₂ with different morphologies for low-temperature CO₂ methanation, *Catal. Today*, (2020).
- [12] J.J. Gao, Q. Liu, F.N. Gu, B. Liu, Z.Y. Zhong, F.B. Su, Recent advances in methanation catalysts for the production of synthetic natural gas, *RSC Adv.*, 5 (2015) 22759-22776.
- [13] R.-P. Ye, W. Gong, Z. Sun, Q. Sheng, X. Shi, T. Wang, Y. Yao, J.J. Razink, L. Lin, Z. Zhou, H. Adidharma, J. Tang, M. Fan, Y.-G. Yao, Enhanced stability of Ni/SiO₂ catalyst for CO₂ methanation: Derived from nickel phyllosilicate with strong metal-support interactions, *Energy*, 188 (2019) 116059.
- [14] M. González-Castaño, J.C.N. de Miguel, A. Penkova, M.A. Centeno, J.A. Odriozola, H. Arellano-Garcia, Ni/YMnO₃ perovskite catalyst for CO₂ methanation, *Applied Materials Today*, 23 (2021) 101055.
- [15] Y. Zhang, Q. Liu, Nickel phyllosilicate derived Ni/SiO₂ catalysts for CO₂ methanation: Identifying effect of silanol group concentration, *J. CO₂ Util.*, 50 (2021) 101587.

- [16] A.M. Abdel-Mageed, K. Wiese, M. Parlinska-Wojtan, J. Rabeah, A. Brückner, R.J. Behm, Encapsulation of Ru nanoparticles: Modifying the reactivity toward CO and CO₂ methanation on highly active Ru/TiO₂ catalysts, *Applied Catalysis B: Environmental*, 270 (2020) 118846.
- [17] Y. Tang, Y. Wei, Z. Wang, S. Zhang, Y. Li, L. Nguyen, Y. Li, Y. Zhou, W. Shen, F.F. Tao, P. Hu, Synergy of Single-Atom Ni-1 and Ru-1 Sites on CeO₂ for Dry Reforming of CH₄, *J. Am. Chem. Soc.*, 141 (2019) 7283-7293.
- [18] Y. Yang, J. Liu, F. Liu, D. Wu, Reaction mechanism of CO₂ methanation over Rh/TiO₂ catalyst, *Fuel*, 276 (2020) 118093.
- [19] A.H. Zamani, R. Ali, W.A.W. Abu Bakar, Optimization of CO₂ methanation reaction over M*/Mn/Cu–Al₂O₃ (M*: Pd, Rh and Ru) catalysts, *J. Ind. Eng. Chem.*, 29 (2015) 238-248.
- [20] W. Zhan, Q. He, X. Liu, Y. Guo, Y. Wang, L. Wang, Y. Guo, A.Y. Borisevich, J. Zhang, G. Lu, S. Dai, A Sacrificial Coating Strategy Toward Enhancement of Metal-Support Interaction for Ultrastable Au Nanocatalysts, *J. Am. Chem. Soc.*, 138 (2016) 16130-16139.
- [21] S. Roensch, J. Schneider, S. Matthischke, M. Schlueter, M. Goetz, J. Lefebvre, P. Prabhakaran, S. Bajohr, Review on methanation - From fundamentals to current projects, *Fuel*, 166 (2016) 276-296.
- [22] A. Vita, C. Italiano, L. Pino, M. Lagana, M. Ferraro, V. Antonucci, High-temperature CO₂ methanation over structured Ni/GDC catalysts: Performance and scale-up for Power-to-Gas application, *Fuel Process. Technol.*, 202 (2020).
- [23] K. Cao, M. Gong, J. Yang, J. Cai, S. Chu, Z. Chen, B. Shan, R. Chen, Nickel catalyst with atomically-thin meshed cobalt coating for improved durability in dry reforming of methane, *J. Catal.*, 373 (2019) 351-360.
- [24] S. He, H. Wu, W. Yu, L. Mo, H. Lou, X. Zheng, Combination of CO₂ reforming and partial oxidation of methane to produce syngas over Ni/SiO₂ and Ni–Al₂O₃/SiO₂ catalysts with different precursors, *Int. J. Hydrog. Energy*, 34 (2009) 839-843.
- [25] W. Nie, X. Zou, X. Shang, X. Wang, W. Ding, X. Lu, CeO₂-assisted Ni nanocatalysts supported on mesoporous γ -Al₂O₃ for the production of synthetic natural gas, *Fuel*, 202 (2017) 135-143.
- [26] Z. Yan, Q. Liu, L. Liang, J. Ouyang, Surface hydroxyls mediated CO₂ methanation at ambient pressure over attapulgite-loaded Ni-TiO₂ composite catalysts with high activity and reuse ability, *J. CO₂ Util.*, 47 (2021) 101489.

- [27] R. Zhou, N. Rui, Z. Fan, C.-j. Liu, Effect of the structure of Ni/TiO₂ catalyst on CO₂ methanation, *Int. J. Hydrog. Energy*, 41 (2016) 22017-22025.
- [28] Z. Bian, Y.M. Chan, Y. Yu, S. Kawi, Morphology dependence of catalytic properties of Ni/CeO₂ for CO₂ methanation: A kinetic and mechanism study, *Catal. Today*, 347 (2020) 31-38.
- [29] X.Y. Jia, X.S. Zhang, N. Rui, X. Hu, C.J. Liu, Structural effect of Ni/ZrO₂ catalyst on CO₂ methanation with enhanced activity, *Appl. Catal. B Environ.*, 244 (2019) 159-169.
- [30] R. Daroughegi, F. Meshkani, M. Rezaei, Enhanced low-temperature activity of CO₂ methanation over ceria-promoted Ni-Al₂O₃ nanocatalyst, *Chem. Eng. Sci.*, 230 (2021).
- [31] L. Zhang, X.G. Wang, C.J. Chen, X.J. Zou, X.F. Shang, W.Z. Ding, X.G. Lu, Investigation of mesoporous NiAl₂O₄/MO_x (M = La, Ce, Ca, Mg)-gamma-Al₂O₃ nanocomposites for dry reforming of methane, *RSC Adv.*, 7 (2017) 33143-33154.
- [32] A.I. Inamdar, R.S. Kalubarme, J. Kim, Y. Jo, H. Woo, S. Cho, S.M. Pawar, C.-J. Park, Y.-W. Lee, J.I. Sohn, S. Cha, J. Kwak, H. Kim, H. Im, Nickel titanate lithium-ion battery anodes with high reversible capacity and high-rate long-cycle life performance, *J. Mater. Chem. A*, 4 (2016) 4691-4699.
- [33] Y. Wang, X. Chen, Q. Wang, Y. Zeng, K. Liao, S. Zhang, Q. Zhong, Novel 3D hierarchical bifunctional NiTiO₃ nanoflower for superior visible light photoreduction performance of CO₂ to CH₄ and high lithium storage performance, *Energy*, 169 (2019) 580-586.
- [34] J.Y. Do, N.-K. Park, M.W. Seo, D. Lee, H.-J. Ryu, M. Kang, Effective thermocatalytic carbon dioxide methanation on Ca-inserted NiTiO₃ perovskite, *Fuel*, 271 (2020).
- [35] M. Pudukudy, Z. Yaakob, Z.S. Akmal, Direct decomposition of methane over SBA-15 supported Ni, Co and Fe based bimetallic catalysts, *Appl. Surf. Sci.*, 330 (2015) 418-430.
- [36] K. Sakamoto, F. Hayashi, K. Sato, M. Hirano, N. Ohtsu, XPS spectral analysis for a multiple oxide comprising NiO, TiO₂, and NiTiO₃, *Appl. Surf. Sci.*, 526 (2020).
- [37] R. Shiozaki, A.G. Andersen, T. Hayakawa, S. Hamakawa, K. Suzuki, M. Shimizu, K. Takehira, Sustainable Ni/BaTiO₃ catalysts for partial oxidation of methane to synthesis gas, in: R.K. Grasselli, S.T. Oyama, A.M. Gaffney, J.E. Lyons (Eds.) *Stud. Surf. Sci. Catal.*, Elsevier 1997, pp. 701-710.

- [38] M. Zhu, P. Tian, X. Cao, J. Chen, T. Pu, B. Shi, J. Xu, J. Moon, Z. Wu, Y.-F. Han, Vacancy engineering of the nickel-based catalysts for enhanced CO₂ methanation, *Appl. Catal. B Environ.*, 282 (2021).
- [39] G.I. Siakavelas, N.D. Charisiou, S. AlKhoori, A.A. AlKhoori, V. Sebastian, S.J. Hinder, M.A. Baker, I.V. Yentekakis, K. Polychronopoulou, M.A. Goula, Highly selective and stable nickel catalysts supported on ceria promoted with Sm₂O₃, Pr₂O₃ and MgO for the CO₂ methanation reaction, *Appl. Catal. B Environ.*, 282 (2021) 19.
- [40] Z. Qin, X. Wang, L. Dong, T. Su, B. Li, Y. Zhou, Y. Jiang, X. Luo, H. Ji, CO₂ methanation on Co/TiO₂ catalyst: Effects of Y on the support, *Chem. Eng. Sci.*, 210 (2019).
- [41] Y. Xie, F. Xie, L. Wang, Y. Peng, D. Ma, L. Zhu, G. Zhou, X. Wang, G. Zhang, Efficient dry reforming of methane with carbon dioxide reaction on Ni@Y₂O₃ nanofibers anti-carbon deposition catalyst prepared by electrospinning-hydrothermal method, *Int. J. Hydrog. Energy*, 45 (2020) 31494-31506.
- [42] Y. Li, Y. Men, S. Liu, J. Wang, K. Wang, Y. Tang, W. An, X. Pan, L. Li, Remarkably efficient and stable Ni/Y₂O₃ catalysts for CO₂ methanation: Effect citric acid addition, *Appl. Catal. B Environ.*, (2021) 120206.
- [43] R.A.L. Baylon, J. Sun, L. Kovarik, M. Engelhard, H. Li, A.D. Winkelman, Y. Wang, Structural identification of Zn_xZr_yO_z catalysts for Cascade aldolization and self-deoxygenation reactions, *Appl. Catal. B Environ.*, 234 (2018) 337-346.
- [44] Y. Li, W. Yang, C. Wang, Z. Li, J. Lai, L. Wang, L. Huang, Achieving Controllable CoTiO₃-Encapsulated TiO₂ Heterostructures for Enhanced Photoelectrochemical Water Splitting, *ACS Appl. Energy Mater.*, 2 (2019) 8229-8235.
- [45] H. Vargas, J.C. Morales, X. Bokhimi, T.E. Klimova, Effect of the preparation method on the hydrogenation activity of Ni/SBA-15 catalysts: Comparison of EDTA complexation and DPU, *Catal. Today*, 305 (2018) 133-142.
- [46] S. Zhang, J. Wang, X. Wang, Effect of calcination temperature on structure and performance of Ni/TiO₂-SiO₂ catalyst for CO₂ reforming of methane, *J. Nat. Gas. Chem.*, 17 (2008) 179-183.
- [47] C. Liang, L. Zhang, Y. Zheng, S. Zhang, Q. Liu, G. Gao, D. Dong, Y. Wang, L. Xu, X. Hu, Methanation of CO₂ over nickel catalysts: Impacts of acidic/basic sites on formation of the reaction intermediates, *Fuel*, 262 (2020) 116521.
- [48] K. Zhao, W. Wang, Z. Li, Highly efficient Ni/ZrO₂ catalysts prepared via combustion method for CO₂ methanation, *J. CO₂ Util.*, 16 (2016) 236-244.

- [49] S. Li, G. Liu, S. Zhang, K. An, Z. Ma, L. Wang, Y. Liu, Cerium-modified Ni-La₂O₃/ZrO₂ for CO₂ methanation, *J. Energy Chem.*, 43 (2020) 155-164.
- [50] X.P. Guo, A. Traitangwong, M.X. Hu, C.C. Zuo, V. Meeyoo, Z.J. Peng, C.S. Li, Carbon Dioxide Methanation over Nickel-Based Catalysts Supported on Various Mesoporous Material, *Energy Fuels*, 32 (2018) 3681-3689.
- [51] Y. Yan, Y. Dai, H. He, Y. Yu, Y. Yang, A novel W-doped Ni-Mg mixed oxide catalyst for CO₂ methanation, *Appl. Catal. B Environ.*, 196 (2016) 108-116.
- [52] X. Xu, Y. Tong, J. Huang, J. Zhu, X. Fang, J. Xu, X. Wang, Insights into CO₂ methanation mechanism on cubic ZrO₂ supported Ni catalyst via a combination of experiments and DFT calculations, *Fuel*, 283 (2021) 118867.

6. Summary

6.1 Summary of this work

In the context of increasingly severe energy and environmental issues, this thesis mainly focuses on the perovskite materials for photocatalysis and the comprehensive utilization of carbon dioxide. In terms of materials, we chose nickel titanate, a typical perovskite material. The catalysts were prepared via microwave method, solvothermal method and sol-gel method. Different transition metals like cobalt, tungsten, niobium, was added in the synthesis process to adjust the particle size, oxygen vacancy concentration, surface alkalinity and electronic structure of the catalyst. We change the catalytic performance of the sample by designing a new type of semiconductor catalyst structure.

The innovation and specific work of the thesis are introduced as follows:

In the first work, nickel titanate (NTN) photocatalyst was prepared by a facile synthesis process with microwave method for photocatalytic decomposition of gas phase toluene. P25, a commercial photocatalyst, was also employed for the photocatalytic decomposition to compare their photocatalytic performance. P25 showed better catalytic performance under UV irradiation, while NTN exhibited a higher reaction rate constant under visible light irradiation. Moreover, NTN generated more CO₂ after the photocatalytic reaction than P25. From XRD patterns and Raman spectra, P25 consisted of anatase and rutile TiO₂ structures and NTN existed pure nickel titanate structure. Based on UV-Vis spectra, the bandgaps of P25 and NTN were obtained at 3.2 and 2.47 eV, respectively, implying that NTN would be a visible light-responded photocatalyst.

In second study, we investigated the changes of the structural and optical properties of NiTiO₃ materials modified by transition metal doping. cobalt or tungsten-doped NiTiO₃ materials were successfully prepared by a modified Pechini method via solvothermal treatment. Raman, FTIR, and XRD spectroscopic analyses showed that the Co²⁺ ions were selectively doped into Ni²⁺ sites in the NiTiO₃ lattice while maintaining an ilmenite structure, resulting in a solid solution of triple transition metal oxides. The size similarity between Co and Ni induced the formation of a solid solution, Co_xNi_{1-x}TiO₃, in the ilmenite structure. In contrast, W doping into the NiTiO₃ ilmenite structure resulted in an irregularity of the materials due to the characteristics of the heavy transition metal dopant. Along with increasing the W content, the crystallite size in the

ilmenite structure decreased from 90.2 to 74.5 nm and new Raman bands at 831 and 892 cm^{-1} for WO_x appeared at high W contents. However, the PL emission intensities gradually decreased with increasing doping content, implying that the recombination process was inhibited in the NiTiO_3 materials by the dopants.

In third research, Nb-doped NiTiO_3 and $\text{NbO}_x/\text{NiTiO}_3$ photocatalysts are prepared with various Nb amounts to enhance photocatalytic activity for dye photodegradation under visible light irradiation. Nb-doped NiTiO_3 exhibits higher photocatalytic activity than pure NiTiO_3 , whereas the inappropriate band structures of NbO_x and NiTiO_3 decrease photocatalytic activity. Incorporation of Nb into the NiTiO_3 lattice induces Ti^{3+} sites and oxygen vacancies. Eventually, the Nb-doped NiTiO_3 photocatalyst at the highest Nb content sample was transformed into a triple metal oxide phase with the highest surface area and oxygen vacancy. The abundant oxygen vacancy of NT-Nb-10 resulted in the lowest photoluminescence emission intensity, which resulted in the highest apparent photocatalytic reaction rate constant (k_{app}) of 14.1min^{-1} owing to the suppression of the recombination process. The formation of the triple metal oxide phase in this study may allow a potential way to modify low cost visible light-driven NiTiO_3 photocatalysts for sustainable photocatalytic application.

In fourth work, we designed and developed a stable and effective Co modified NiTiO_3 catalyst. The best catalyst exhibits high CO_2 conversion (86%) and high methane selectivity (nearly 100%), which can work continuously for 16 hours without significant deactivation at 350 °C. As evidenced by various characterization methods, like XPS, H_2 -TPD and CO_2 -TPR, Co doping are found to influence the electron distribution of the catalyst, change the size of metal particle and the interaction of metal and support, which in turn has positive impact on methanation performance, while NiTiO_3 support improve the ability to capture CO_2 because of its abundant basic oxide and oxygen vacancies after reduction. Cobalt modification proved to be an potential way to construct Ti-O-Ni interfacial structure, and increase the hydrogen activation site and carbon dioxide activation site simultaneously. This work may provide ideas for the synthesis of multi-metal modified catalysts.

6.2 Prospect

The thesis mainly pay attention to improve the photocatalytic activity and carbon dioxide methanation activity of nickel titanate materials from the perspective of sur-

face structure modification. For photocatalysis, the recombination rate of photogenerated electron and holes seriously affects the photon utilization rate. If a suitable heterojunction structure can be constructed successfully, the internal electric field can be formed inside the material. Under this electric field, photo-generated electrons and holes will migrate to different directions, which greatly promote the photon utilization rate in the catalysis process. The nickel titanate and niobium pentoxide system in this article still needs to be further optimized to improve activity. Among the modification strategies that have been selected, the atomic-level doping process has not yet been implemented. The preparation of single-atom catalysts is a major challenge in the field of catalyst preparation. It has great significance for further understanding the reaction mechanism and improving the activity.

7. Papers Published During the Study for Ph. Degree

- [1] Jiang Kaiming, Jung H, Pham T T, et al. Modification of NiTiO₃ visible light-driven photocatalysts by Nb doping and NbO_x heterojunction: Oxygen vacancy in the Nb-doped NiTiO₃ structure[J]. *Journal of Alloys and Compounds*, 2021, 861: 158636.
- [2] Jiang Kaiming, Pham T T, Kang S G, et al. Modification of the structural properties of NiTiO₃ materials by transition metal dopants: The dopant size effect[J]. *Journal of Alloys and Compounds*, 2018, 739: 393-400.
- [3] Yu Hongyan, Jiang Kaiming, Kang S G, et al. Hexagonal and Monoclinic Phases of La₂O₂CO₃ Nanoparticles and Their Phase-Related CO₂ Behavior[J]. *Nanomaterials*, 2020, 10(10): 2061.
- [4] Highly stable and selective Co_xNi_yTiO₃ for CO₂ methanation: Electron transfer and interface interaction (Under review)